

The first samples from Almahata Sitta showing contacts between ureilitic and chondritic lithologies: Implications for the structure and composition of asteroid 2008 TC₃

Cyrena Anne GOODRICH ^{1*}, Michael E. ZOLENSKY², Anna Maria FIORETTI³, Muawia H. SHADDAD⁴, Hilary DOWNES⁵, Takahiro HIROI⁶, Issaku KOHL⁷, Edward D. YOUNG⁷, Noriko T. KITA ⁸, Victoria E. HAMILTON⁹, My E. I. RIEBE ^{10,11}, Henner BUSEMANN ¹¹, Robert J. MACKE ¹², M. FRIES ¹², D. Kent ROSS¹³, and Peter JENNISKENS ¹⁴

¹Lunar and Planetary Institute, Universities Space Research Association, 3600 Bay Area Blvd, Houston, Texas 77058, USA

²Astromaterials Research and Exploration Science, NASA-Johnson Space Center, Houston, Texas 77058, USA

³CNR—Istituto di Geoscienze e Georisorse, I-35131 Padova, Italy

⁴Physics Department, University of Khartoum, Khartoum 11115, Sudan

⁵Department of Earth and Planetary Sciences, Birkbeck, University of London, Malet Street, Bloomsbury, London WC1E 7HX, UK

⁶Department of Geological Sciences, Brown University, Providence, Rhode Island 02912, USA

⁷Department of Earth and Planetary Sciences, University of California at Los Angeles, 595 Charles Young Drive East, Los Angeles, California 90095, USA

⁸Wisc-SIMS Laboratory, Department of Geoscience, University of Wisconsin-Madison, 1215 West Dayton Street, Madison, Wisconsin 53706, USA

⁹Department of Space Studies, Southwest Research Institute, 1050 Walnut St., Suite 300, Boulder, Colorado 80302, USA

¹⁰Department of Terrestrial Magnetism, Carnegie Institution for Science, 5241 Broad Branch Rd NW, Washington, District of Columbia 20015, USA

¹¹Institute for Geochemistry and Petrology, ETH Zürich, Clausiusstrasse 25, CH-8092 Zürich, Switzerland

¹²Specola Vaticana, V-00120, Vatican City State, Italy

¹³Jacobs-JETS, University of Texas at El Paso at NASA-JSC, Houston, Texas 77058, USA

¹⁴SETI Institute, 189 Bernardo Ave, Mountain View, California 94043, USA

*Corresponding author. E-mail: goodrich@lpi.usra.edu

(Received 27 February 2019; revision accepted 17 August 2019)

Abstract—Almahata Sitta (AhS), an anomalous polymict ureilite, is the first meteorite observed to originate from a spectrally classified asteroid (2008 TC₃). However, correlating properties of the meteorite with those of the asteroid is not straightforward because the AhS stones are diverse types. Of those studied prior to this work, 70–80% are ureilites (achondrites) and 20–30% are various types of chondrites. Asteroid 2008 TC₃ was a heterogeneous breccia that disintegrated in the atmosphere, with its clasts landing on Earth as individual stones and most of its mass lost. We describe AhS 91A and AhS 671, which are the first AhS stones to show contacts between ureilitic and chondritic materials and provide direct information about the structure and composition of asteroid 2008 TC₃. AhS 91A and AhS 671 are friable breccias, consisting of a C1 lithology that encloses rounded to angular clasts (<10 μm to 3 mm) of olivine, pyroxenes, plagioclase, graphite, and metal-sulfide, as well as chondrules (~130–600 μm) and chondrule fragments. The C1 material consists of fine-grained phyllosilicates (serpentine and saponite) and amorphous material, magnetite, breunnerite, dolomite, fayalitic olivine (Fo 28–42), an unidentified Ca-rich silicate phase, Fe,Ni sulfides, and minor Ca-phosphate and ilmenite. It has similarities to C11 but shows evidence of heterogeneous thermal metamorphism. Its bulk oxygen isotope composition (δ¹⁸O = 13.53‰, δ¹⁷O = 8.93‰) is unlike that of any known chondrite, but similar to compositions of several CC-like clasts in typical polymict ureilites. Its Cr isotope composition is unlike that of any known meteorite. The enclosed clasts and chondrules do

not belong to the C1 lithology. The olivine (Fo 75-88), pyroxenes (pigeonite of Wo ~10 and orthopyroxene of Wo ~4.6), plagioclase, graphite, and some metal-sulfide are ureilitic, based on mineral compositions, textures, and oxygen isotope compositions, and represent at least six distinct ureilitic lithologies. The chondrules are probably derived from type 3 OC and/or CC, based on mineral and oxygen isotope compositions. Some of the metal-sulfide clasts are derived from EC. AhS 91A and AhS 671 are plausible representatives of the bulk of the asteroid that was lost. Reflectance spectra of AhS 91A are dark (reflectance ~0.04–0.05) and relatively featureless in VNIR, and have an ~2.7 μm absorption band due to OH^- in phyllosilicates. Spectral modeling, using mixtures of laboratory VNIR reflectance spectra of AhS stones to fit the F-type spectrum of the asteroid, suggests that 2008 TC₃ consisted mainly of ureilitic and AhS 91A-like materials, with as much as 40–70% of the latter, and <10% of OC, EC, and other meteorite types. The bulk density of AhS 91A ($2.35 \pm 0.05 \text{ g cm}^{-3}$) is lower than bulk densities of other AhS stones, and closer to estimates for the asteroid (~1.7–2.2 g cm^{-3}). Its porosity (36%) is near the low end of estimates for the asteroid (33–50%), suggesting significant macroporosity. The textures of AhS 91A and AhS 671 (finely comminuted clasts of disparate materials intimately mixed) support formation of 2008 TC₃ in a regolith environment. AhS 91A and AhS 671 could represent a volume of regolith formed when a CC-like body impacted into already well-gardened ureilitic + impactor-derived debris. AhS 91A bulk samples do not show a solar wind component, so they represent subsurface layers. AhS 91A has a lower cosmic ray exposure (CRE) age (~5–9 Ma) than previously studied AhS stones (11–22 Ma). The spread in CRE ages argues for irradiation in a regolith environment. AhS 91A and AhS 671 show that ureilitic asteroids could have detectable ~2.7 μm absorption bands.

INTRODUCTION

Asteroid 2008 TC₃ was the first near-Earth object (NEO) to be detected before it hit the Earth (Chesley et al. 2008; Kowalski 2008; Yeomans 2008). It was discovered on October 6, 2008, and then tracked and studied for ~20 h before it impacted in northern Sudan (Jenniskens et al. 2009; Scheirich et al. 2010; Kozubal et al. 2011). Organized search campaigns in the predicted fall area resulted in recovery of more than 700 stones, ~0.2–400 g in mass, which were collectively named the Almahata Sitta (AhS) meteorite (Shaddad et al. 2010). AhS is the first meteorite observed to originate from a spectrally classified asteroid, and provides an unprecedented opportunity to correlate spectral, compositional, and physical properties of a meteorite with those of the asteroid from which it was derived.

Almahata Sitta is also remarkable because, unlike any previous known meteorite fall, its stones are not all the same meteorite type. The main collection of AhS is curated at the University of Khartoum (UoK), documented with find coordinates for each stone in the strewn field (Fig. 1). Eighty-five of these stones have been studied so far, as well as ~100 AhS stones from unknown find locations that were distributed by private meteorite dealers. Based on these studies, approximately 70–80% of the stones are ureilites (carbon-rich ultramafic achondrites that represent the residual mantle of a differentiated

asteroid), whereas 20–30% are various types of chondrites (Zolensky et al. 2010; Horstmann and Bischoff 2014; Bischoff et al. 2015a, 2016; Fioretti et al. 2017; Goodrich et al. 2018). The ureilites span the entire range of petrologic types seen among main group ureilites, and the chondrites include all major classes (enstatite, ordinary, carbonaceous, and Rumuruti-type chondrites) and numerous groups and subgroups (Horstmann and Bischoff 2014; Goodrich et al. 2015a). AhS is classified as an anomalous polymict ureilite (Jenniskens et al. 2009). This classification implies that it is analogous (though not necessarily identical) to typical polymict ureilites, which are breccias dominated by ureilitic material but also containing chondritic and other xenolithic clasts (Prinz et al. 1986, 1987; Goodrich et al. 2004; Downes et al. 2008). However, unlike typical polymict ureilites, AhS has been disaggregated. It can be inferred that 2008 TC₃ was a heterogeneous asteroidal breccia in which the clasts were so loosely bound that they separated in the atmosphere and landed on Earth as individual stones.

Pre-impact observations of 2008 TC₃ support this inference. The average diameter of the asteroid was ~4 m, based on the light curve and F-type reflectance spectrum (Jenniskens et al. 2009; Scheirich et al. 2010). Its bulk density was ~1.7 g cm^{-3} , based on its size and abundances of cosmogenic nuclides in some of the stones (Welten et al. 2010). This value is significantly lower than densities of the studied stones, particularly the typical ureilites

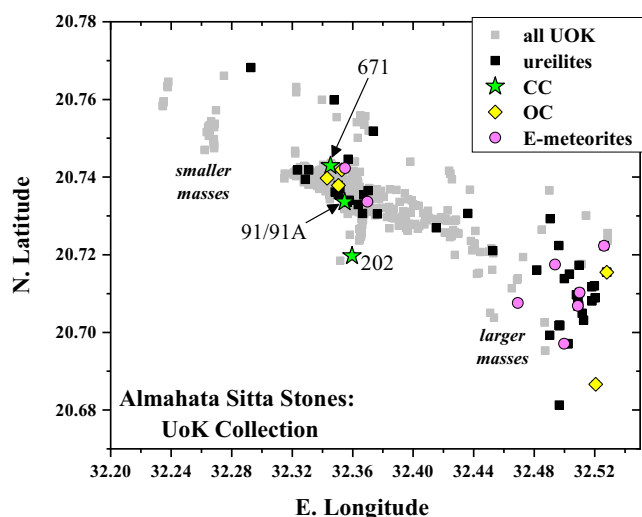


Fig. 1. Find coordinates for Almahata Sitta (AhS) stones in the University of Khartoum (UoK) collection (Shaddad et al. 2010). Classification of 85 stones from Zolensky et al. (2010) and Goodrich et al. (2018). The asteroid path was from NW to SE. The three carbonaceous chondrite (CC) stones are noted by sample number. AhS 91/91A and AhS 671 are the subject of this paper. AhS #202 was briefly described in Fioretti et al. (2017) and Goodrich et al. (2018). (Color figure can be viewed at wileyonlinelibrary.com.)

($\sim 3.3 \text{ g cm}^{-3}$), which implies $\sim 25\text{--}50\%$ porosity in the asteroid (Jenniskens et al. 2009; Welten et al. 2010). This suggests that the asteroid was loosely consolidated, which explains why it shattered at such a high altitude (Borovička and Charvát 2009; Jenniskens et al. 2009; Shaddad et al. 2010; Popova et al. 2011). These data also imply that most of the mass of 2008 TC₃ was lost in the atmosphere, probably as dust. The total mass of fallen material was estimated to be $\sim 40 \text{ kg}$ (Shaddad et al. 2010), representing $\leq 0.1\%$ of the estimated mass of the asteroid. Thus, the asteroid must have consisted of $>99\%$ loosely consolidated, porous material, with only the small fraction of more coherent clasts surviving as meteorite fragments (Jenniskens et al. 2009; Goodrich et al. 2015a). Nevertheless, the reflectance spectrum of the asteroid provides information on the composition and grain size of the lost material.

The reflectance spectrum of 2008 TC₃ was measured in the $0.5\text{--}1 \mu\text{m}$ range (Jenniskens et al. 2009, 2010), and most closely matches F-type asteroids in the Tholen taxonomy (Tholen and Barucci 1989). The average F-type albedo of 0.046 (Mainzer et al. 2011) is consistent with independent estimates of the asteroid's size (Jenniskens et al. 2009). F-type asteroids belong to the C complex of dark asteroids commonly identified with carbonaceous chondrites (Tholen and Barucci 1989; DeMeo et al. 2009, 2015). If AhS had not been recovered, 2008 TC₃ would have been assumed to be a carbonaceous chondrite. The recovery of AhS provided

irrefutable evidence that not all dark asteroids are primitive, making studies of the AhS stones important for distinguishing differentiated dark asteroids from primitive dark asteroids.

However, determining the structure and composition of asteroid 2008 TC₃ has been hindered so far because none of the studied AhS stones showed contacts between ureilitic and chondritic lithologies. Here, we describe the first AhS stones that do. AhS 91/91A and AhS 671 are breccias consisting of C1 carbonaceous chondrite, ureilite, ordinary chondrite, and enstatite chondrite components. We report mineralogy and petrology, oxygen isotope compositions, density and porosity, reflectance spectra from visible through thermal infrared (VNIR to TIR) wavelengths, and noble gas abundances for these two AhS stones. We also measured chromium isotope compositions, which are reported elsewhere (Sanborn et al. 2017; Yin et al. 2018). We discuss implications for the structure, composition, and formation of asteroid 2008 TC₃, and for remote sensing of ureilitic asteroids.

SAMPLES AND ANALYTICAL METHODS

UoK stones 91 and 91A (hereafter referred to collectively as 91A) were recovered together near the central part of the AhS strewn field (Fig. 1). They were suspected to be paired (Shaddad et al. 2010) and this is confirmed by the results of our studies. The two stones originally had a combined mass of 8.57 g, but they are extremely friable and have been progressively crumbling into smaller fragments (e.g., Fig. 2). AhS 671 (original mass 11.85 g) was recovered $\sim 1400 \text{ m}$ from AhS 91A (Fig. 1) and is also very friable. We were allocated $\sim 1.5 \text{ g}$ of each, entirely as small fragments (most $< 100 \text{ mg}$ each). We used a variety of analytical techniques to study these fragments (Supplement 1 in supporting information) including: X-ray computed tomography (XRCT or CT scans); field emission scanning electron microscopy (FE-SEM); field emission electron microprobe analyses (FE-EMPA); focused ion beam (FIB) milling and transmission electron microscopy (TEM); Raman spectroscopy; visible-to-near-infrared (VNIR) and Fourier transform infrared (FT-IR) reflectance spectroscopy; microscopic FTIR ($\mu\text{-FTIR}$) reflectance spectroscopy; noble gas analysis; bulk and in situ (SIMS) oxygen isotope analyses; chromium isotope analysis (reported elsewhere); and determination of bulk density, grain density, and porosity. All analytical methods are described in Supplement 2 in supporting information.

RESULTS

Petrography and Mineral Compositions

We studied polished sections of 20 fragments of AhS 91A and 22 fragments of AhS 671, with exposed

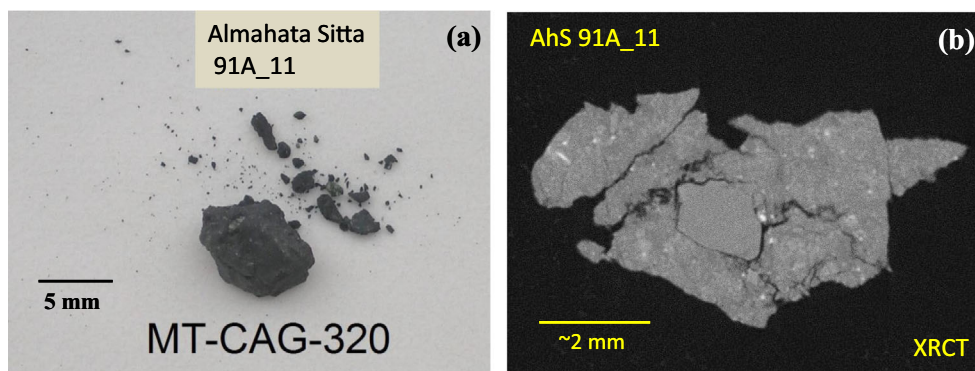


Fig. 2. a) Fragment AhS 91A_11, showing the highly friable nature of this stone. Crumbs in this image were not chipped off the sample, but fell off by themselves. b) Image from the interior of a CT scan of AhS 91A_11, showing large mineral clast (possibly ureilitic) embedded in fine-grained CC-like material. (Color figure can be viewed at wileyonlinelibrary.com.)

areas ranging from ~ 0.05 to 10 mm^2 . These two AhS breccias are very similar and consist of a hydrous carbonaceous chondrite-like lithology (C1) enclosing clasts of olivine, pyroxene, plagioclase, and graphite (ranging from $<10 \mu\text{m}$ to $\sim 3 \text{ mm}$ in size), as well as chondrules ($\sim 130\text{--}600 \mu\text{m}$ in diameter) and metal-sulfide grains (up to $\sim 1.3 \text{ mm}$ in size). Most of the fragments studied do not show this entire assemblage. Individual fragments consist of either (1) C1 matrix material; (2) olivine, pyroxene, plagioclase, or metal grains; (3) C1 material containing or in contact with clasts of olivine, pyroxene, plagioclase, and/or metal; or (4) C1 material containing chondrules, as well as clasts of olivine, pyroxene, plagioclase, and metal.

C1 Material

C1 material is the most abundant component (Figs. 3–11). It consists mostly of fine-grained phyllosilicates, with varying abundances of a Ca-rich silicate phase, carbonates, magnetite, fayalitic olivine, and Fe,Ni sulfides, plus minor Ca-phosphate and ilmenite. Its texture shows a variety of rounded clasts in a fine-grained matrix, with the clasts differing in relative proportions of phases, as well as how distinct they are from the matrix. One common type of clast (e.g., areas 1 and 3 in Figs. 3a and 3b) is Ca-rich. It consists of phyllosilicates plus a high abundance of a patchy to fibrous Ca-rich silicate phase, as well as clusters of magnetite grains (Fig. 4). Another type of clast (e.g., area 4 in Figs. 3a and 3b) consists almost entirely of serpentine intergrown with one or more poorly crystalline phyllosilicates, plus a few larger pyrrhotite grains (Fig. 5). The matrix of the C1 lithology is a fine-grained mixture of all observed phases in varying proportions (e.g., Figs. 3c and 3d).

Broad beam electron microprobe (EMP) analyses suggest that the most abundant phyllosilicates in both clasts and matrix are a mixture of serpentine with

varying Mg# (=molar $\text{Mg}/[\text{Mg} + \text{Fe}]$) and saponite (Fig. 6; Table 1). FIB/TEM observations of area 1, a Ca-rich clast, revealed that most silicates are poorly crystalline (Figs. 7 and 8). Local regions of flaky phyllosilicates (Figs. 7, 8a, and 8b) grade into moderately well crystalline spongy phyllosilicates, and then into poorly crystalline spongy material (Figs. 7, 8c, and 8d). These morphologies are very similar to those commonly observed in CI chondrites (Barber 1981, 1985; Zolensky et al. 1993). Flaky phyllosilicates frequently surround Fe,Ni sulfide grains (Fig. 7). Phyllosilicate packets are generally $<100 \text{ nm}$ across and are not well crystalline. Interlayer lattice spacings vary from 0.95 to 1.3 nm. This information and EDX spectra indicate a mixture of at least two phyllosilicate phases and Fe,Ni sulfides. The interlayer lattice fringes and approximate composition of one of these phyllosilicates are consistent with a smectite, perhaps saponite, with lattice spacings from 1.1 to 1.3 nm. Approximately 1 nm d-spacings are common in smectite (saponite) in Orgueil (Klimentidis and MacKinnon 1986). Naturally dehydrated meteoritic smectites exhibit a range of interlayer spacings from 1.1 to 1.4 nm (e.g., Nakamura 2005; Tonui et al. 2014), as observed in AhS 91A.

The Ca-rich silicate phase or assemblage ($\sim 13\text{--}15 \text{ wt}\%$ CaO; Table 1) in area 1 and similar clasts has not yet been identified. Based on EMP totals of $\sim 94\text{--}97\%$, this phase contains less OH than serpentine or a smectite (such as saponite), for which totals typically range 87–89%. FIB/TEM analyses (Fig. 4d) showed this “phase” to consist of Ca-rich, poorly crystalline material with occasional flakes of a layered phase with a basal spacing of 0.95–0.96 nm, which we verified by recalibrating our scale bar for TEM images. This layer lattice value would be correct for completely dehydrated smectites. However, the Ca content of this “phase” is far too high to be only a smectite. Therefore, we hypothesize that this Ca-rich material is an assemblage

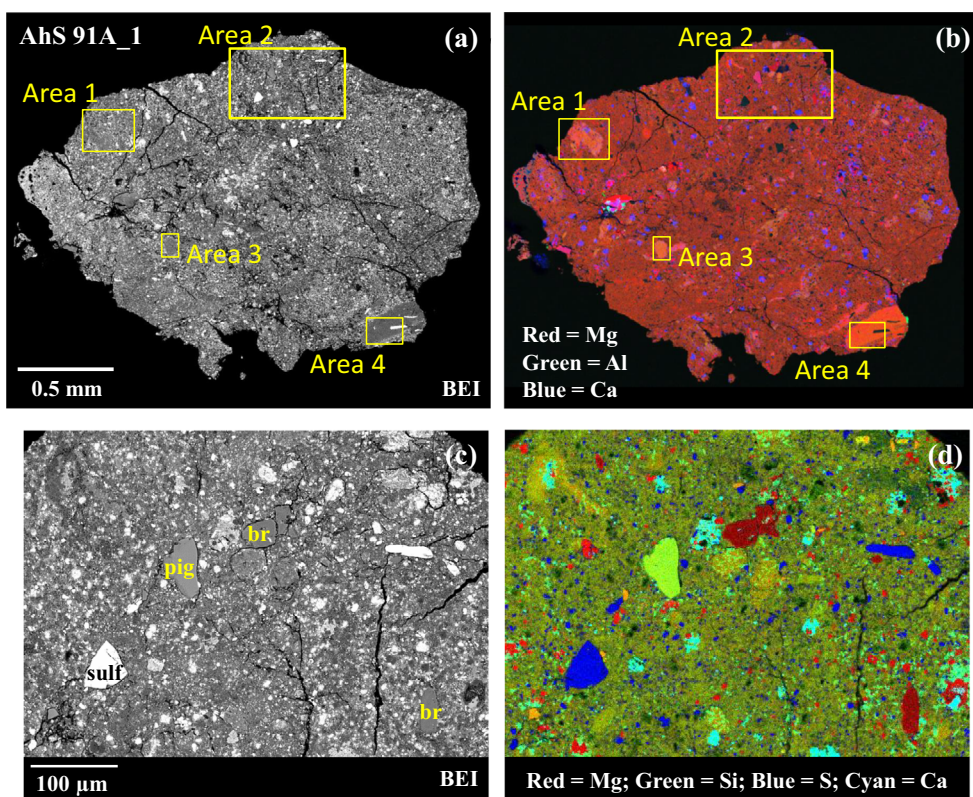


Fig. 3. Backscattered electron images (BEI) and X-ray elemental maps of fragment AhS 91A_1. This fragment consists mostly of a C1 lithology, but contains a few small clasts of ureilitic minerals. a) BEI of whole fragment. b) Mg (red)—Al (green)—Ca (blue) map corresponding to (a). c) BEI of area 2 marked in (a, b). sulf = (sulfide); pig = pigeonite; br = breunnerite. d) Mg (red)—Si (green)—S (blue)—Ca (cyan) map corresponding to (c). Pigeonite grain in (c, d) is consistent with ureilitic pigeonite compositions. (Color figure can be viewed at wileyonlinelibrary.com.)

of two phases. Elsewhere in AhS 91A, we observe phyllosilicates in association with Ca-bearing carbonates. After phyllosilicates begin to dehydrate, Ca carbonates calcine to CaO plus CO₂ (Rodríguez-Navarro et al. 2009). In permeable rocks (e.g., at or near an asteroid's surface), the CO₂ would escape, and at this low CO₂ pressure, calcination occurs at temperatures as low as 450 °C (Grasa et al. 2014), a temperature consistent with dehydration of smectites (Nakamura 2005; Tonui et al. 2014). Thus, the Ca-rich “phase” may be a mixture of poorly crystalline CaO and dehydrated smectite. This possibility will be further investigated with other techniques.

FIB/TEM observations of area 4 (Fig. 5) showed that the dominant fibrous phase has a basal lattice spacing of 0.770–0.772 nm consistent with Mg-rich serpentines (Mg# ~0.9 based on EMPA; Fig. 6). The serpentine is surrounded by poorly crystalline spongy phyllosilicates. Chrysotile serpentine is occasionally observed here with characteristic cylindrical morphology, although these sometimes do not show well-defined lattice fringes (Fig. 5d), a characteristic of heating to temperatures <300 °C (Nakamura 2005; Tonui et al. 2014).

Breunnerite is the most abundant carbonate in the C1 lithology (Fig. 9a), occurring as rounded grains, ~70–400 μm in size, with average composition Mg_{0.64}Fe_{0.26}Mn_{0.09}Ca_{0.01}CO₃ in AhS 91A and Mg_{0.67}Fe_{0.24}Mn_{0.07}Ca_{0.02}CO₃ in AhS 671 (Table 2). Dolomite grains of similar size were observed in AhS 91A (Fig. 9b), with average composition Mg_{0.43}Fe_{0.06}Mn_{0.03}Ca_{0.48}CO₃ (Table 2). Both types of carbonate have corroded outer rims with magnesite-enriched breunnerite compositions (e.g., Mg_{0.88}Fe_{0.11}Mn_{0.01}Ca_{0.00}CO₃). Breunnerite similar in composition to the rims also occurs as 10–20 μm-sized irregular patches in the matrix (Figs. 3c and 3d; Table 2).

Magnetite occurs pervasively in the matrix as clusters of anhedral to subhedral grains with irregular rims of porous, fayalitic olivine (Figs. 10a, 10c, and 10d), as clusters of radially oriented grains (Figs. 4a–c), and also as subhedral grains embedded in pyrrhotite (Fig. 10b). Abundances of minor elements in the magnetite are extremely low (Figs. 10e and 10f; Table 3), similar to magnetite in CI and CR chondrites (Böstrom and Fredriksson 1966; Folinsbee et al. 1967; Löhn and El Goresy 1992; Harju et al. 2014), as well as CC-like clasts in typical polymict ureilites. Fine-grained

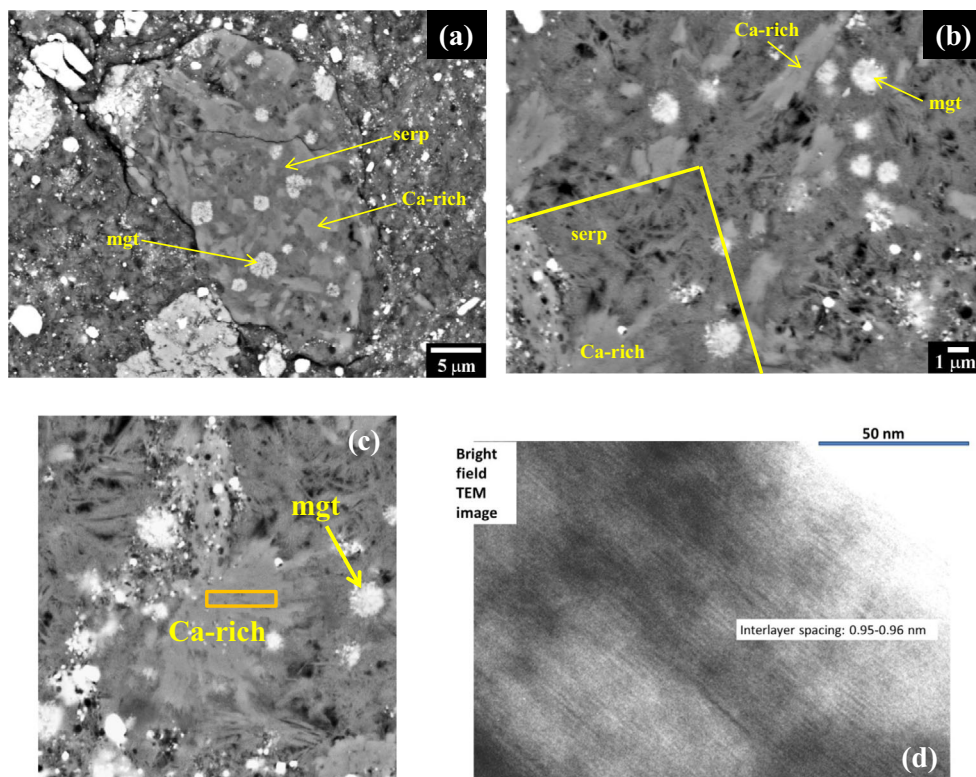


Fig. 4. a) BEI of a common type of clast in the C1 lithology of AhS 91A. Such clasts consist of laths or patches of an unidentified Ca-rich silicate phase in a matrix of serpentine (serp) and other (?) phyllosilicates, with clusters of magnetite (mgt) grains. b) BEI showing interior of clast in area 1 of AhS 91A_1 (Figs. 3a and 3b). c) Detail from lower left corner of (b). Rectangular box indicates position of FIB section made from this area and studied by TEM. d) Bright-field TEM image of a detail from the FIB section from (c) showing a well-crystallized phyllosilicate with a 0.95–0.96 nm interlayer spacing, possibly dehydrated smectite with a composition between montmorillonite and saponite. (Color figure can be viewed at wileyonlinelibrary.com.)

sulfides are dispersed abundantly throughout the matrix. Some matrix areas have concentrations of fayalitic olivine (Fo 28–42), which occurs as porous tabular crystals with numerous small inclusions of other phases (Fig. 11). Such areas appear to be more abundant in AhS 671 than AhS 91A.

Clasts of Olivine, Pyroxene, Plagioclase, Graphite, and Metal

Clasts of olivine, pigeonite, orthopyroxene, plagioclase, and graphite (in order of decreasing abundance) are embedded in the C1 matrix (Figs. 12 and 13). They are rounded to angular and up to ~3 mm in size. They are completely enclosed within the C1 material and show no evidence of reaction with their surroundings (Figs. 12 and 13). In a few occurrences, they are concentrated along cracks or in brecciated zones. Some of the olivine clasts appear to be polymineralic and some have small inclusions of graphite. Otherwise, no compound clasts were observed.

The olivine clasts are homogeneous except for reduced zones (Mg-enriched olivine containing numerous tiny grains of metal) along grain boundaries

and around inclusions of graphite (Figs. 12a and 12c). Core compositions range from Fo 75 to 87.5 among clasts (Table 4). At least six distinct olivine core compositions were observed. Reduced zones have higher Fo than cores, up to ~99. Several olivine clasts of Fo ~78–79 contain micron-sized symplectic lamellae of chromite + pyroxene (Fig. 12e). Figure 14 shows plots of molar Fe/Mg versus molar Fe/Mn and wt% Cr₂O₃ versus CaO for all olivine clasts (including reduced zones), compared with olivine in other types of meteorites. The clasts plot along the Fe/Mg versus Fe/Mn trend defined by the olivine+low-Ca pyroxene main group ureilites (Fig. 14a), and encompass most of the ureilite range. They have high CaO (~0.25–0.50 wt%) and Cr₂O₃ (~0.45–1.0 wt%) contents, which are also consistent with those in ureilite olivine (Fig. 14b). These features distinguish the olivine clasts in AhS 91A and AhS 671 from olivines in C1 and C2 carbonaceous chondrites, type 4–6 ordinary and enstatite chondrites (Steele 1990; Leshin et al. 1997; Brearley and Jones 1998; Frank et al. 2014), and all major groups of olivine-rich achondrites other than ureilites.

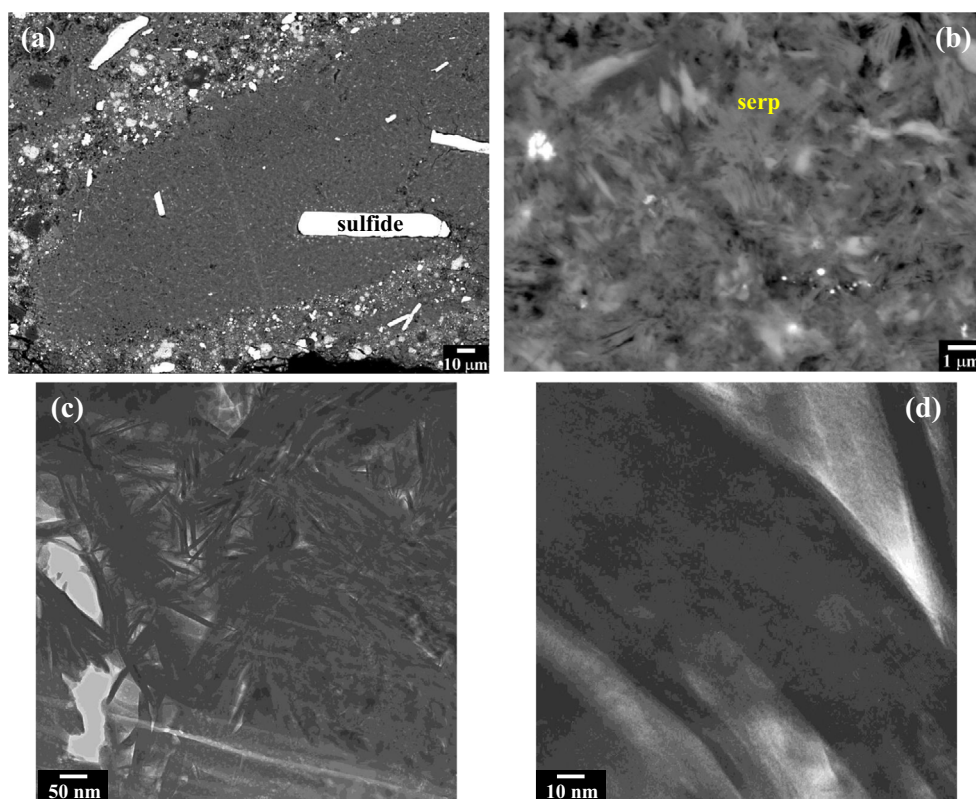


Fig. 5. a) BEI of phyllosilicate-rich clast in area 4 of AhS 91A_1 (Figs. 3a and 3b). b) Detail of clast in (a), showing fine-grained mixture of serpentine (serp) plus other phyllosilicates. c) Low magnification bright-field TEM image of the flaky serpentine with flakes exhibiting 0.7 nm basal lattice fringes characteristic of serpentine-type phases. d) Detail from (c) showing a few serpentine flakes, but with none showing basal lattice fringes, indicating heating and dehydration. (Color figure can be viewed at wileyonlinelibrary.com.)

The pyroxene clasts in AhS 91A and AhS 671 (Table 4) include pigeonite of $Wo \sim 7\text{--}10$ (Mg# 78–88), orthopyroxene of $\sim Wo 4.5$ (Mg# 88–89), and one clast of orthopyroxene of $Wo 0.8$ (Mg# 99.5) (note that we refer to pyroxenes with $Wo < 5$ as orthopyroxene). Each clast is homogeneous, except that some pigeonites have irregularly shaped, porous, Mg-rich patches containing blebs of metal (Fig. 13c). At least five distinct pigeonite compositions were observed (Table 4). Major and minor (Al_2O_3 and Cr_2O_3) element compositions of the pyroxene clasts are compared with compositions of low-Ca pyroxenes in other types of meteorites in Fig. 15. The pigeonite and $Wo \sim 4.5$ orthopyroxene clasts are consistent with compositions of low-Ca pyroxenes in main group and typical polymict ureilites, and are distinguished from those of low-Ca pyroxenes in most other groups of chondrites and achondrites. The one orthopyroxene clast of $Wo \sim 0.8$ has major and minor element compositions consistent with orthopyroxenes in several types of chondrites (Fig. 15).

Three plagioclase clasts were observed (Figs. 13e and 13f). Two are Na-rich (An $\sim 3\text{--}5$, Or 3–4). The third is more calcic, with An ~ 35 (Table 4, columns 16–18). The

analyses are stoichiometric (Table 4), suggesting that they are or once were crystalline. Graphite (identified by Raman spectroscopy, Supplement 3 in supporting information) occurs as inclusions in olivine clasts, and as isolated masses up to $\sim 300 \mu m$ in size in the C1 matrix (Fig. 13d). Several of the isolated graphite masses were found to contain minor diamond (Supplement 3).

Three types of metal grains (or assemblages) were observed. The first type consists of kamacite containing significant P, Cr, and Si (Table 5), and is sometimes associated with Cr-bearing troilite. Metal grains of this type occur as inclusions in graphite masses (e.g., Fig. 13d). The second type consists of kamacite + taenite \pm troilite (e.g., Fig. 16a), with the kamacite having very low Si, P, and Cr contents (Table 5). The third type consists of Si-rich, Cr-poor kamacite (Table 5) with abundant inclusions of enstatite and niningerite (e.g., Figs. 16c,d). One particularly large clast of this type is a 1.2 mm long lath in AhS 91A_09 (Fig. 16b). Compositions of the kamacite in the clasts are compared with compositions of kamacite in ureilites, ordinary chondrites, enstatite chondrites, and iron meteorites in Fig. 17.

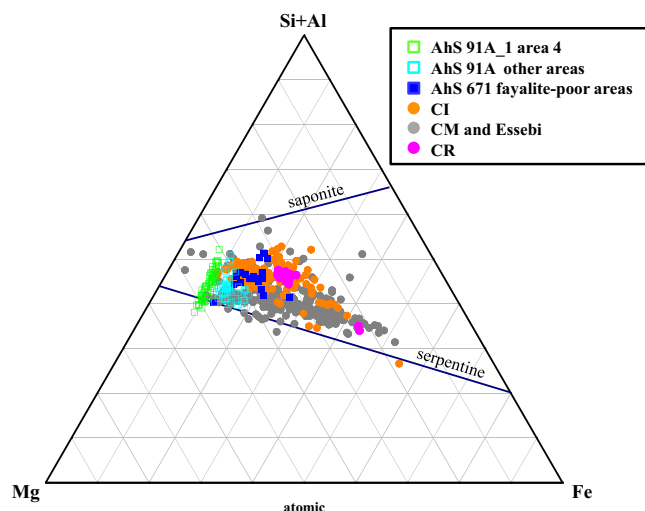


Fig. 6. (Si + Al)-Mg-Fe atomic percent ternary diagram plotting compositions of phyllosilicates in AhS 91A and AhS 671 compared with those in selected carbonaceous chondrites (data collected in this work for CM, CI, and CR chondrites). Lines cutting through the ternary represent the observed stoichiometric compositions of serpentine and saponite (from Deer et al. 1962; Fleet 2003). CMs in the plot are Boriskino (96 points), Crescent (18), Santa Cruz (21), Cochabamba (51), and MET01070 (75). CIs are Alais (55 points) and Orgueil (101). The CR is Renazzo (18 points). Essebi (39) is a C2 related to CMs. Data for AhS 91A (area 4—76 points, other areas—45 points) and AhS 671 (19 points). Data for all samples were obtained by line scans of analyses of matrix areas (see Supplement 2), and then filtered to remove analyses with high FeO (presumably including magnetite and/or fayalite and/or sulfides) and CaO (including Ca-rich phases), as well as those with extremely low totals. (Color figure can be viewed at wileyonlinelibrary.com.)

Chondrules

A CT scan of fragment AhS 91_01 showed that it contained spherical objects that appeared to be chondrules. The fragment was mounted in epoxy and then sectioned conservatively (near its outer surface), revealing four ~140 to 600 μm diameter chondrules (#2–5), along with several clasts of olivine, pigeonite, orthopyroxene, and plagioclase, embedded in C1 material (Fig. 18a). The chondrules are located at the edge of the fragment in this section, without connecting material, so it was not possible to determine their textural relationship to one another or to the C1 material. They vary in internal texture (PO and POP types), mineral compositions (Table 6), and degree of equilibration, and can be described within the standard classification scheme for chondrules in chondritic meteorites (e.g., Gooding and Keil 1981; Brearley and Jones 1998; Jones 2012). Chondrule #2 (Fig. 18b) consists of subhedral, normally zoned olivine phenocrysts in a small amount of feldspathic mesostasis surrounded by a rim of subhedral to anhedral grains of

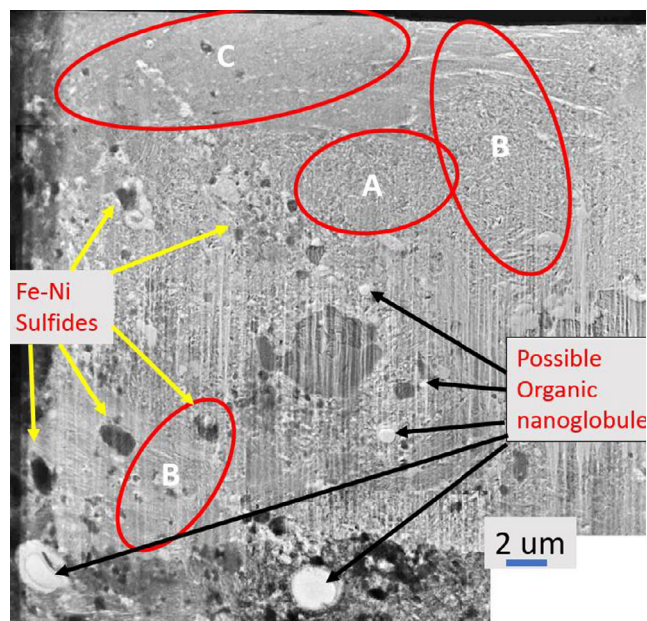


Fig. 7. Low magnification TEM bright-field image of the FIB slice of area 1 in AhS 91A_1. Areas dominated by different phyllosilicate morphologies are indicated (A, B, C). Area A is dominated by poorly crystalline, fibrous phyllosilicate. Area B consists mainly of coarse-grained phyllosilicate. Area C consists mainly of poorly crystalline, spongy phyllosilicate. Some Fe-Ni sulfides are indicated. Possible organic nanoglobules, identified by typical morphology and EDS spectra showing carbon, are indicated. (Color figure can be viewed at wileyonlinelibrary.com.)

orthopyroxene. Olivine and orthopyroxene cores are Fo ~95 and En ~98, respectively (Table 6). It is a partially equilibrated type IAB POP. Chondrule #3 (Fig. 18c) consists dominantly of orthopyroxene phenocrysts (Mg# ~95) with overgrowths of Ca-rich pyroxene, plus subhedral to anhedral grains of FeO-rich olivine (Fo ~80). It is a partially equilibrated Type IAB. Chondrule #4 (Fig. 18d) is a Type IIAB POP consisting of anhedral olivine (Fo ~79) and orthopyroxene (Mg# ~89), with one large metal (kamacite+taenite) grain (Fig. 18e). Chondrule #5 (Fig. 18f) is an unequilibrated Type IAB POP, consisting of zoned, anhedral olivine (Fo 89–99), anhedral orthopyroxene (Mg #99), and mesostasis containing acicular olivine crystals.

The CT scan of AhS 91_01 (Fig. 19a) shows that it contains additional chondrules not yet exposed, some of which are in contact with one another and the C1 matrix. Examining these chondrules could provide information on textural relationships between the chondrules and between the chondrules and the C1 matrix. Therefore, we have begun progressively polishing down the AhS 91_01 section and examining newly exposed features. The first new feature observed is a highly brecciated area (Figs. 19b and 19c), which

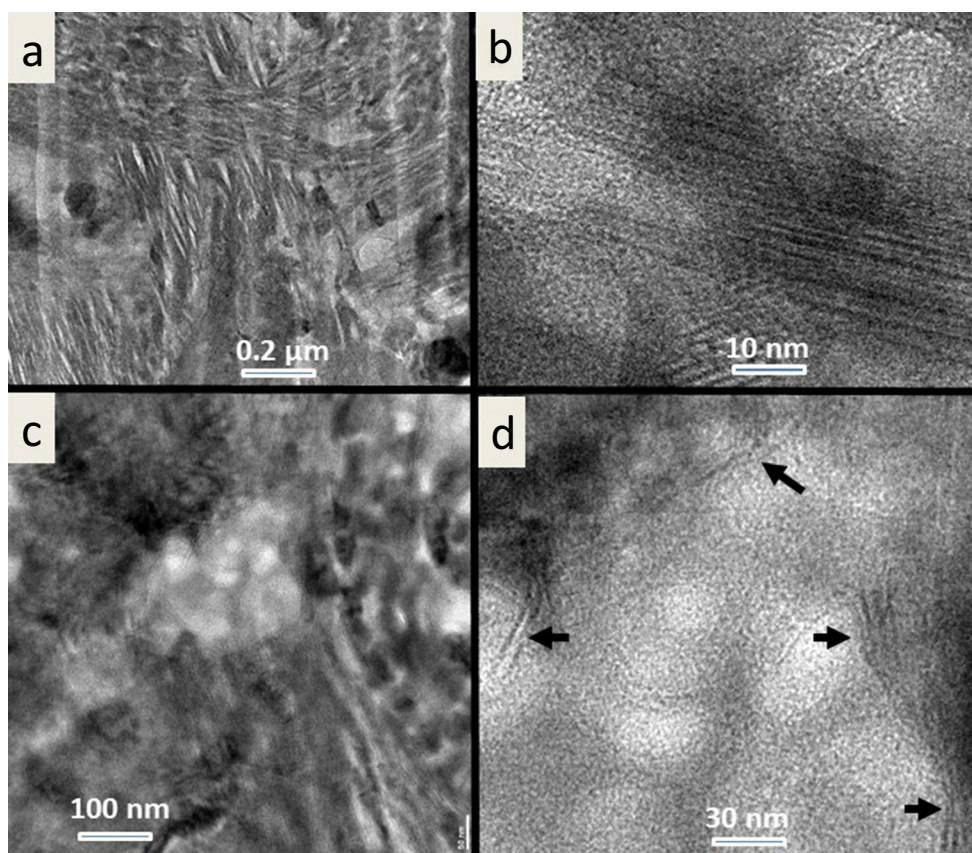


Fig. 8. Higher magnification TEM bright-field images of phyllosilicate morphologies in 91A. a, b) Views of relatively well crystalline phyllosilicates from area B in Fig. 7. Interlayer lattice fringes (lines from upper left to lower right) measuring 1.1–1.3 nm are evident in (b). c, d) Poorly crystalline, spongy phyllosilicates from area C in Fig. 7. d) A few, very thin phyllosilicate crystallites (arrowed), with 1.1–1.3 nm spacings and only two to four sheets thick. (Color figure can be viewed at wileyonlinelibrary.com.)

appeared in the area formerly occupied by chondrule #5 (chondrules #3 and #4 are still present). This area shows finely comminuted material consisting of angular mineral and lithic fragments <1 to 100 μm in size. Based on their textures and mineral compositions (Fig. 19d), these fragments are an intimate mix of C1 matrix material, olivine and pyroxenes similar to the ureilitic clasts in AhS 91A, and chondrule components. The C1 material in this area occurs as distinct clasts, rather than forming a matrix around the ureilitic clasts as it does in other areas of AhS 91A and AhS 671.

Oxygen Isotope Compositions

Oxygen isotope compositions for bulk samples of AhS 91A and AhS 671 (Table 7) are shown in Fig. 20. The analyzed fragment of AhS 91A was separated into a main fragment that was dominated by the C1 lithology and a small chip with a “metallic” texture (based on binocular microscope observation). The main fragment (analyzed as two aliquots) had an average composition plotting on an extension of the CCAM line at

$\delta^{18}\text{O} = 13.53\text{‰}$ and $\delta^{17}\text{O} = 8.93\text{‰}$, with $\Delta^{17}\text{O} = \sim 1.8\text{‰}$. This does not match the composition of any known chondrite, but is very similar to the composition of a CC-like clast from the Nilpena polymict ureilite (Fig. 20a: Clayton and Mayeda 1988; Brearley and Prinz 1992) and similar to compositions of three CC-like clasts in other typical polymict ureilites (Patzek et al. 2018b). An aliquot of the “metallic” chip had a composition plotting on the terrestrial fractionation line (TFL) at $\delta^{18}\text{O} = -1.33$. SEM observations and EMPA analyses of this chip showed only hydrous iron oxides, with a texture indicative of terrestrial alteration products. The fragment of AhS 671 (two aliquots) showed a composition slightly offset from that of AhS 91A, with $\Delta^{17}\text{O} = \sim 1.6\text{‰}$ and slightly lower $\delta^{18}\text{O} = \sim 10.72\text{‰}$. This composition would be consistent with a mixture of AhS 91A and a terrestrial component similar to the chip separated from AhS 91A.

Oxygen isotope compositions obtained by SIMS for various components of AhS 91_01 (Fig. 18a) are given in Table 8 and shown in Fig. 20. Compositions of olivine and pyroxene in chondrules #2 and #4, and pyroxene in chondrule #3 (Fig. 18), are within the range

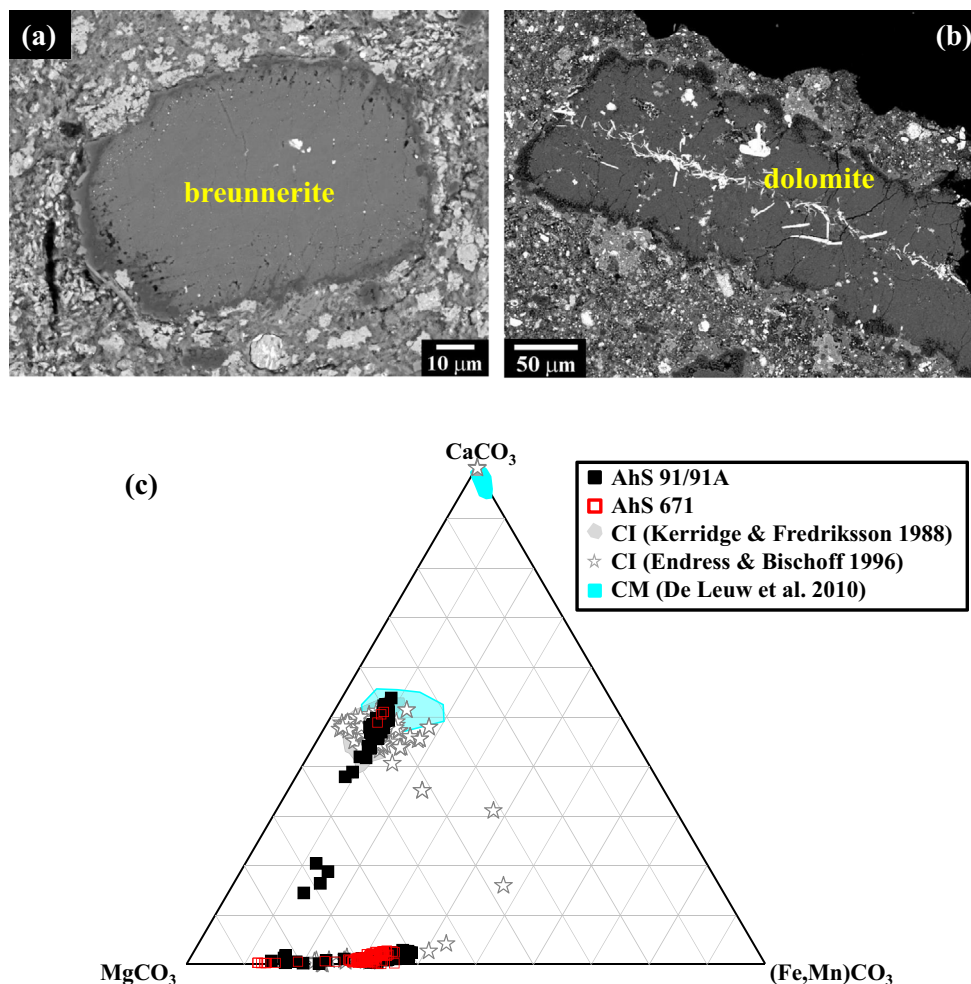


Fig. 9. BEI of large breunnerite grain (a) and large dolomite grain (b) in AhS 91A. Both carbonates have narrow rims of Mg-enriched breunnerite. Dolomite has inclusions of Fe,Ni sulfides. (c) Compositions of carbonates in AhS 91A and AhS 671 in the calcite-magnesite-siderite ternary system, compared with carbonates in various groups of carbonaceous chondrites. Data sources: Fredriksson and Kerridge (1988); Endress and Bischoff (1996); De Leuw et al. (2010). (Color figure can be viewed at wileyonlinelibrary.com.)

of compositions of olivine and pyroxene in chondrules in LL ordinary chondrites (Kita et al. 2010). One analysis of FeO-rich olivine (Fo ~80) in chondrule #3 has a more ^{16}O -rich composition (Fig. 20a), suggesting that it is a relict grain, that is, a remnant of chondrule precursor material that survived the last chondrule-forming melting event (Kunihiro et al. 2004; Ushikubo et al. 2012). Analyses of olivine and pyroxene from chondrule #5 are significantly more ^{16}O -rich (Fig. 20a) than the olivine from chondrules #2, 3, and 4, and are within the range of olivine and pyroxene in chondrules from primitive (type 3) CC (Ushikubo et al. 2012; Tenner et al. 2015). Clasts of olivine, pyroxene, and plagioclase in AhS 91_01 have oxygen isotope compositions within the range of main group ureilites; ureilitic stones from AhS; and olivine, pyroxene, and plagioclase clasts in typical polymict ureilites (Fig. 20a).

Five analyses from the core and zoned rim of a breunnerite grain in the C1 material (Fig. 18a) show $\Delta^{17}\text{O} = -2.3 \pm 0.2\text{‰}$ and form a $\delta^{17}\text{O}$ - $\delta^{18}\text{O}$ line of slope = 0.526 (correlation coefficient 0.999) with $\delta^{18}\text{O} \sim 20$ to 35.6‰ (Fig. 20b).

Bulk Sample Spectroscopy from 0.3 to 3.6 μm

Bulk sample spectra from 0.3 to 3.6 μm for two fragments of AhS 91A (chips and powders of each) are shown in Fig. 21a (RELAB file names are given in Supplement 2). Spectra of the chips are dark (reflectance ~ 0.04 – 0.05) and relatively featureless across VNIR wavelengths. They show a strong absorption band at $\sim 2.7 \mu\text{m}$, indicative of water of hydration (OH^-) in phyllosilicates. Spectra of powdered samples are similar to those of the corresponding chips but having

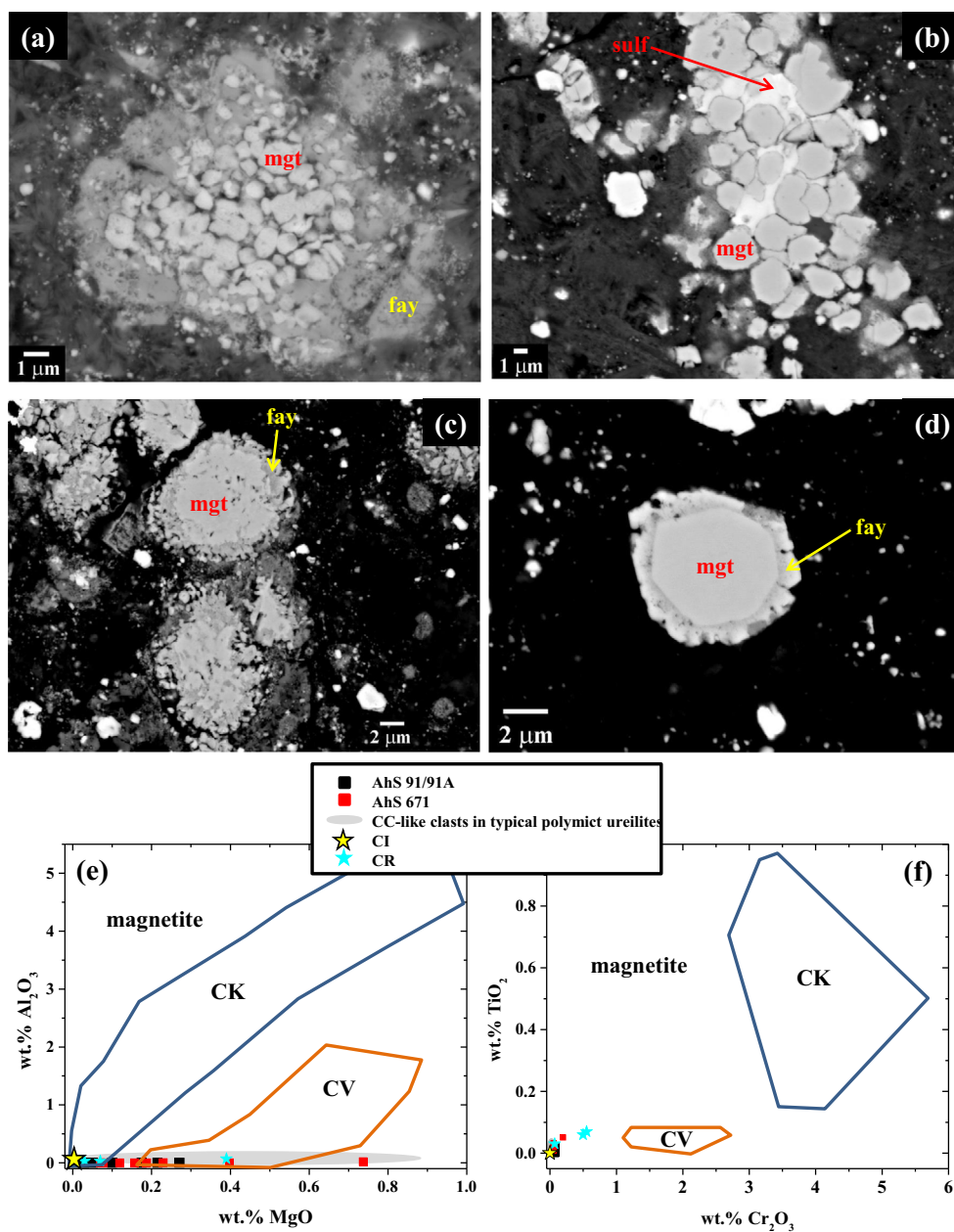


Fig. 10. a–d) BEI showing magnetite (mgt) in AhS 91A, which commonly occurs in clusters of grains having irregular rims of fayalitic olivine (fay), and less commonly in clusters with interstitial sulfide (sulf). e) Plot of wt% MgO versus wt% Al₂O₃ in magnetite in AhS 91A and AhS 671 compared with magnetite in various chondrite groups. f) Plot of wt% Cr₂O₃ versus wt% TiO₂ in magnetite in AhS 91A and AhS 671 compared with magnetite in various chondrite groups. Data for CK and CV from Dunn et al. (2016) and Greenwood et al. (2010); CR from Harju et al. (2014); CC clasts in typical polymict ureilites from Brearley and Prinz (1992) and Goodrich et al. (2019a). (Color figure can be viewed at wileyonlinelibrary.com.)

lower reflectance (~0.03–0.04). The <125 μm powder of one fragment (91A_11) exhibits a shallow absorption at ~1.05 μm, attributable to olivine.

VNIR spectra of chips and powder samples of two AhS enstatite chondrites, AhS 2012 and AhS 1002 (Goodrich et al. 2018), measured to add to the data of Hiroi et al. (2010) for spectra of AhS stones, are also

shown in Fig. 21b. Both chips have very red, featureless slopes, with high reflectance values (~0.27–0.28 at 0.55 μm). The powders are also red and featureless, but with lower reflectance (0.08–0.09 at 0.55 μm). The AhS 1002 samples are more affected by terrestrial weathering than AhS 2012, evident from their stronger UV and 0.5 μm absorption features.

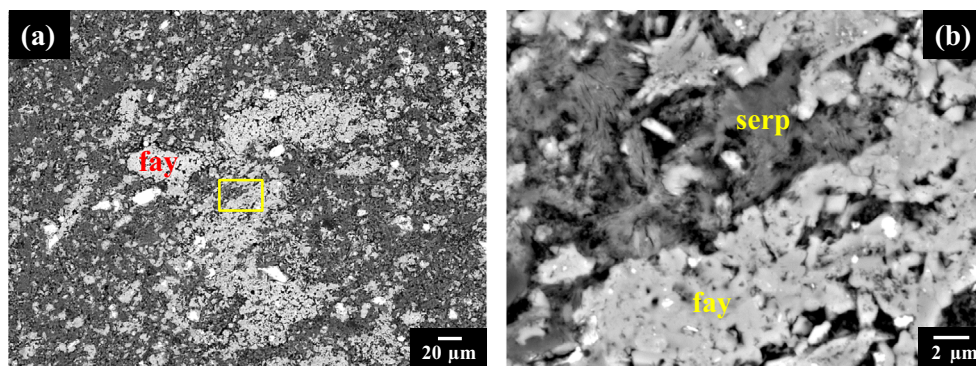


Fig. 11. BEI of area of AhS 671 with flaky, porous, fayalitic olivine (fay) of Fo 28–42 intergrown with phyllosilicates dominated by serpentine (serp). Area of (b) is marked in (a). (Color figure can be viewed at wileyonlinelibrary.com.)

Table 1. Compositions of phases in C1 matrix of AhS 91A and AhS 671 from EMPA.

	Phyllosilicate(s) ^a						Ca-rich silicate phase		Fayalitic olivine ^b
	AhS 91A_01		AhS 91A_01		AhS 671_03	AhS 671_03		AhS 91A_01	AhS 671_03
	Avg. (23)	SD	Avg. (47)	SD	(1)	Avg. (5)	SD	(1)	Avg. (4)
SiO ₂	39.7	2.4	39.3	2.1	36.2	37.7	3.5	48.9	30.4
TiO ₂	bdl		0.04	0.04	0.03	bdl		bdl	0.07
Al ₂ O ₃	3.8	0.5	2.6	1.0	4.7	4.1	0.3	4.1	0.10
Cr ₂ O ₃	1.3	0.1	0.90	0.37	1.1	0.72	0.23	0.39	0.20
FeO	11.8	0.7	13.2	2.0	14.6	17.9	1.3	7.4	50.5
MgO	31.7	2.2	29.8	2.3	30.8	24.2	2.7	17.7	17.6
MnO	0.14	0.02	0.16	0.03	0.07	0.19	0.04	0.33	0.23
CaO	0.18	0.06	0.25	0.22	0.04	0.40	0.12	15.0	0.13
Na ₂ O	0.44	0.18	0.51	0.27	0.13	0.15	0.04	2.7	0.05
K ₂ O	0.07	0.05	0.07	0.03	bdl	0.05	0.06	bdl	bdl
P ₂ O ₅	0.08	0.03	0.07	0.04	bdl	0.56	0.20	na	0.73
NiO	0.04	0.02	0.12	0.10	1.3	1.2	0.3	0.10	0.51
Total	89.2	1.8	87.0	1.4	89.0	87.2	5.1	96.6	100.5
FeS ^c	0.05	0.05	0.26	0.31	2.4	0.3	0.1	1.2	0.50

bdl = below detection limit; na = not analyzed.

^aAnalyses of phyllosilicates are broad beam (2 μm) analyses obtained in profiles across matrix areas, and were filtered to remove analyses with high CaO (assumed to include the Ca-rich phase) and FeO (assumed to include magnetite and/or fayalite). They appear to be dominantly mixtures of serpentine and saponite but may include minor phases.

^bOlivine is porous and has many tiny inclusions of unidentified phases, hence stoichiometry is not perfect for olivine.

^cS was measured as SO₃; analyses were recalculated assuming all S was in FeS and adjusting FeO accordingly.

Microscopic Spectroscopy from 2.5 to 25 μm

We acquired μ-FTIR reflectance measurements on polished mounts of AhS 91A and AhS 671 in the 4000–400 cm⁻¹ range (2.5–25 μm). Microscopic measurements enable the targeted analysis of minerals and clasts of interest as well as allowing for mapping to obtain a bulk sample spectrum that represents coarse to solid rock (non volume scattering) surfaces. Analytical spot sizes typically varied from ~100 to 300 μm².

A spectrum representing bulk or whole-rock 91A_1 was obtained by automated mapping of the sample at 200 μm² spatial resolution in a 10 × 9 array. After removal of pixels that did not fall completely on the

sample area, 65 spectra remained, which we averaged to obtain the bulk spectrum due to the linear nature of mixing over this spectral range. Figure 22 shows this bulk spectrum compared to similarly acquired spectra of selected carbonaceous chondrites (Hamilton 2018; Hamilton et al. 2018). Like many of the CI and CM chondrites, the bulk spectrum of AhS 91A_1 exhibits an OH⁻ band at ~3686 cm⁻¹ (~2.71 μm) indicative of the presence of serpentine group phyllosilicates. The Christiansen feature (CF), a minimum on the high wave number side of the silicate stretching peak, is located at ~1097 cm⁻¹/~9.12 μm (at 2 cm⁻¹ spectral sampling). This position lies between the CF positions of typical CII and CM meteorites, and is most consistent with

Table 2. Compositions of carbonates in AhS 91A and AhS 671 from EMPA.

	Large breunnerite AhS 91A		Large dolomite AhS 91A		Large breunnerite AhS 671		Rim on breunnerite	Small breunnerite
	Avg. (111)	SD	Avg. (49)	SD	Avg. (87)	SD		
FeO	19.3	0.9	4.8	0.6	18.1	1.6	9.1	9.2
MgO	27.1	1.1	18.3	1.2	28.8	1.0	40.0	39.7
MnO	6.4	1.5	2.0	0.5	5.5	1.9	0.8	1.2
CaO	1.0	0.3	28.4	1.6	0.9	0.5	0.22	0.19
CO ₂ *	46.2	0.3	46.5	0.2	46.7	0.3	49.9	49.8
Total	100.0		100.0		100.0		100.0	100.0
Magnesite	0.64	0.02	0.43	0.03	0.67	0.02	0.88	0.87
Siderite	0.26	0.01	0.06	0.01	0.24	0.02	0.11	0.11
Rhodochrosite	0.09	0.02	0.03	0.01	0.07	0.03	0.01	0.02
Calcite	0.01	0.01	0.48	0.03	0.02	0.01	0.00	0.00

*CO₂ was not analyzed. Analyses were recalculated assuming that CO₂ = 100%—analytical total, and then checked for carbonate stoichiometry. Concentrations of Si, Al, Cr, Ti, and Na were near or below detection limit.

Table 3. Compositions of magnetite in AhS 91A and AhS 671 from EMPA.

	AhS 671_02		AhS 91A_02	
	Avg (6)	SD	Avg (5)	SD
SiO ₂	0.11	0.07	0.08	0.04
TiO ₂	0.02	0.02	0.02	0.00
Al ₂ O ₃	bdl		bdl	
Cr ₂ O ₃	0.08	0.06	0.08	0.01
FeO	30.9	0.2	30.8	0.1
Fe ₂ O ₃	68.8	0.4	68.5	0.2
MgO	0.22	0.26	0.04	0.04
MnO	0.27	0.25	0.02	0.02
CaO	bdl		bdl	
NiO	0.06	0.04	0.06	0.03
Total	100.5		99.6	

Analyses recalculated assuming molar Fe²⁺/Fe³⁺ = 2/3.

petrologic type 1, 1/2, or low petrologic subtype CM2 chondrites (Hamilton et al. 2018). The shape of the Si-O stretching region from the CF to ~695 cm⁻¹/~14.4 μm is relatively broad, exhibits modest structure in the form of several small shoulders (at 944, 877, and 827 cm⁻¹/10.59, 11.40, and 12.09 μm), and is not particularly well matched by any available meteorites in our collection. The broadened absorption of the bulk spectrum may suggest the presence of an amorphous component. The smaller shoulders are attributable to a few pixels in the 91A_1 map to which pyroxene (one pixel) and fayalitic (not ureilitic) olivine contribute. Continuing across the spectrum, there is a slightly asymmetric Mg-OH absorption at ~616 cm⁻¹ (16.23 μm) whose shape and position are most similar to CM1, CM1/2, and low petrologic type CM2 meteorites. The Si-O bending fundamental is located at 443 cm⁻¹ in AhS 91A_1 and,

not surprisingly, also bears strong similarities to the shape and position of the same feature in CI and CM1, CM1/2, and low petrologic type CM2 meteorites (Hamilton et al. 2018). Comparable spectra of CM 2.5–2.7 meteorites exhibit a lower wave number band minimum (~426 cm⁻¹/23.47 μm) and additional structure in this region (e.g., a small minimum at ~490 cm⁻¹/20.41 μm) due to the greater abundances of pyroxene and olivine they contain (e.g., Howard et al. 2015).

We also made targeted spectral measurements of areas 1 and 4 of AhS 91A_1 (Fig. 3a). Area 1 has a very consistent and feature-rich spectral shape that differs considerably from that of the bulk meteorites (Fig. 23). The area 1 spectrum has no discernible OH⁻ band and the Si-O stretching region (1120–625 cm⁻¹; 8.9–16.0 μm) looks quite similar to the platy or lath-like, fayalitic olivine-dominated matrix materials in CV3_{ox} meteorites (e.g., Hamilton and Connolly 2012), although the Si-O bending region (<625 cm⁻¹; >16.0 μm) resembles olivine mixed with a small amount of phyllosilicate. These observations indicate the presence of one or more anhydrous compositions, consistent with the observed high abundance in area 1 of the Ca-rich silicate that is inferred from EMPA to be nearly anhydrous. It is also noteworthy that the minimum reflectance (values not shown in Fig. 23) of the bulk sample at the CF position is 4% whereas the reflectance of area 1 at the CF is ~16%—this overall brightening commonly occurs due to the presence of spectrally neutral (in this region of the TIR) phases, such as metal and sulfide (Hamilton et al. 2018). This can be explained by a high abundance of sulfides seen in petrographic observations of area 1. We also collected an oversampled spectral map (100 μm/pixel at 25 μm spatial sampling) of area 1 in the hopes of

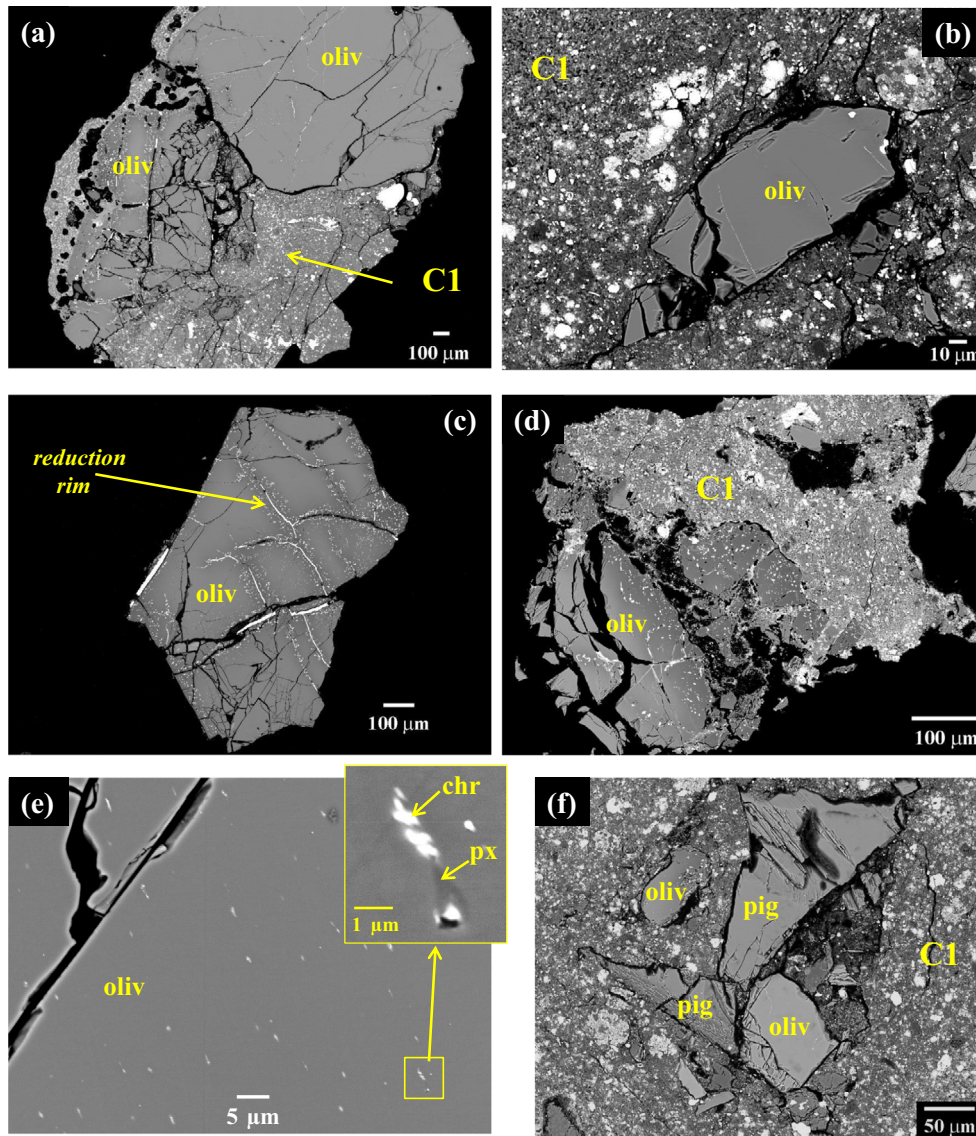


Fig. 12. BEI showing clasts of ureilitic olivine (oliv) and pigeonite (pig) enclosed by or in direct contact with C1 material in AhS 91A and AhS 671. Olivine clasts in (a,c,d) show reduction rims (Mg-enriched olivine containing tiny grains of metal), which are a characteristic feature of ureilite olivine. Olivine clast of Fo 78 shown in (e) contains submicron-sized lamellar exsolutions of chromite (chr) + pyroxene (px), a feature that has been observed in olivine of Fo 75–78 in ureilites. Samples: (a) AhS 91A_2A; (b) AhS 91A_6A; (c) AhS 91A_2B; (d) AhS 671_4-17; (e) AhS 91A_2A; (f) AhS 91A_9. (Color figure can be viewed at wileyonlinelibrary.com.)

extracting the individual component spectra using a statistical approach (factor analysis) demonstrated successfully for laboratory and remote sensing data (e.g., Bandfield et al. 2002; Hamilton and Ruff 2012). Using this approach, we recovered the spectrum of an olivine-like (Fo 55) component, but no other components, including crystalline serpentines or phyllosilicate minerals (for phyllosilicates, we searched using a test suite of spectra for samples that have been measured at temperatures ranging from ambient to as much as 900 °C: Che et al. 2011). If a disordered phyllosilicate

(serpentine or clay mineral) and/or CaO component are present in area 1, as suggested based on TEM data, we do not have the correct trial spectra to extract those components from the measured AhS spectra. If these materials are present and intergrown at very small scales ($\ll 25 \mu\text{m}$), we also may not be able to extract their signatures with this analytical approach, which requires variability in the phase proportions between individual measurement spots/pixels.

The spectrum of AhS 91A_1, area 4 exhibits a feature at $\sim 3687 \text{ cm}^{-1}/2.71 \mu\text{m}$ (at 4 cm^{-1} sampling) that

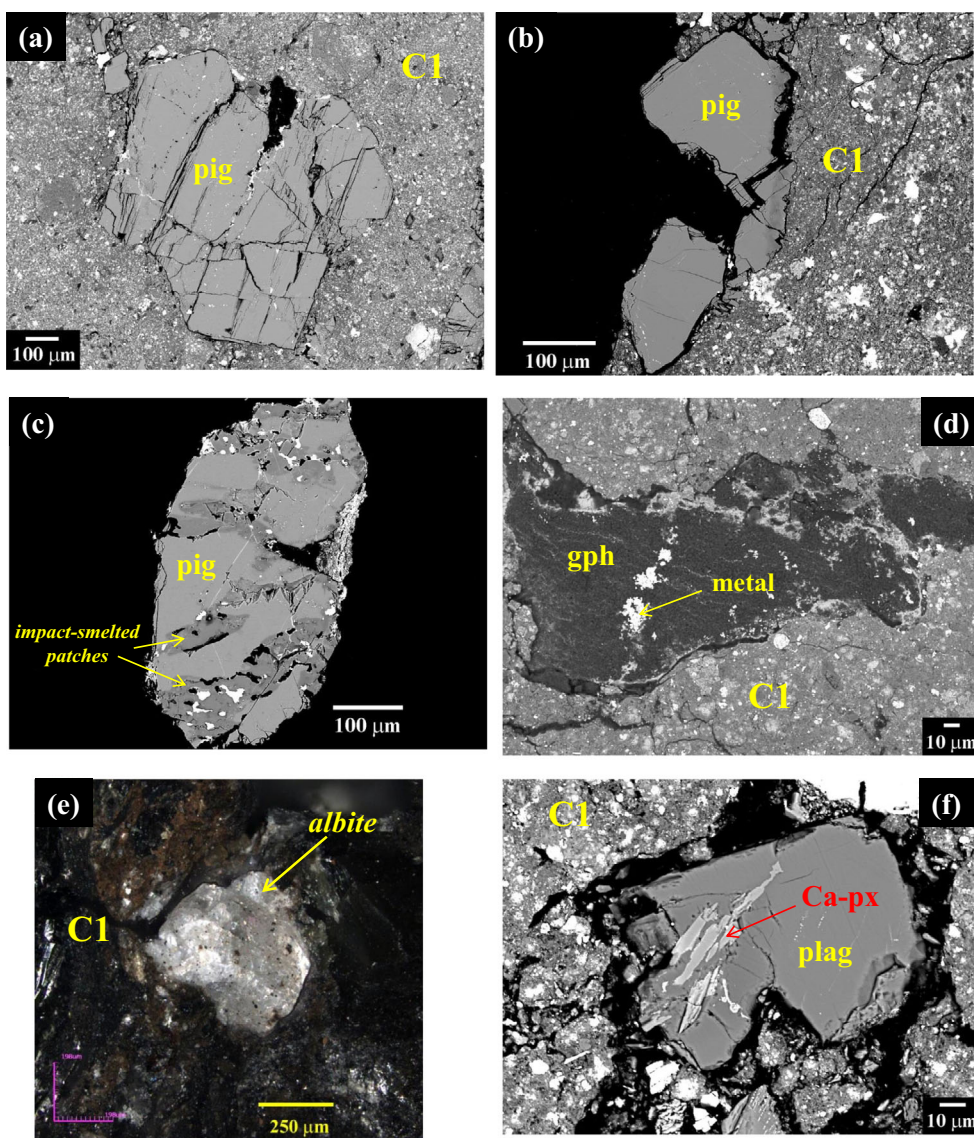


Fig. 13. BEI showing clasts of ureilitic pigeonite (a, b, c), graphite (d), and plagioclase (e, f) in AhS 91A and AhS 671. e) Optical (stereo microscope) image of albite grain in CI material in AhS 91A. This grain was first observed on surface of the fragment, as shown here. It subsequently fell out and was mounted separately for EMPA. Pigeonite in (c) shows patches of impact-smelted texture, characterized by reduced composition, blebs of metal, and pores (black), which is common in pigeonite in Almahata Sitta ureilites. Samples: (a) AhS 91A_9; (b) AhS 91A_6B; (c) AhS 671_4-6; (d) AhS 91A_9; (e) AhS 91A_3; (f) AhS 91_1. pig = pigeonite; gph = graphite; plag = plagioclase; Ca-px = Ca-rich pyroxene. (Color figure can be viewed at wileyonlinelibrary.com.)

is attributable to the fundamental hydroxyl stretching vibration in serpentines (Farmer 1974; Bishop et al. 2002). At lower wave numbers (longer wavelengths), area 4 exhibits a distinct spectral shape (Fig. 24) that is shifted relative to a terrestrial saponite and more consistent with minerals of the serpentine group, including an Mg-OH-related band at $\sim 641\text{ cm}^{-1}/15.6\text{ }\mu\text{m}$ that generally is not present in other magnesian phyllosilicate group minerals (Michalski et al. 2006). The CF minimum and silicate stretching band features of cronstedtite (Fe-bearing serpentine) are shifted (~ 60 –

70 cm^{-1}) to lower wave numbers than in Mg-rich serpentines and other features of cronstedtite are not apparent in the AhS area 4 spectrum (Fig. 24), indicating that the AhS composition is relatively magnesian, consistent with EMPA analyses from this area (Fig. 6).

Targeted spot analyses on AhS 671_2 and AhS 671_3 reveal the spectral character of carbonate (Figs. 25a and 25b) and mixed phyllosilicate/olivine (Figs. 25c and 25d). The positions of spectral peaks in spectra of carbonate are at 1506 , 898 , and 742 cm^{-1} (6.64 , 11.14 , and $13.48\text{ }\mu\text{m}$); a large feature is present at the lowest wave numbers (longest

Table 4. Representative compositions of ureilitic mineral clasts in AhS 91A and AhS 671 from EMPA.

	1	2	3	4	5	6	7	8	9	10	11	12	13	14	15	16	17	18
	ol core	ol	ol	pyx	pyx	pyx	pyx	pyx	pyx	pyx	pyx	plag	plag	plag				
Avg.	Avg.	Avg.	Avg.	Avg.	Avg.	reduc.	reduc.	Avg.	Avg.	Avg.	Avg.	Avg.	Avg.	Avg.	Avg.	Avg.	Avg.	Avg.
(4)	(11)	(49)	(11)	(11)	(1)	rim	rim	(12)	(8)	(7)	(6)	(27)	(1)	(5)	(7)	(3)	(4)	(4)
SiO ₂	38.6	38.7	39.0	39.7	40.3	40.4	42.2	54.1	54.9	54.3	55.9	55.8	56.1	55.8	60.0	67.5	68.2	59.5
TiO ₂	bdl	bdl	bdl	bdl	bdl	bdl	bdl	0.07	0.05	0.10	0.05	0.07	0.15	0.16	0.06	bdl	0.10	bdl
Al ₂ O ₃	bdl	bdl	bdl	bdl	bdl	bdl	bdl	1.01	0.56	0.92	0.38	0.46	0.99	1.16	0.11	20.2	21.4	25.8
Cr ₂ O ₃	0.71	0.47	0.76	0.74	0.57	0.44	0.17	1.20	1.07	1.17	1.07	1.10	1.03	0.97	0.02	bdl	bdl	bdl
FeO	22.6	20.1	19.5	15.0	12.0	9.8	0.93	12.9	13.2	11.3	11.0	9.3	7.5	7.4	0.39	0.05	0.06	0.39
MgO	38.7	39.8	41.2	44.6	47.4	47.9	55.2	24.9	26.2	25.5	28.4	28.6	29.4	31.2	39.5	0.01	0.01	0.11
MnO	0.41	0.41	0.44	0.45	0.5	0.49	0.26	0.39	0.39	0.42	0.42	0.46	0.53	0.56	0.10	bdl	bdl	0.02
CaO	0.38	0.26	0.40	0.32	0.44	0.26	0.14	4.9	4.0	5.1	3.4	4.2	5.2	2.4	0.45	0.62	1.1	7.2
Na ₂ O	bdl	bdl	bdl	bdl	bdl	bdl	bdl	0.05	0.04	0.06	0.05	0.02	0.04	0.04	0.02	11.1	10.6	7.3
NiO	bdl	bdl	bdl	bdl	bdl	bdl	bdl	bdl	bdl	bdl	bdl	bdl	bdl	bdl	bdl	na	bdl	bdl
K ₂ O	na	na	na	na	na	na	na	na	na	na	na	na	na	na	na	0.56	0.72	0.06
Total	101.4	99.7	101.3	100.8	101.2	99.3	98.9	99.5	100.4	98.9	100.7	100.0	100.9	99.7	100.7	100.0	102.0	100.4
Mg#	75.3	78.0	79.0	84.1	87.5	89.7	99.1	77.5	77.9	80.0	82.2	84.5	87.5	88.3	99.5			
Wo								9.8	7.9	10.3	6.6	8.2	9.9	4.6	0.8			
An																2.9	5.2	35.2
Or																3.2	4.1	0.4

Numbers in parentheses are number of analyses in the average.

Mg# = $100 \times \text{molar MgO} / (\text{MgO} + \text{FeO})$; Wo = $100 \times \text{molar CaO} / (\text{CaO} + \text{FeO} + \text{MgO})$; An = $100 \times \text{molar CaO} / (\text{CaO} + \text{Na}_2\text{O} + \text{K}_2\text{O})$; Or = $100 \times \text{molar K}_2\text{O} / (\text{CaO} + \text{Na}_2\text{O} + \text{K}_2\text{O})$.

ol = olivine; pyx = pyroxene; reduc. = reduction; plag = plagioclase.

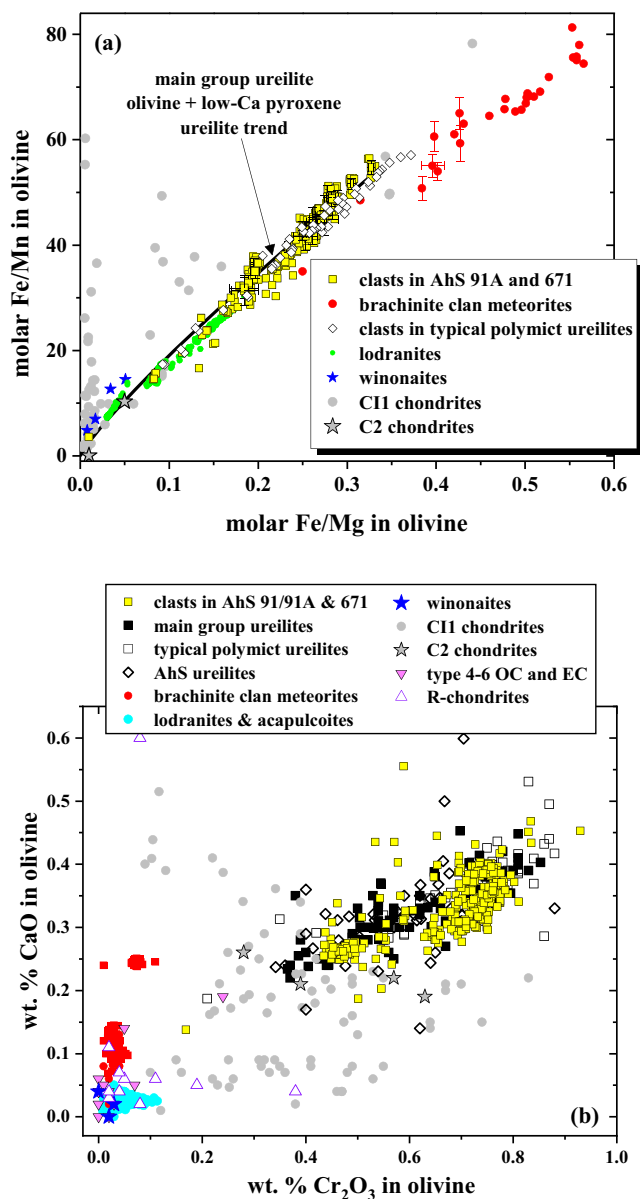


Fig. 14. Compositions of olivine clasts in AhS 91A and AhS 671 compared with olivine in other groups of meteorites. a) Plot of molar Fe/Mg versus Fe/Mn. b) Plot of wt% Cr₂O₃ versus wt% CaO. In combination, these two plots show that olivine in main group ureilites, typical polymict ureilites, and ureilitic stones from Almahata Sitta show a characteristic compositional range, which distinguishes them from olivine in other groups of achondrites and most chondrites. The olivine clasts in AhS 91A and AhS 671 are consistent with ureilitic compositions. Data sources as follows. Acapulcoites and lodranites: Nagahara (1992); Takeda et al. (1994); Papike et al. (1995); Mittlefehldt et al. (1996); Buroni and Folco (2008); Goodrich et al. (2011). Brachinite clan meteorites: Nehru et al. (1983); Warren and Kallemeyn (1989); Petaev et al. (1994); Delaney et al. (2000); Goodrich and Righter (2000); Mittlefehldt et al. (2003); Goodrich et al. (2006, 2011, 2017c); Gardner-Vandy et al. (2012, 2013); Day et al. (2015). Winonaites/IAB silicates: Kimura et al. (1992); Benedix et al. (1998). Main group ureilites: Goodrich et al. (1987, 2001, 2006, 2013a, 2014); Takeda (1987, 1989); Treiman and Berkley (1994); Goodrich and Righter (2000); Inoue et al. (2016); Singletary and Grove (2003); Weber et al. (2003); Warren and Rubin (2011). Typical polymict ureilites: Downes et al. (2008). C1 chondrites: Steele (1990); Leshin et al. (1997); Frank et al. (2014). C2 chondrites: Brearley and Jones (1998). Type 4-6 OC and EC: Brearley and Jones (1998). R-chondrites: Bischoff et al. (2011). (Color figure can be viewed at wileyonlinelibrary.com.)

spectra in both 91A_2 and AhS 671_3 are more akin to those in the matrices of petrologic type 3 carbonaceous chondrites, as opposed to chondrule olivines, a property that may be indicative of their tabular and porous nature, as well as composition.

Noble Gas Analyses

The noble gas results are given in Tables 9–12. The isotopic compositions of all elements He–Xe can be explained with a mixture of cosmogenic (cos), primordially trapped (tr), and radiogenic (rad; very minor ⁴He, ⁴⁰Ar, and ¹²⁹Xe from decay of U, Th, ⁴⁰K, and ¹²⁹I) noble gases, as is expected for both primitive chondritic and ureilitic material (e.g., Ott 2014). In detail, cosmogenic noble gases are best visible in ²¹Ne. The trapped noble gases of phase Q or a related “ureilitic” component (e.g., Göbel et al. 1978) dominate ³⁶Ar, ³⁸Ar, and all Kr and Xe isotopes. Trapped HL (heavy- and light-enriched) gases from presolar diamonds (Huss and Lewis 1994) might contribute to the He and Ne isotopic compositions. The Ne three isotope plot (Fig. 26) shows the three fragments plotting on an apparent mixing line between trapped Ne and the cosmogenic endmember. The spread of the data points illustrates the distinct mixing ratios of the trapped and cosmogenic Ne.

Using Ne with trapped and cosmogenic endmember compositions ($^{20}\text{Ne}/^{22}\text{Ne}_{\text{tr}} = 10.46 \pm 0.05$ (from fit through the data using $^{21}\text{Ne}/^{22}\text{Ne}_{\text{tr}} = 0.0294$; Busemann et al. 2000) and $^{21}\text{Ne}/^{22}\text{Ne}_{\text{cos}} = 0.789 \pm 0.016$ for a

wavelengths), but the peak position is not clearly evident in our data and likely lies just beyond the 400 cm⁻¹/25 μm limit of these data. The observed feature positions are consistent with a carbonate with an intermediate Mg-Fe composition (e.g., Lane and Christensen 1997) and is similar to magnesite and dolomite (we do not have a brunnerite spectrum for comparison), consistent with EMPA results (Fig. 9). To extract the individual mineral spectra from the mixed olivine/phyllsilicate analyses, we employed factor analysis on data collected as an oversampled (100 μm spot size, 50 μm spatial resolution) 16 × 15 map on a portion of AhS 671_03. We successfully extracted spectra consistent with magnesian serpentines (Fig. 25e) and olivine (~Fo 30–40, consistent with EMPA results, Fig. 25f). The shape of the olivine

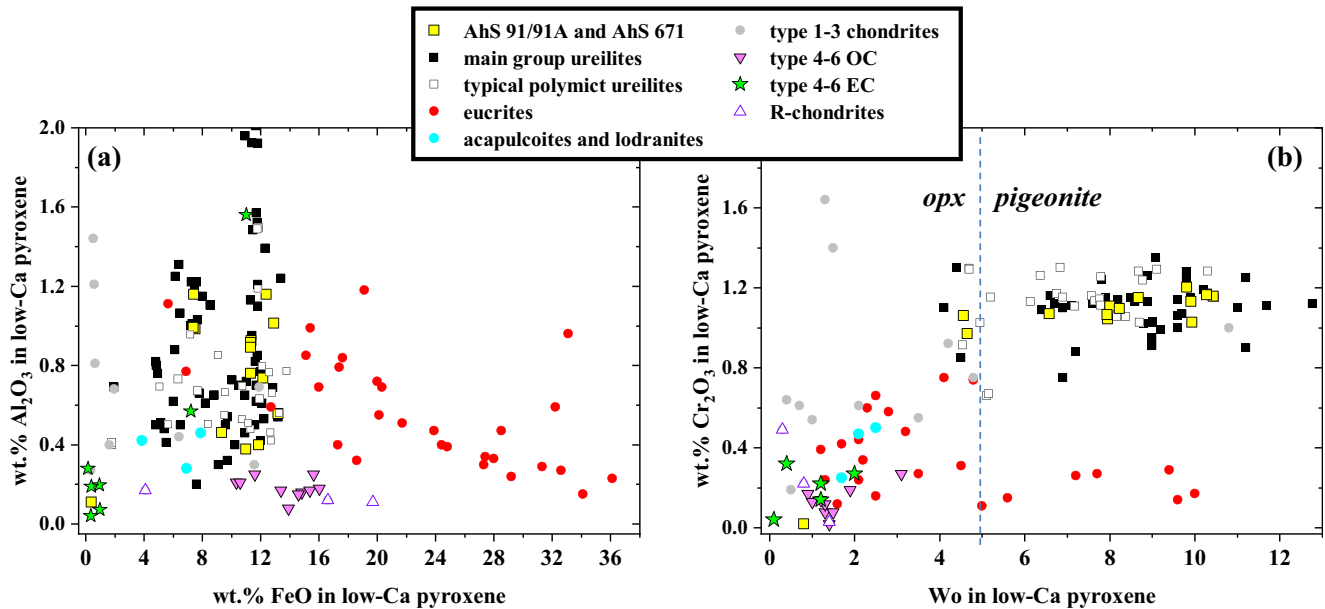


Fig. 15. Compositions of low-Ca pyroxene clasts in AhS 91A and AhS 671 compared with low-Ca pyroxenes in other groups of meteorites. a) wt% FeO versus wt% Al_2O_3 . b) Wo content (molar $\text{CaO}/[\text{CaO} + \text{FeO} + \text{MgO}]$) versus wt% Cr_2O_3 . These two plots show that low-Ca pyroxenes in main group ureilites, typical polymict ureilites, and ureilitic stones from Almahata Sitta are well distinguished from those in other groups of meteorites. With one exception, the pigeonite and orthopyroxene clasts in AhS 91A and AhS 671 are consistent with the ureilite fields (the boundary between pigeonite and orthopyroxene is defined compositionally at $\text{Wo} = 5$). One orthopyroxene clast of very low Wo content is out of the range of ureilites and consistent with orthopyroxene in type 4–6 enstatite chondrites. Data sources as follows. Main group ureilites: Goodrich et al. (1987, 2001, 2009, 2013a, 2014); Takeda (1987, 1989); Takeda et al. (1989); Treiman and Berkley (1994); Weber et al. (2003); Singletary and Grove (2003); Inoue et al. (2016). Typical polymict ureilites: Downes et al. (2008); Acapulcoites and lodranites: Mittlefehldt et al. (1998); Eucrites: Mittlefehldt et al. (1998); R-chondrites: Bischoff et al. (2011). Other chondrites: Brearley and Jones (1998). (Color figure can be viewed at wileyonlinelibrary.com.)

Table 5. Compositions of metal and sulfide in metal-sulfide clasts in AhS 91A and AhS 671 from EMPA.

	Clast ^a	Chondrule #4 ^b		Clast ^c			Metal grain with inclusions ^d			
		Ureilitic Kamacite	Kamacite Avg. (2)	Troilite	Kamacite Avg. (6)	Taenite Avg. (3)	Troilite	Kamacite Avg. (15)	SD	Niningerite inclusions Avg. (2)
Mg	bdl	bdl	bdl	bdl	bdl	bdl	bdl			12.0
Si	0.47	0.05	0.04	0.03	0.03	0.03	3.0	0.1		0.27
P	0.24	bdl	bdl	bdl	bdl	bdl	0.12	0.01		bdl
S	bdl	bdl	36.1	bdl	bdl	37.0	bdl			40.9
Ca	bdl	bdl	bdl	bdl	bdl	bdl	bdl			1.3
Ti	bdl	bdl	bdl	bdl	bdl	bdl	bdl			0.06
V	bdl	bdl	bdl	bdl	bdl	bdl	bdl			bdl
Cr	0.23	0.02	0.03	0.03	0.08	0.04	bdl			1.6
Mn	bdl	bdl	bdl	bdl	bdl	bdl	bdl			4.6
Fe	92.5	91.9	59.2	93.0	79.0	61.2	87.8	0.9		36.7
Co	0.36	0.46	0.19	0.49	0.20	bdl	0.33	0.02		0.02
Ni	4.2	6.9	2.5	5.8	19.8	0.24	8.2	0.1		0.26
Total	98.0	99.3	98.0	99.4	99.1	98.5	99.5	1.0		97.7

^{a,d}AhS 91A_09.

^{b,c}AhS 91_01.

typical $(^{20}\text{Ne}/^{22}\text{Ne})_{\text{cos}}$ range from 0.70 to 0.93 (e.g., Wieler 2002), we determined $^{20}\text{Ne}_{\text{tr}}$ and $^{21}\text{Ne}_{\text{cos}}$ concentrations for each of the AhS 91A fragments (Table 9). Using a physical model that predicts the production rates of cosmogenic

nuclides as a function of chemical composition and shielding conditions (Leya and Masarik 2009), with two different estimates of bulk composition for AhS 91A (CI chondrite and ureilitic), we calculated cosmic ray exposure

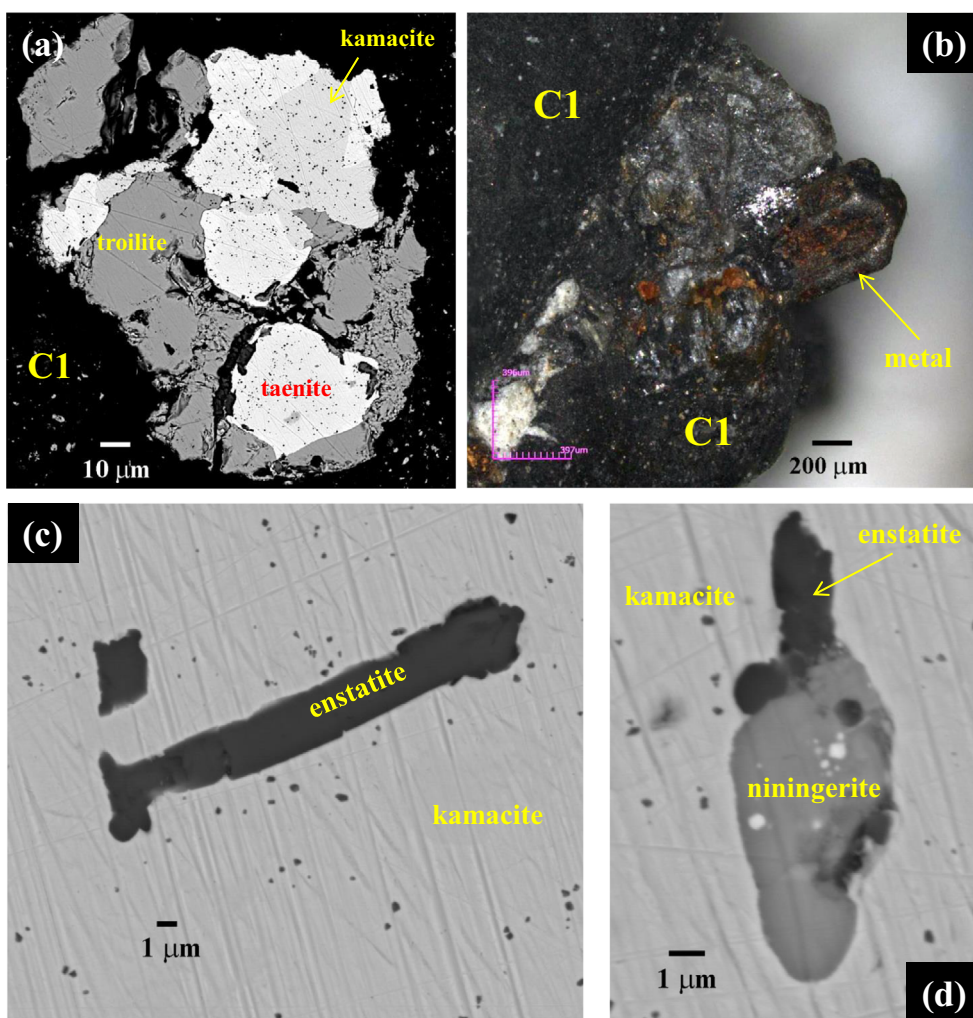


Fig. 16. a) BEI of kamacite-troilite-metal assemblage surrounded by C1 matrix material in AhS 91_1 (see Fig. 18a for location). Texture and compositions (Table 5) of this assemblage are consistent with derivation from an ordinary chondrite. b) Optical (stereo microscope) image of an elongated grain (1.2 mm long) of Si-bearing kamacite embedded in C1 material in AhS 91A_9. The grain subsequently fell out and was mounted separately for EMPA. Its composition (Table 5) is consistent with derivation from an EH chondrite. c and d) = BEI showing inclusions of enstatite and niningerite within the metal grain shown in (b). (Color figure can be viewed at wileyonlinelibrary.com.)

(CRE) ages (Table 13). The frequently used shielding indicator $(^{22}\text{Ne}/^{21}\text{Ne})_{\text{cos}}$ is not appropriate for large bodies like 2008 TC₃ (average ~4 m diameter) and the production rates were averaged over most of the expected shielding depths in the asteroid (see Riebe et al. [2017a] for more details). The $^3\text{He}/^4\text{He}$ ratios are between 6 and 11×10^{-4} (Table 9), close to the trapped HL or Q range ($\sim 1.5 \times 10^{-4}$, e.g., Ott 2014). Thus, $^3\text{He}_{\text{cos}}$ cannot reliably be determined because most ^3He is trapped and some ^4He might be radiogenic. Similarly, the $^{36}\text{Ar}/^{38}\text{Ar}$ ratios of >5.20 suggest only very small, if any, contributions from $^{38}\text{Ar}_{\text{cos}}$. Using $(^{36}\text{Ar}/^{38}\text{Ar})_{\text{cos}} = 0.65 \pm 0.02$ (Wieler 2002) and $(^{36}\text{Ar}/^{38}\text{Ar})_{\text{tr}}$ in the range 5.31–5.36 (Q or air, Busemann et al. 2000) yields only very small concentrations of $^{38}\text{Ar}_{\text{cos}}$ (Table 10) with very large errors,

so we do not use $^{38}\text{Ar}_{\text{cos}}$ to determine CRE ages. Similarly, significant amounts of ^3He may originate from trapped He components, and some ^4He might be radiogenic. This renders the determination of CRE ages based on ^3He very difficult. The most reliable CRE ages, from ^{21}Ne , averaged over both estimated chemical compositions, are between 5 and 9 Ma, lower than the ages of ~11–22 Ma reported for other AhS stones (Welten et al. 2010; Meier et al. 2012; Riebe et al. 2017a).

Krypton and Xe isotope ratios (Tables 11 and 12) resemble purely trapped ratios as typical for phase Q Kr and Xe (Busemann et al. 2000). The element abundances and ratios in AhS 91A_12 and AhS 91A_15 are very similar, whereas AhS 91A_14 shows large enrichments in Ar (~11×), Kr (~2.9×), Ne (~2.5×), and He (~1.4×)

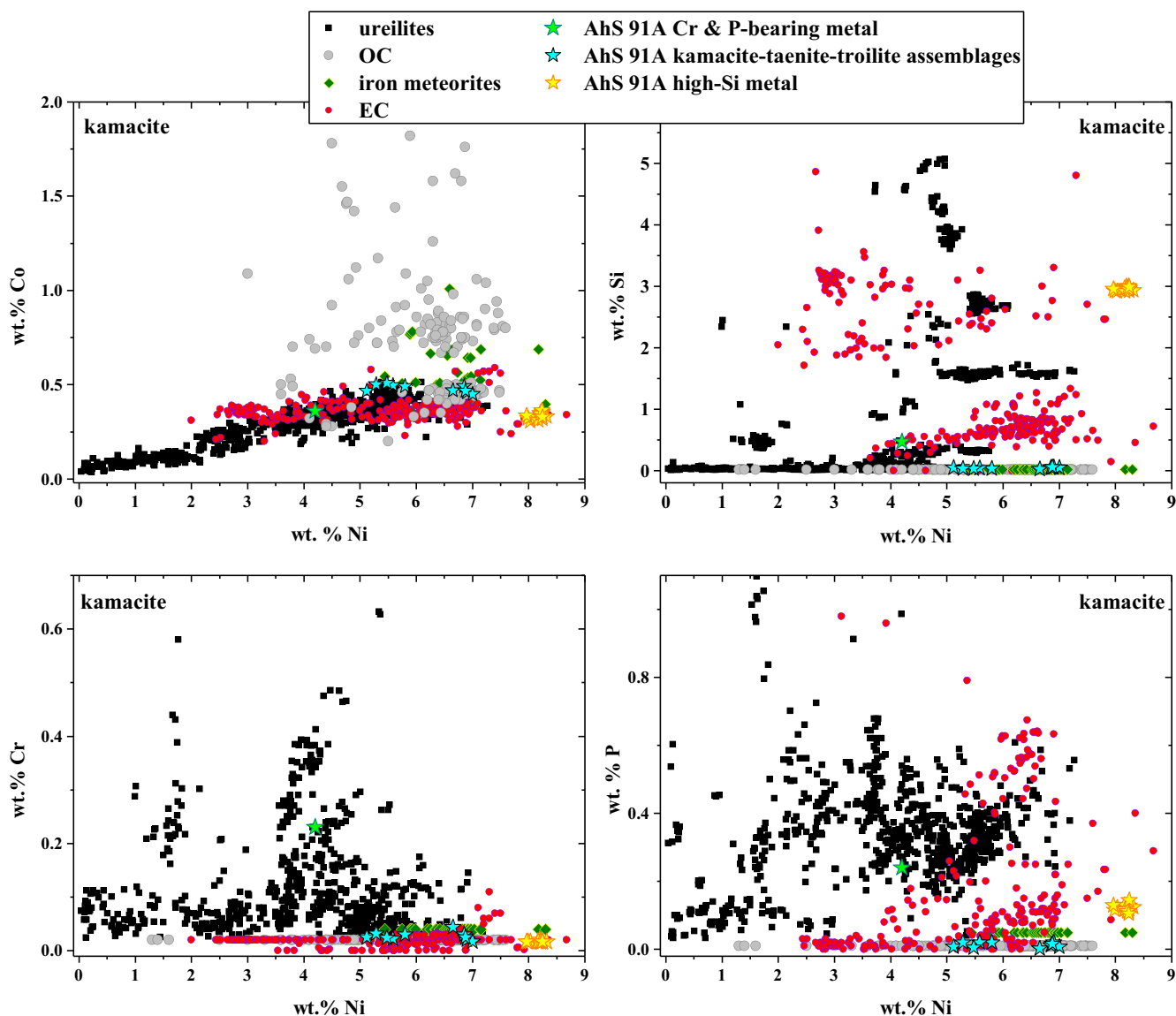


Fig. 17. Compositions of kamacite grains in AhS 91A and AhS 671 compared with compositions of metal in ureilites, ordinary chondrites (OC), enstatite chondrites (EC), and iron meteorites. Three different types of metal are distinguished by composition and associated minerals. Data for ureilites from Goodrich et al. (2013b); ordinary chondrites from Rubin (1990), Zanda et al. (1994), Afiatalab and Wasson (1980), Brearley and Jones (1998), Reisener and Goldstein (2003); enstatite chondrites from Weisberg and Kimura (2012); Horstmann et al. (2014); Brearley and Jones (1998); iron meteorites from Goldstein et al. (2017), Brearley and Jones (1998), Rout et al. (2017). (Color figure can be viewed at wileyonlinelibrary.com.)

relative to the other two fragments, but essentially similar Xe concentrations. This leads to high $^{36}\text{Ar}/^{132}\text{Xe}$ (~ 870) and $^{84}\text{Kr}/^{132}\text{Xe}$ (~ 2.2) ratios in AhS 91A_14, compared to these ratios in AhS 91A_12 and AhS 91A_15 (~ 90 , ~ 0.8 , respectively), which resemble Q gas compositions.

Density and Porosity

Results of the measurements of density and porosity for AhS 91A_18 and AhS 91A_19 are given in Table 14. The bulk densities of the two samples

(2.33 ± 0.06 and $2.39 \pm 0.01 \text{ g cm}^{-3}$, respectively) are within the range measured for 12 CM2 chondrites (1.88–2.54; median 2.20 g cm^{-3}) by Macke et al. (2011a), which are lower than those of any other CC except CI. In contrast, the grain density of the samples ($3.69 \pm 0.16 \text{ g cm}^{-3}$) is higher than those of CM2 ($2.74\text{--}3.26 \text{ g cm}^{-3}$), and similar to the highest grain densities measured for CV ($3.25\text{--}3.86 \text{ g cm}^{-3}$) or CO ($3.17\text{--}3.78 \text{ g cm}^{-3}$) chondrites (Macke et al. 2011a). The porosity of the two samples ($36.2 \pm 3.0\%$) is much higher than those of any CCs or other meteorite types

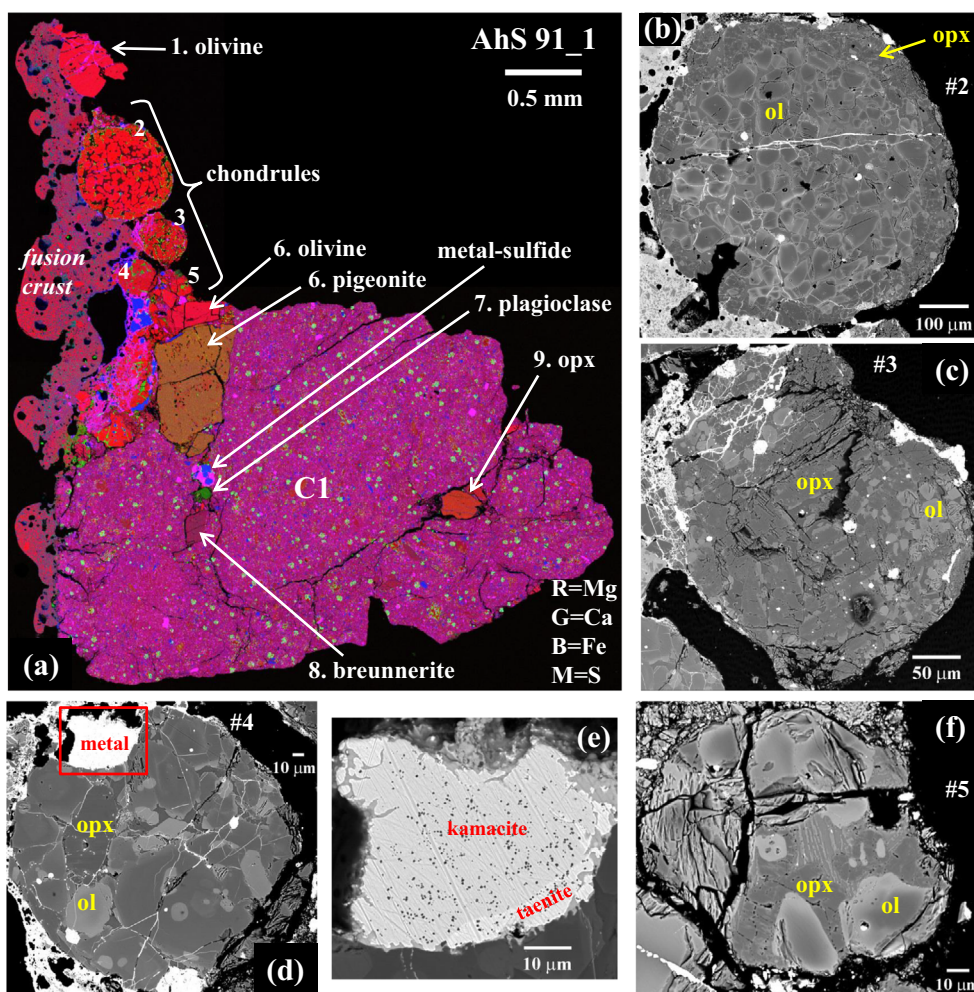


Fig. 18. a) Combined elemental X-ray map of polished section of AhS 91_1. Red = Mg, green = Ca, blue = Fe, magenta = S. Section shows dominantly C1 material, containing clasts of ureilitic minerals (olivine, pigeonite, plagioclase, orthopyroxene), a metal-sulfide globule (shown in Fig. 16a), and four chondrules. b) BEI of chondrule #2 from (a). Type IAB POP. c) BEI of chondrule #3 from (a). Type IAB. d) BEI of chondrule #4 from (a). Type IIAB POP. e) BEI of kamacite-metal grain in chondrule #4, area outlined by red box in (d). f) BEI of chondrule #5 from (a). Type IAB POP. opx = orthopyroxene; ol = olivine. (Color figure can be viewed at wileyonlinelibrary.com.)

except CI, the ungrouped CC Tagish Lake, or a few rare CM chondrites (Bland et al. 2004; Hildebrand et al. 2006; Macke et al. 2011a, 2011b).

DISCUSSION

What Type of Meteorites Are AhS 91A and AhS 671?

CC Lithology

The dominant component of AhS 91A and AhS 671 is a CC matrix-like material, which we have referred to as the C1 lithology because it appears to consist mainly, or entirely, of products of aqueous alteration (Zolensky and McSween 1988). The mineral assemblages, textures, and mineral compositions of this lithology resemble

those of CI1 meteorites, which consist almost entirely of diverse lithic fragments of aqueously altered matrix material (Brearley and Jones 1998; Bland et al. 2002). Like CI1s (Tomeoka and Buseck 1988), the CC lithology in AhS 91A and AhS 671 consists mostly of fine-grained Mg-rich serpentine and saponite, with abundant magnetite, sulfides, and carbonates. It is also similar in mineralogy and phyllosilicate Mg#s to CR1 matrix (Le Guillou et al. 2015), but differs from CR1 chondrites in not containing chondrules. It differs from CM matrices, in which cronstedtite is a major phase (Müller et al. 1977; Akai 1980; MacKinnon 1980, 1982; Barber 1981; Akai and Kanno 1986). The areas rich in fayalitic olivine in AhS 91A and AhS 671 CC bear some resemblance to CV matrices (Green et al. 1971; Kornacki and Wood 1984;

Table 6. Compositions of phases in chondrules in Ahs 91_01 from EMPA.

	Chondrule 2				Chondrule 3				Chondrule 4				Chondrule 5							
	xtal cores		xtal rim		xtal rim		xtal rim		xtal rim		xtal rim		xtal rim		xtal rim		xtal rim			
	oliv Avg. (24)	SD	oliv Avg. (8)	SD	oliv Avg. (8)	SD	oliv Avg. (8)	SD	oliv Avg. (8)	SD	oliv Avg. (10)	SD	oliv Avg. (10)	SD	oliv Avg. (28)	SD	oliv Avg. (10)	SD	oliv Avg. (3)	SD
SiO ₂	41.6	0.3	39.5	0.04	39.8	0.06	39.0	0.3	39.0	0.4	39.0	0.3	39.0	0.3	56.9	0.7	42.1	0.7	40.5	0.1
TiO ₂	bdl		bdl		bdl		bdl		0.10	0.02	bdl		bdl		0.04	0.02	bdl		bdl	0.24
Al ₂ O ₃	bdl		bdl		bdl		bdl		0.59	0.08	bdl		0.04	0.06	0.38	0.25	0.16		0.08	1.41
Cr ₂ O ₃	0.05	0.02	0.04	0.05	0.06	0.06	0.05	0.01	0.67	0.05	0.05	0.18	0.15	0.18	0.72	0.16	0.11		0.11	0.28
FeO	5.1	1.4	16.8	1.3	14.9	1.3	18.7	1.5	1.3	0.2	18.7	1.5	19.5	1.7	7.5	0.7	0.93		10.5	0.65
MgO	53.2	1.2	43.5	38.1	44.9	38.1	41.7	1.2	38.1	0.2	41.7	1.2	41.1	1.5	33.5	1.0	55.8		48.4	38.3
MnO	0.08	0.02	0.33	0.09	0.24	0.24	0.46	0.03	0.09	0.01	0.46	0.03	0.52	0.09	0.47	0.18	0.04		0.17	0.06
CaO	0.14	0.04	0.13	0.36	0.15	0.15	0.13	0.01	0.36	0.05	0.13	0.01	0.09	0.03	0.50	0.28	0.53		0.36	0.52
Na ₂ O	bdl		bdl		bdl		bdl		bdl		bdl		bdl		0.01	0.01	bdl		bdl	bdl
NiO	bdl		bdl		0.05	0.05	0.06	0.04	bdl		0.06	0.04	bdl		0.04	0.02	bdl		bdl	bdl
Total	100.2		100.3	99.9	100.1	100.1	100.1		99.9		100.1		100.4		100.0		99.7		100.1	99.9
Mg#	94.9	1.5	82.2	98.2	84.3	84.3	79.9	1.7	98.2	0.2	79.9	1.7	78.9	2.06	88.9	1.1	99.1		89.2	99.1
Wo				0.7	0.1	0.1			0.7	0.1					1.0	0.6			1.0	0.0

Numbers in parentheses are number of analyses in the average.

Mg# = 100 × molar MgO/(MgO + FeO); Wo = 100 × molar CaO/(CaO + FeO + MgO); An = 100 × molar CaO/(CaO + Na₂O + K₂O); Or = 100 × molar K₂O/(CaO + Na₂O + K₂O).

xtal = crystal; oliv = olivine; opx = orthopyroxene.

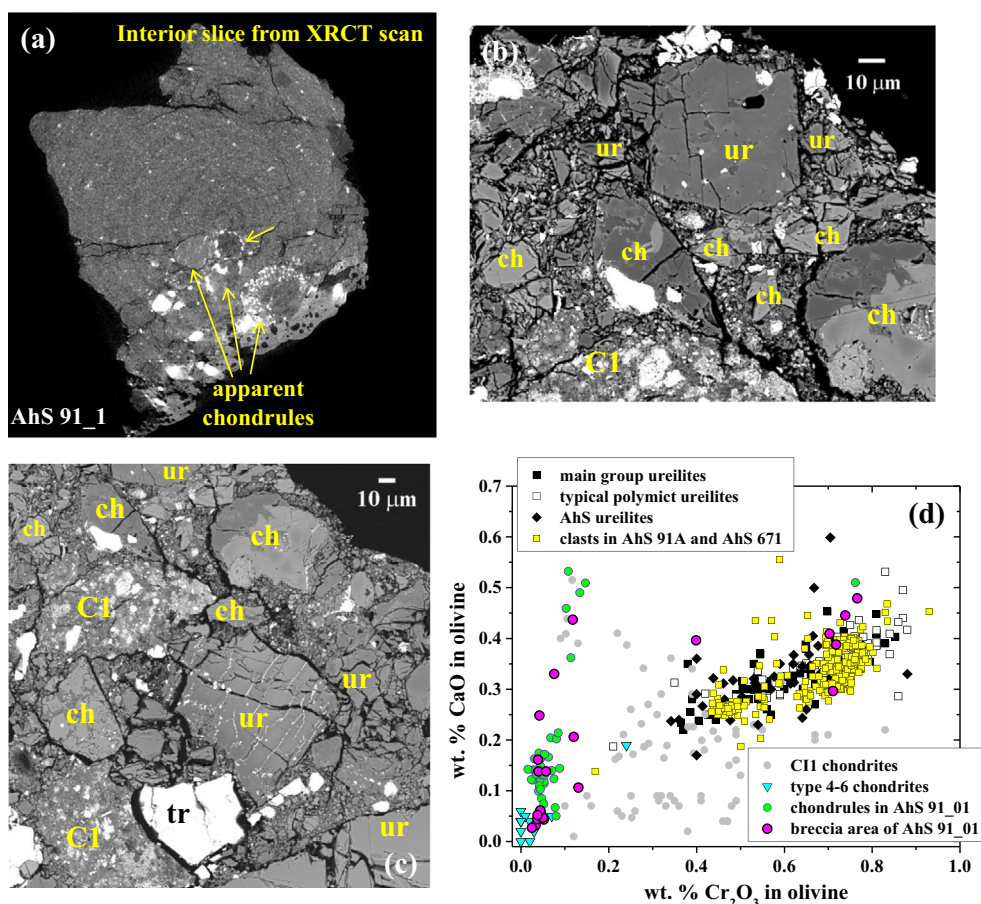


Fig. 19. a) Frame from XRCT scan of fragment AhS 91_1, showing several chondrules in the interior, not yet exposed in section. b, c) BEI of brecciated zone in AhS 91_01, exposed by polishing down the section shown in Fig. 18. Lithic and mineral fragments of mixed ureilitic (ur), CI, and chondrule-like (ch) materials. d) Plot of wt% Cr_2O_3 versus wt% CaO in olivine grains from the areas in (b, c), showing that some of these grains could be derived from chondrules similar to chondrules #2–5 (Fig. 18), whereas others are ureilitic. (Color figure can be viewed at wileyonlinelibrary.com.)

Table 7. Bulk oxygen isotope compositions for AhS 91A and AhS 671.

Sample		$\delta^{17}\text{O}'$	SE	$\delta^{18}\text{O}'$	SE	$\Delta^{17}\text{O}'$	SE	<i>n</i>
AhS 91A_08	CC-like	9.185	0.008	13.872	0.016	1.872	0.004	6
AhS 91A_08	CC-like	8.676	0.004	13.189	0.006	1.712	0.005	6
Average		8.931		13.531		1.792		
AhS 91A_08	Metallic?	-0.671	0.005	-1.263	0.007	-0.004	0.005	6
AhS 91A_08	Metallic?	-0.748	0.003	-1.399	0.006	-0.01	0.003	6
Average		-0.710		-1.331		-0.007		
AhS 671 01_A.1	CC-like	7.42	0.007	11.105	0.009	1.556	0.009	10
AhS 671 01_A.2	CC-like	7.195	0.003	10.639	0.012	1.577	0.007	7
Average		7.308		10.872		1.567		

SE = standard error.

Peck 1984; Keller et al. 1994; Krot et al. 1995), but the porous, tabular morphology of the olivine (Fig. 11) differs from that in most CVs (Krot et al. 1995); furthermore, other phases common in CV matrices (andradite, grossular, wollastonite, feldspathoids) are

absent. Compositions of magnetite in AhS 91A and AhS 671 are like those of magnetite in CI and CR and distinct from those in CV and CK (Fig. 10). Compositions of carbonates in AhS 91A and AhS 671 (breunnerite and lesser dolomite) are most consistent with those in CI

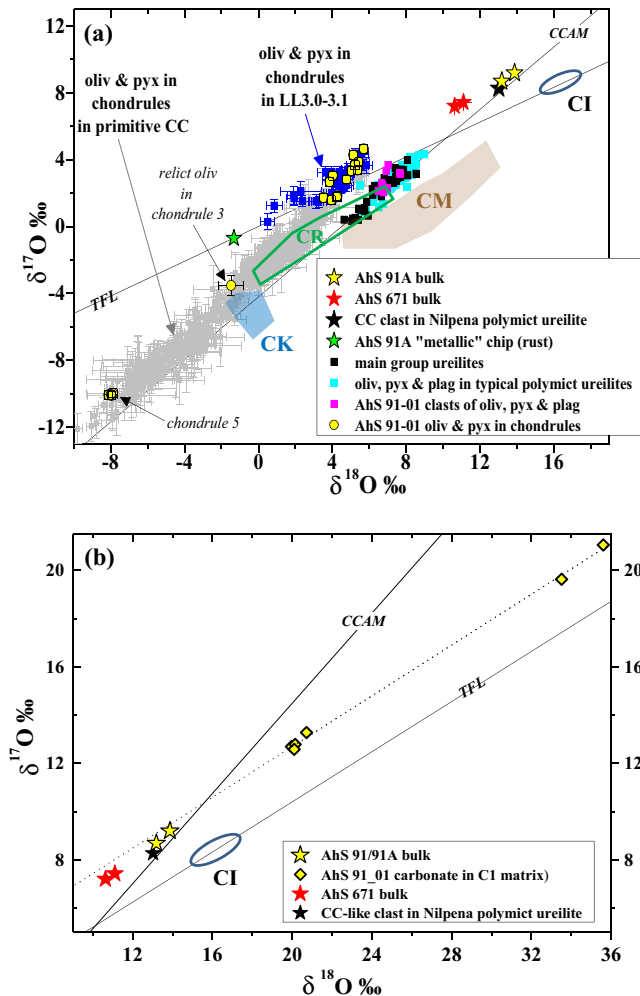


Fig. 20. a) Three oxygen isotope plot showing bulk compositions of fragments of AhS 91A and AhS 671 dominated by the CI lithology. These compositions do not match those of any known chondrite group, but are very similar to the composition of a CC-like clast from the Nilpena polymict ureilite (Brearley and Prinz 1992). A “metallic”-looking chip removed from the AhS 91A fragment has a composition on the terrestrial fractionation line (TFL), and was found to consist of iron oxides/hydroxides (rust). The bulk composition obtained for AhS 671 is consistent with being a mix of AhS 91A and terrestrial contamination similar to the “metallic” chip. Also shown are oxygen isotope compositions obtained by SIMS for various components of AhS 91_1 (Fig. 18). Clasts of olivine, pyroxene, and plagioclase in this section have oxygen isotope compositions consistent with those of main group ureilites and silicate clasts in typical polymict ureilites. Olivine and pyroxene in chondrules #2–4 (Fig. 18b–d) have oxygen isotope compositions consistent with those of olivine and pyroxene in chondrules in LL3.0–3.1 chondrites (Kita et al. 2010). One olivine grain in chondrule #3 is more ^{16}O -rich ($\Delta^{17}\text{O} = -2.8\text{‰}$) and may be a relict grain (remnant of chondrule precursors). Olivine and pyroxene in chondrule #5 have oxygen isotope composition out of the range of OC and consistent with olivine and pyroxene in primitive (type 3) CC (Ushikubo et al. 2012; Tenner et al. 2015). b) Three oxygen isotope plots showing compositions obtained by SIMS from the core and zoned rim of a carbonate (breunnerite) grain in AhS 91_0 (Fig. 18). These data show $\Delta^{17}\text{O}$ slightly higher than bulk AhS 91A, and form a mass-dependent fractionation line (slope = 0.526, correlation coefficient 0.999). Main group ureilite data from Clayton and Mayeda (1996); clasts in typical polymict ureilites from Downes et al. (2008) and Kita et al. (2004, 2006). (Color figure can be viewed at wileyonlinelibrary.com.)

(Fig. 9), although dolomite is more abundant than breunnerite in CIs (Johnson and Prinz 1993; Endress and Bischoff 1996). They differ from carbonates in CMs, in which calcite is more abundant than dolomite (Barber 1981; Johnson and Prinz 1993; Brearley 1995) and breunnerite has not been reported (Fig. 9).

However, although this lithology appears to be most like CI1, it also shows evidence of spatially heterogeneous thermal metamorphism that resulted in dehydration, including the nearly anhydrous Ca-rich silicate phase, the absence of OH^- bands in $\mu\text{-FTIR}$ spectra of some areas of AhS 91A, and the presence of significant amounts of fayalitic olivine. In particular, the unique morphology (not seen in known CC) of magnetite clusters rimmed by fayalitic olivine (e.g., Fig. 10c) may be a product of reduction of magnetite during metamorphism (Zolotov et al. 2006). Evidence for post aqueous alteration thermal metamorphism is seen in some CIs (Nakamura 2005; Tonui et al. 2014), and may have been common on primitive, volatile-rich bodies.

Furthermore, bulk oxygen isotope compositions of AhS 91A and AhS 671 show that it is distinct from CI and unlike any previously known chondrite (Fig. 20a). This result is underscored by Cr isotope compositions, which show that AhS 91A and AhS 671 have unique $\varepsilon^{54}\text{Cr}$ values, which are the highest of any known solar system materials (Sanborn et al. 2017; Yin et al. 2018).

The CI lithology in AhS 91A and AhS 671 may, however, be related to some CC-like clasts in meteoritic breccias. Carbonaceous chondrite-like clasts occur as xenoliths and microxenoliths in typical polymict ureilites, HED (howardite-eucrite-diogenite) breccias, ordinary chondrite regolith breccias, and Rumuruti-type chondrites, with their apparent abundance decreasing in this order (Bischoff et al. 2006; Greshake 2014; Patzek et al. 2018a). In HED and ordinary chondrites, most CC-like clasts are mineralogically similar to CM2 or CR2 chondrites, with CI-like clasts being much less common (Zolensky et al. 1996, 2018; Gounelle et al. 2003; Herrin et al. 2011; Briani et al. 2012; Patzek et al. 2018a). However, in polymict ureilites, all CC-like clasts have been reported to be CI-like. Such clasts were first identified by Prinz et al. (1987) as “black (opaque)”

Table 8. Oxygen isotope compositions of phases in AhS 91_01 analyzed by SIMS.*

	<i>N</i>	$\delta^{18}\text{O}$	$\delta^{18}\text{O}$ unc.	$\delta^{17}\text{O}$	$\delta^{17}\text{O}$ unc.	$\Delta^{17}\text{O}$	$\Delta^{17}\text{O}$ unc.
<i>Ureilitic</i>							
AhS 91_1 Area 1 (olivine)	4	6.73	0.38	2.18	0.25	-1.32	0.19
AhS 91_1 Area 6 (olivine)	2	7.68	0.36	3.18	0.28	-0.81	0.23
AhS 91_1 Area 6 (pigeonite)	2	6.97	0.36	3.50	0.41	-0.12	0.33
AhS 91_1 Area 7 (plagioclase)	1	7.02	0.39	3.16	0.34	-0.49	0.28
AhS 91_1 Area 9 (orthopyroxene)	2	6.71	0.36	2.53	0.28	-0.96	0.23
<i>Chondrules</i>							
AhS 91_1 Area 2 chondrule Ol	4	4.92	0.69	3.35	0.33	0.80	0.23
AhS 91_1 Area 2 chondrule pyx	1	3.86	0.39	2.67	0.34	0.66	0.28
Mean AhS 91_1 Area 2 chondrule	5	4.71	0.71	3.22	0.40	0.77	0.21
AhS 91_1 Area 3 chondrule Ol	1	-1.47	0.75	-3.53	0.66	-2.76	0.41
AhS 91_1 Area 3 chondrule pyx	3	5.42	0.46	4.26	0.50	1.44	0.43
AhS 91_1 Area 4 chondrule Ol	2	4.16	1.30	2.27	1.11	0.10	0.45
AhS 91_1 Area 4 chondrule pyx	3	4.16	0.39	1.73	0.26	-0.44	0.20
Mean AhS 91_1 Area 4 chondrule	5	4.16	0.53	1.94	0.49	-0.22	0.33
AhS 91_1 Area 5 chondrule Ol	2	-8.04	0.37	10.09	0.28	-5.91	0.23
AhS 91_1 Area 5 chondrule pyx	1	-7.89	0.39	-9.98	0.34	-5.88	0.28
Mean AhS 91_1 Area 5 chondrule	3	-7.99	0.35	10.06	0.26	-5.90	0.20
<i>Carbonate (breunnerite)</i>							
AhS 91_1 Area 8 carbonate core	3	20.07	0.36	12.68	0.26	2.24	0.22
AhS 91_1 Area 8 carbonate intermediate	1	20.71	0.23	13.27	0.25	2.50	0.27
AhS 91_1 Area 8 carbonate rim 1	1	35.61	0.23	21.05	0.25	2.53	0.27
AhS 91_1 Area 8 carbonate rim 2	1	33.51	0.23	19.62	0.25	2.20	0.27
Mean AhS 91_1 Area 8 carbonate	6					2.33	0.21

unc. = uncertainty.

*Analysis areas are marked in Fig. 18a.

materials similar to carbonaceous chondrite matrix in the three polymict ureilites known at the time (Nilpena, North Haig, EET 83309). Prinz et al. (1987) noted that these clasts were “soft and friable” and consisted mostly of very fine-grained silicates with magnetite, Fe,Ni sulfides, Fe-Mn-Mg carbonates, and minor ilmenite and apatite. Brearley and Prinz (1992) conducted XRD, TEM, and analytical electron microscopy on one such clast and found that it consisted of very fine-grained phyllosilicates, with coarser sulfide and magnetite grains. The phyllosilicates were dominated by serpentine, with lesser amounts of saponite, minor chlorite, and other fine-grained and/or amorphous materials. They also identified a darker clast within the main clast, indicating that the clast itself was a breccia. Brearley and Prinz (1992) showed that the CC-like clasts in Nilpena were mineralogically more like CI than CM. However, one dark clast from Nilpena was analyzed for bulk oxygen isotopes (Clayton and Mayeda 1988) and found to be distinct from CI, as well as all other known chondrites (Fig. 20a). Patzek et al. (2018b) recently reported three CC-like clasts in other typical polymict ureilites with similar oxygen isotope compositions. Brearley and Prinz (1992) concluded that

the CC-like clasts in polymict ureilites were unique. This is supported by data for D/H ratios and S isotope ratios of a few CI-like clasts in typical polymict ureilites (Patzek et al. 2017; Visser et al. 2018).

The CI material in AhS 91A and AhS 671 is generally similar in mineralogy to the dark clasts in typical polymict ureilites described by Prinz et al. (1987) and Brearley and Prinz (1992). Furthermore, it is almost identical in oxygen isotope composition (Fig. 20a) to the dark clast from Nilpena analyzed by Clayton and Mayeda (1988) and the three clasts reported by Patzek et al. (2018b). However, studies of >130 CC-like xenoliths in 14 different polymict ureilites show substantial diversity in the abundances and compositions of their constituents (Ikeda et al. 2000, 2003; Goodrich et al. 2004; Kita et al. 2017; Patzek et al. 2018a) and, so far, only one clast that could be considered petrologically “identical” to AhS 91A or AhS 671 has been reported (Goodrich et al. 2019a). Furthermore, bulk oxygen isotopes have been analyzed for another CC-like clast from a polymict ureilite, and found to have a composition very different from that of 91A and 671 (Goodrich et al. 2019a). Continued petrologic and isotopic studies of CC-like clasts in

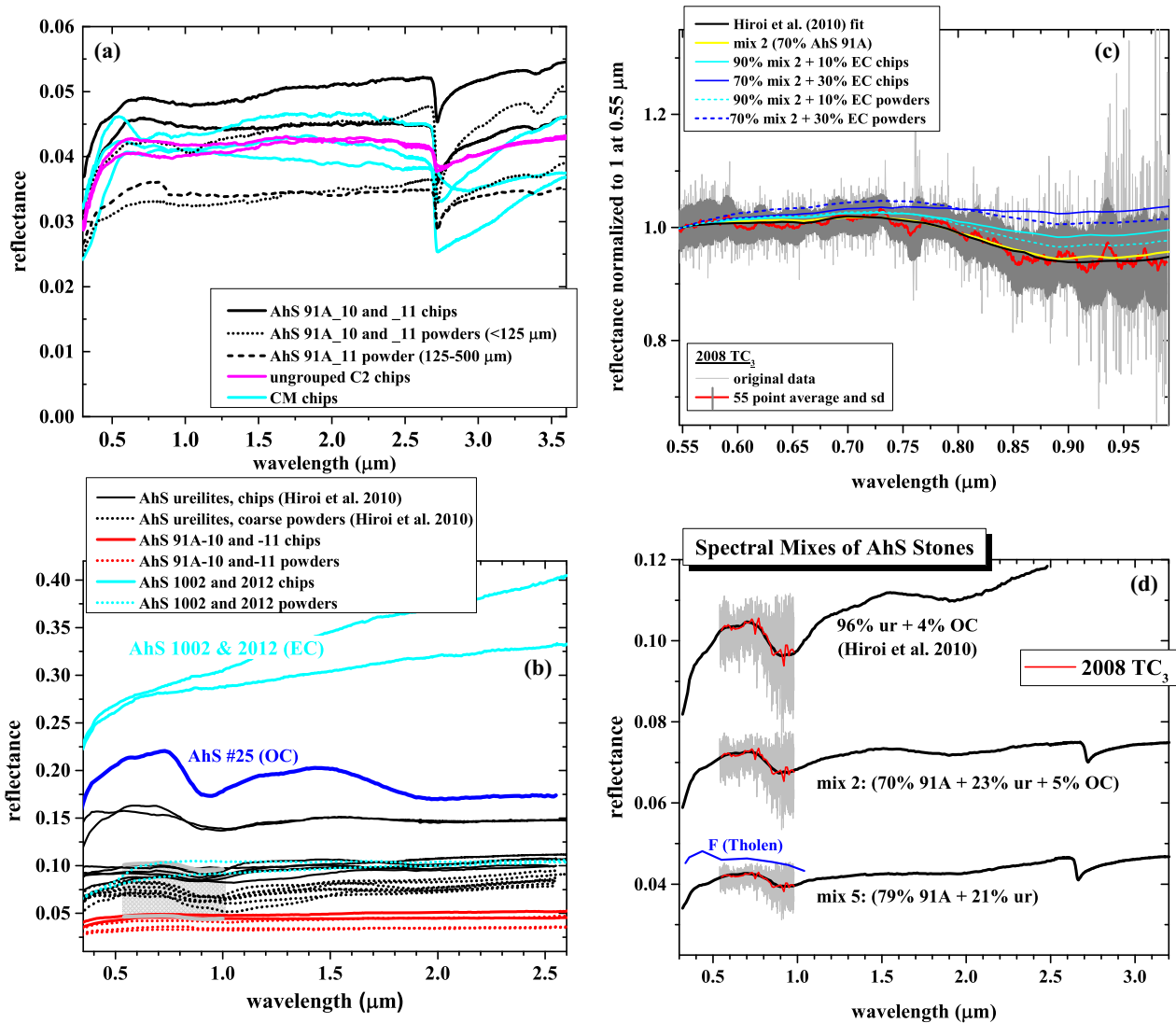


Fig. 21. a) Bulk sample reflectance spectra from 0.3 to 3.6 μm for chips and powdered samples of AhS 91A and AhS 671. Data for CM and ungrouped C2 chondrites (Hiroi et al. 2017) for comparison. b) VNIR reflectance spectra. Asteroid 2008 TC₃ was measured in the 0.55–1 μm range (Jenniskens et al. 2009) and is shown in light gray at the range of albedo estimates of Jenniskens et al. (2009) and Hiroi et al. (2010). Spectra for chips and coarse (125–500 μm) powders of AhS ureilites and ordinary chondrite from Hiroi et al. (2010). Spectra for chips (solid cyan lines) and powders (dashed cyan lines) of AhS 1002 and AhS 2012 enstatite chondrites and AhS 91A from this work. c) Spectrum of asteroid 2008 TC₃ (original data in light gray; 55 pt averaged spectrum in red with standard deviations [SD] in dark gray), normalized to 1 at 0.55 μm , compared with model spectra for mixtures of AhS stones from Hiroi et al. (2010) and calculated in this work. d) Model spectra (black) for mixtures of AhS ureilites + AhS 91A + OC calculated in this work and by Hiroi et al. (2010) compared with asteroid 2008 TC₃ (original data in light gray; 55 pt averaged spectrum in red) scaled to match the 0.55 μm reflectance of the mixtures in each case. Also shown in blue is the average spectrum of F-type asteroids (Tholen 1984) normalized to the average F-type albedo of 0.046 (Mainzer et al. 2011) at 0.55 μm . (Color figure can be viewed at wileyonlinelibrary.com.)

typical polymict ureilites and other meteoritic breccias are needed to determine whether AhS 91A and 671 are closely related to any of them.

Clasts and Chondrules

The clasts of olivine, pyroxene, plagioclase, graphite, and metal in AhS 91A and AhS 671 cannot be

indigenous to the CC lithology. Although the matrices of C1 and C2 chondrites sometimes contain a small fraction (estimated <1 vol% in C1 by Brearley and Jones 1998) of relict olivine and orthopyroxene grains (Steele 1990; Leshin et al. 1997; Frank et al. 2014), the olivine and pyroxene clasts in AhS 91A and 671 are much larger than such grains (up to 3 mm versus

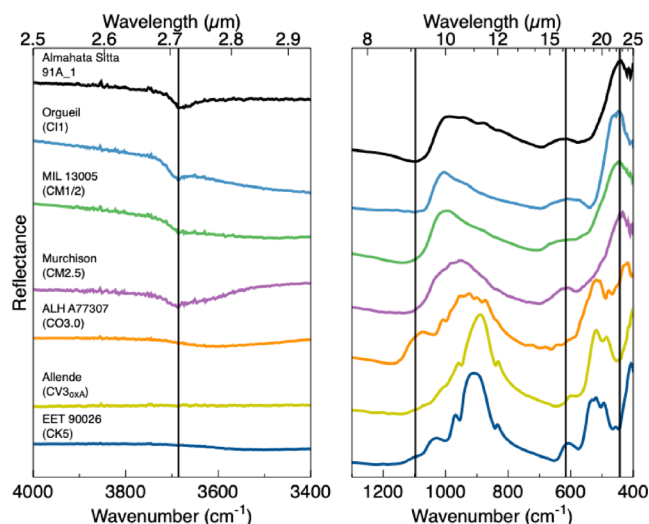


Fig. 22. Whole-rock reflectance spectrum of fragment AhS 91A_1 from μ -FTIR compared to similarly acquired spectra of carbonaceous chondrites (Hamilton 2018; Hamilton et al. 2018). Spectra are normalized and offset for comparison. Vertical lines denote features described in text. (Color figure can be viewed at wileyonlinelibrary.com.)

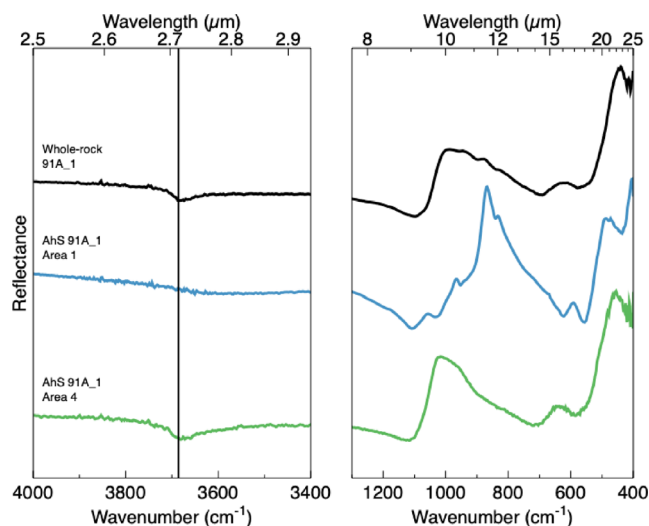


Fig. 23. Whole-rock reflectance spectrum of Almahata Sitta fragment 91A_1 from μ -FTIR compared to spectra isolated from areas 1 and 4 (Fig. 3a). Spectra are normalized and offset for comparison. Vertical line denotes position of OH^- feature described in text. (Color figure can be viewed at wileyonlinelibrary.com.)

400 μm). They also show sharp boundaries with the matrix, whereas relict grains in C1 and C2 have more diffuse edges (Steele 1990). Moreover, the olivine and pyroxene grains in AhS 91A and AhS 671 are compositionally distinct from those in C1/C2 (Figs. 14 and 15). Plagioclase has not been reported in CC matrices. Although CC can have carbon contents up to ~ 8 wt% (Kerridge 1985; Pearson et al. 2006), the

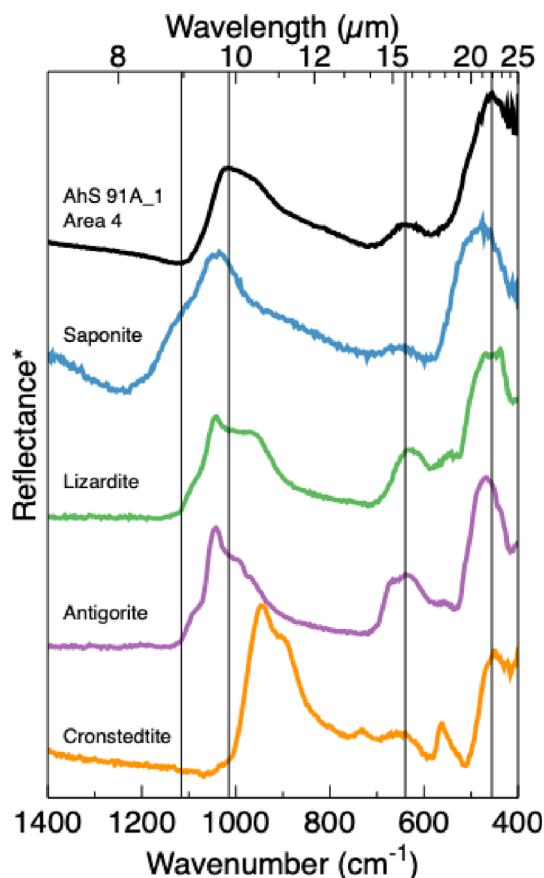


Fig. 24. Comparison of AhS 91A_1 area 4 reflectance and phyllosilicate mineral spectra measured in emission. Spectra are normalized and offset for comparison. Vertical lines denote positions of key features in the AhS area 4 spectrum at 1116, 1015, 640, and 456 cm^{-1} . (Color figure can be viewed at wileyonlinelibrary.com.)

carbon does not occur as large masses of graphite like those in AhS 91A and AhS 671 (Fig. 13d), but rather as widely dispersed organic compounds or poorly graphitized carbon (Hayes 1967; Smith and Buseck 1981; Botta and Bada 2002; Alexander et al. 2017). The metal grains in AhS 91A and AhS 671 (Fig. 16) are also unlikely to belong to the CC lithology, because Fe,Ni metal is absent or extremely rare in all CC matrix materials except reduced CVs (which do not contain magnetite and so are not analogous to AhS 91A and AhS 671).

A similar argument can be made for the chondrules in AhS 91_01 (Fig. 18). Although CC with aqueously altered matrices (C1 and C2) can contain chondrules (e.g., McSween 1979), such chondrules show various degrees of aqueous alteration (Ikeda 1983; Kojima et al. 1984; Browning et al. 1996). The chondrules in AhS 91_01 show no aqueous alteration, and therefore are not likely to be an indigenous component of the C1 material.

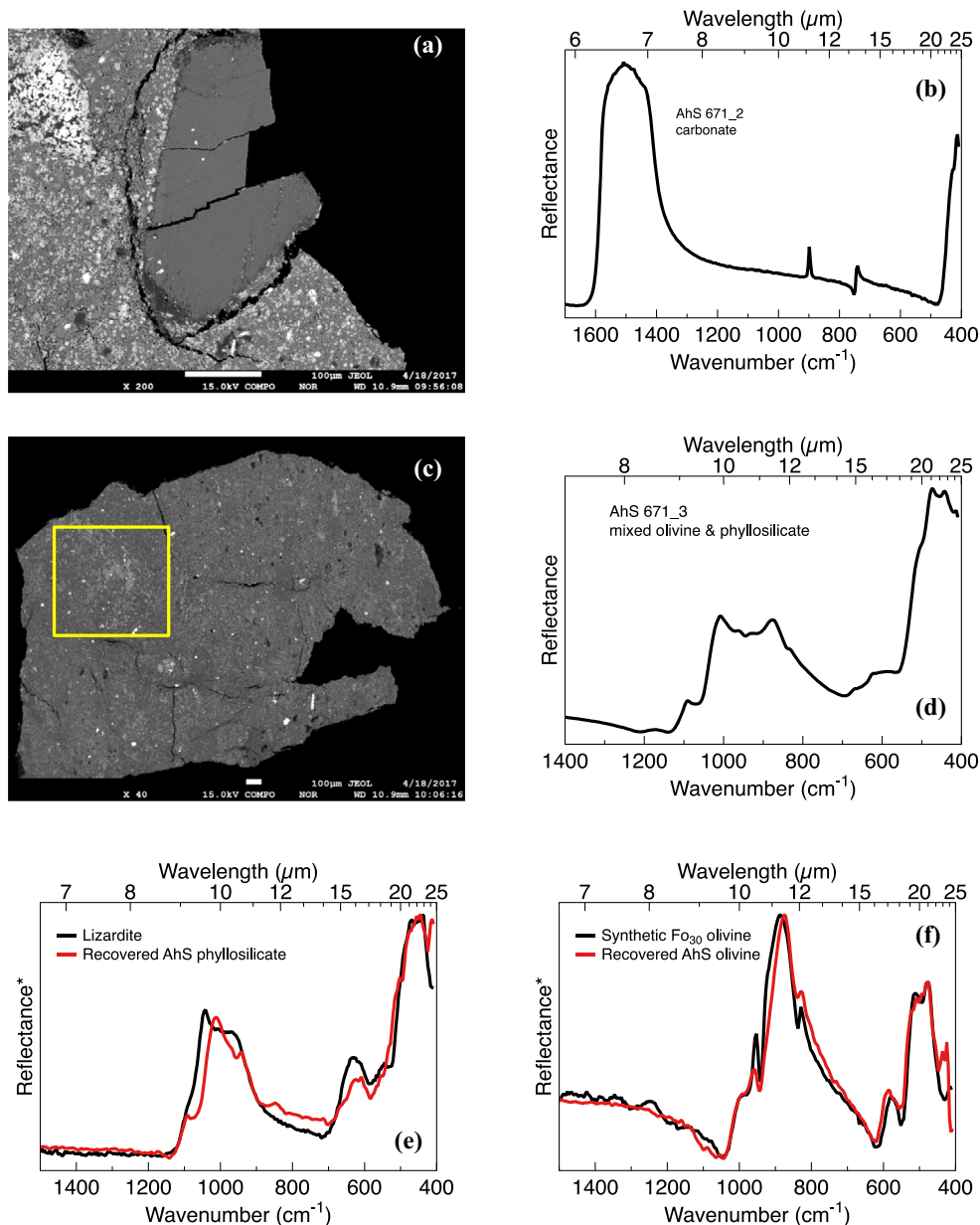


Fig. 25. a) Backscattered electron image of carbonate grain in fragment AhS 671_2. b) μ -FTIR reflectance spectrum of carbonate grain in (a). c) Backscattered electron image of fragment AhS 671_3 showing the outline of the area of the oversampled μ -FTIR map in yellow. d) Average μ -FTIR spectrum of the area outlined in (c) exhibiting features of both phyllosilicate and olivine. e) Laboratory emission spectrum of lizardite (inverted for comparison to reflectance) and the phyllosilicate spectrum recovered from AhS 671_3 by factor analysis. Features are not perfectly matched due to compositional differences between terrestrial and meteoritic serpentines. f) Laboratory emission spectrum of synthetic olivine (Fo₃₀) from Lane et al. (2011) and the olivine spectrum recovered from AhS 671_3 by factor analysis. (Color figure can be viewed at wileyonlinelibrary.com.)

If the olivine, pyroxene, plagioclase, graphite, metal, and chondrules in AhS 91A and AhS 671 are not part of the C1 lithology, then they must be xenolithic. What is their provenance? The olivine and pyroxene clasts can be identified as ureilitic from their compositions and internal textural features. Olivines in main group ureilites, typical polymict ureilites, and ureilitic stones

from AhS show characteristic compositions, with Fo ranging from ~75 to 95 (among samples), a well-defined Fe/Mg-Fe/Mn trend of near-constant Mn/Mg ratio that passes through the origin, and high CaO and Cr₂O₃ contents (Fig. 14). These combined features distinguish ureilitic olivine from that in all other major meteorite groups (Fig. 14). The compositions of the olivine clasts

Table 9. Helium and Ne concentrations (in $10^{-8} \text{ cm}^3 \text{ g}^{-1}$) and isotopic ratios in three fragments of AhS 91A.

#	Mass (mg)	^4He	$^3\text{He}/^4\text{He} \times 10,000$	^{20}Ne	$^{20}\text{Ne}/^{22}\text{Ne}$	$^{21}\text{Ne}/^{22}\text{Ne}$	$^{21}\text{Ne}_{\text{cos}}$
12	14.94 ± 0.01	6505 ± 50	11.42 ± 0.10	21.62 ± 0.15	4.25 ± 0.03	0.518 ± 0.003	2.579 ± 0.019
14	7.79 ± 0.01	8699 ± 88	6.19 ± 0.07	54.7 ± 0.4	7.96 ± 0.05	0.2258 ± 0.0013	1.394 ± 0.016
15	6.88 ± 0.01	5922 ± 48	9.01 ± 0.08	21.83 ± 0.20	5.08 ± 0.05	0.454 ± 0.003	1.887 ± 0.017

Table 10. Argon concentrations (in $10^{-8} \text{ cm}^3 \text{ g}^{-1}$) and isotopic ratios in three fragments of AhS 91A.

#	^{36}Ar	$^{36}\text{Ar}/^{38}\text{Ar}$	$^{40}\text{Ar}/^{36}\text{Ar}$	$^{38}\text{Ar}_{\text{cos}}$	$^{40}\text{Ar}_{\text{rad}}$
12	83.3 ± 1.0	5.204 ± 0.023	27.6 ± 0.4	0.45 ± 0.09	2300 ± 43
14	1064 ± 18	5.302 ± 0.022	1.59 ± 0.03	1.4 ± 1.1	1692 ± 46
15	114.5 ± 1.9	5.310 ± 0.022	14.5 ± 0.3	n.d.	1660 ± 46

Table 11. Krypton concentrations and isotopic ratios in three fragments of AhS 91A.

#	^{84}Kr $10^{-10} \text{ cm}^3/\text{g}$	$^{78}\text{Kr}/^{84}\text{Kr}$	$^{80}\text{Kr}/^{84}\text{Kr}$	$^{82}\text{Kr}/^{84}\text{Kr}$	$^{83}\text{Kr}/^{84}\text{Kr}$	$^{86}\text{Kr}/^{84}\text{Kr}$
		$^{84}\text{Kr} = 100$				
12	88.0 ± 0.7	0.608 ± 0.005	3.994 ± 0.026	20.22 ± 0.11	20.08 ± 0.18	31.23 ± 0.17
14	272.3 ± 2.3	0.599 ± 0.005	3.873 ± 0.027	19.97 ± 0.12	19.90 ± 0.09	30.33 ± 0.15
15	99.6 ± 0.9	0.593 ± 0.006	4.04 ± 0.03	20.12 ± 0.14	20.05 ± 0.18	30.73 ± 0.22

Table 12. Xenon concentrations and isotopic ratios in three fragments of AhS 91A.

#	^{132}Xe $10^{-10} \text{ cm}^3/\text{g}$	$^{124}\text{Xe}/^{132}\text{Xe}$	$^{126}\text{Xe}/^{132}\text{Xe}$	$^{128}\text{Xe}/^{132}\text{Xe}$	$^{129}\text{Xe}/^{132}\text{Xe}$	$^{130}\text{Xe}/^{132}\text{Xe}$
		$^{132}\text{Xe} = 100$				
12	108.8 ± 2.6	0.466 ± 0.004	0.412 ± 0.004	8.14 ± 0.06	105.1 ± 1.0	16.08 ± 0.10
14	22.5 ± 2.9	0.439 ± 0.005	0.389 ± 0.006	7.97 ± 0.06	103.4 ± 0.6	15.86 ± 0.10
15	113.5 ± 2.8	0.453 ± 0.008	0.421 ± 0.009	8.16 ± 0.08	106.7 ± 1.2	16.24 ± 0.15
(Continued)		$^{131}\text{Xe}/^{132}\text{Xe}$	$^{134}\text{Xe}/^{132}\text{Xe}$		$^{136}\text{Xe}/^{132}\text{Xe}$	
#			$^{132}\text{Xe} = 100$			
12		81.9 ± 0.5	38.51 ± 0.29		32.40 ± 0.22	
14		81.0 ± 0.4	38.11 ± 0.22		31.81 ± 0.17	
15		82.6 ± 0.8	38.5 ± 0.4		32.4 ± 0.3	

in AhS 91A and AhS 671 are consistent with these characteristics and encompass most of the known ureilitic range. At least six distinct main group ureilite lithologies are represented by these clasts. Internal textures further support ureilitic provenance. The reduced zones along grain boundaries and around inclusions of graphite are a characteristic feature of ureilitic olivine, as are the graphite inclusions themselves (Wlotzka 1972; Mittlefehldt et al. 1998). The micron-sized chromite+pyroxene symplectites in the Fo ~78–79 clasts (Fig. 12e) are also a feature of ureilitic olivines of Fo 75–79 (Goodrich et al. 2013a).

Pyroxenes in ureilites also show characteristic compositional features. The sole or dominant pyroxene in ~95% of main group ureilites is pigeonite with Wo ~6–14. Most meteoritic pigeonites are significantly more

ferroan than the pigeonite in ureilites (Fig. 15a). Ureilites (main group ureilites, clasts in typical polymict ureilites, and ureilitic stones from AhS) represent a unique occurrence of Mg-rich (Mg# ~78–92) pigeonite, which also has higher Cr₂O₃ contents than low-Ca pyroxenes in most other meteorites (Fig. 15b). The pigeonite clasts in AhS 91A and AhS 671 have Wo, Mg#, and Al₂O₃ and Cr₂O₃ contents consistent with ureilitic pigeonite (Fig. 15). The primary orthopyroxenes (i.e., ignoring shock-recrystallized pyroxenes) in ureilites also have distinct compositions. They occur mostly in the more magnesian ureilites, with Mg# >~87, and invariably have Wo ~4.5–4.9 (Mittlefehldt et al. 1998; Goodrich et al. 2004). Two of the three orthopyroxene clasts in AhS 91A and AhS 671 have Wo, Mg#, and Al₂O₃ and Cr₂O₃ contents consistent with those of

ureilitic orthopyroxene. The porous, reduced patches in some of the pigeonite clasts (Fig. 13c) further support their ureilitic provenance. Internal textures like these occur in pigeonites in some main group ureilites and many AhS ureilites and have been attributed to pyroxene-selective impact smelting (Bischoff et al. 2010; Zolensky et al. 2010; Warren and Rubin 2011). From the number of distinct pigeonite compositions, at least five main group ureilites are represented by these clasts. The Wo 4.5 orthopyroxene clast could be derived from the most magnesian of these, based on compositions of coexisting pigeonite and orthopyroxene in main group ureilites. Based on typical compositions of coexisting olivine and pigeonite in main group ureilites (Mittlefehldt et al. 1998; Goodrich et al. 2004), these could be the same five ureilitic lithologies that are represented by the olivine clasts in AhS 91A and AhS 671. The orthopyroxene clast of Wo 0.8, Mg# 99.5 (Table 4, column 15) has major and minor element compositions out of the range of ureilites and consistent with those of orthopyroxenes in several types of chondrites (Fig. 15).

The plagioclase clasts in AhS 91A and 671 could also be derived from ureilites. Main group ureilites do not contain plagioclase (Mittlefehldt et al. 1998), but typical polymict ureilites contain a few vol% of plagioclase as mineral and lithic clasts (Jaques and Fitzgerald 1982; Prinz et al. 1987, 1988; Ikeda et al. 2000; Cohen et al. 2004; Goodrich et al. 2004, 2017a; Kita et al. 2004, 2006; Goodrich and Wilson 2014). These clasts span the entire range from albite to anorthite, with two main populations, one “albitic” (An ~0–30) and the other “labradoritic” (An ~33–70) (Ikeda et al. 2000; Cohen et al. 2004; Goodrich et al. 2017a). These two populations probably represent indigenous melt lithologies complementary to main group ureilites (Cohen et al. 2004; Goodrich et al. 2004; Kita et al. 2004). One AhS stone, called ALM-A (Bischoff et al. 2015b), is a trachyandesite with mineral and oxygen isotope compositions resembling those of the “albitic” lithology in typical polymict ureilites. Two of the three plagioclase clasts in AhS 91A and AhS 671 have major and minor (Mg, Fe) element compositions (Table 4) consistent with the “albitic” lithology and ALM-A, and the third has major and minor element compositions consistent with the “labradoritic” lithology.

Oxygen isotope compositions of the olivine, pyroxenes, and plagioclase clasts in AhS 91_01 (Fig. 18a) are within the range of compositions of main group ureilites and clasts in polymict ureilites (Fig. 20a), and thus support the ureilitic provenance of these clasts.

The provenance of the graphite masses in the C1 material cannot be determined from any in situ analyses

we were able to make on the carbon. However, some of them have inclusions of metal (Fig. 13d) of characteristically ureilitic composition (see next paragraph). Furthermore, the fact that they are found with numerous other clasts derived from ureilites (which contain abundant graphite) strongly suggests ureilitic provenance. The presence of minor diamond in some of the graphite masses (Supplement 3) further supports this interpretation (Mittlefehldt et al. 1998; Ross et al. 2011).

Based on composition, the metal grains in AhS 91A and AhS 671 are derived from three different meteorite types—ureilites, ordinary chondrites, and enstatite chondrites. Ureilitic metal is kamacite with ~1–7 wt% Ni (Goodrich et al. 2013b). It is distinguished from kamacite in ordinary chondrites and iron meteorites by its significant Si, P, and Cr contents, and from kamacite in enstatite chondrites by higher Cr (Fig. 17). Thus, kamacite grains that occur in AhS 91A and 671 without taenite, and contain significant Si, P, and Cr (e.g., Table 5, column 1), are likely of ureilitic provenance. The association of Cr-bearing troilite with some of these grains further supports this interpretation, as Cr-bearing troilite is common in ureilites (Goodrich et al. 2013b). The kamacite-taenite-troilite assemblages in AhS 91A and AhS 671 (e.g., Fig. 16a) are likely derived from ordinary chondrites, considering the low abundances of Cr, P, and Si in their kamacite (consistent with either OC or iron meteorites; Fig. 17) in combination with their textures (similar to those of kamacite-taenite-troilite particles in OC rather than the typical Widmanstätten texture of iron meteorites: Brearley and Jones 1998). Cobalt contents of the kamacite further narrow it down to the H group (Kallemeyn et al. 1989). The grains of Si-rich kamacite in AhS 91A and 671 (e.g., Figs. 16b–d) have compositions that constrain them to being from enstatite chondrites (Fig. 17). Nickel and Si contents of these grains further narrow it down to EH type 4–6 (Weisberg and Kimura 2012). Enstatite chondrite provenance is also supported by inclusions of enstatite and niningerite in these grains (Figs. 16b–d; Ehlers and El Goresy 1988; El Goresy et al. 1988; Weisberg and Kimura 2012; Horstmann et al. 2014).

Based on textures, mineralogy, and mineral compositions, the chondrules and chondrule fragments in AhS 91_01 are most likely derived from type 3 OC, RC, or CC (Bischoff 2000; Scott and Krot 2004; Jones 2012). Oxygen isotope compositions (Fig. 20a) of chondrules #2, #3, and #4 (Figs. 18b–d) are most consistent with OC. The combined Fo of olivine and Co content of kamacite in chondrule #4 suggest H type (Kallemeyn et al. 1989). The ¹⁶O-rich composition of chondrule #5 (Fig. 20a) suggests derivation from type 3 CC.

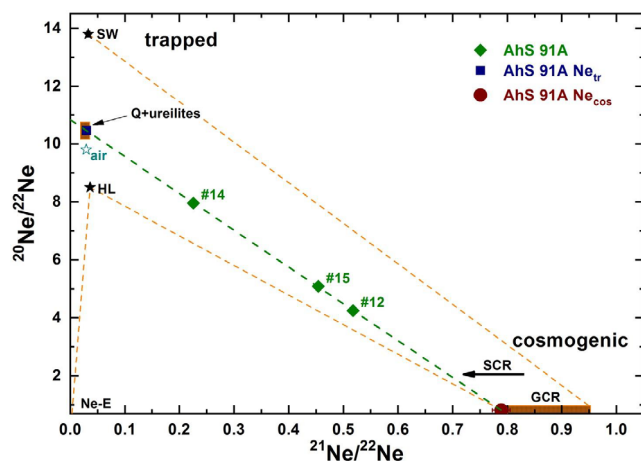


Fig. 26. Neon three-isotope plot showing the data points for AhS 91A_12, AhS 91A_14, and AhS 91A_15. They appear to plot on a mixing line between a trapped component (upper left) and a cosmogenic Ne endmember composition (lower right). The spread along the line suggests varying mixing ratios of these two endmembers, with AhS 91A_14 containing by far more trapped Ne relative to cosmogenic Ne than the other two samples. This is consistent with the huge trapped ^{36}Ar concentration detected in AhS 91A_14 relative to AhS 91A_12 and AhS 91A_15 (see text). Extrapolation of this line to a typical trapped $^{21}\text{Ne}/^{22}\text{Ne}$ (0.0294) yields a $^{20}\text{Ne}/^{22}\text{Ne}$ ratio of 10.45 ± 0.05 , similar to Ne observed in phase Q and ureilites. The remarkably constant trapped $^{20}\text{Ne}/^{22}\text{Ne}$ ratio observed for all three samples suggests that the additional trapped component in AhS 91A_14 is not SW, which would shift the data point toward higher $^{20}\text{Ne}/^{22}\text{Ne}$. References: HL (noble gas component residing in presolar diamonds)—Huss and Lewis (1995); Q—Busemann et al. (2000); “ureilites”—Göbel et al. (1978) and Ott et al. (1985); SW (solar wind as measured by Genesis)—Heber et al. (2009); GCR (typical range for cosmogenic Ne)—Wieler (2002). (Color figure can be viewed at wileyonlinelibrary.com.)

Summary and Implications

Summarizing the petrology and oxygen isotope compositions of AhS 91A and AhS 671, these stones are breccias of a type not previously known among meteorites. They are dominated by aqueously altered (C1) matrix material that has similarities to CII but also has unique mineralogic features and oxygen and Cr isotope compositions, showing that it represents a reservoir of volatile-rich early solar system material not so far sampled by whole meteorites. The C1 matrix material encloses clasts of ureilitic olivine, pyroxene, plagioclase, graphite, and metal representing at least six different ureilite lithologies, EC metal-sulfide and enstatite grains, OC metal-sulfide grains, and chondrules derived from type 3 OC and CC.

Although most of the material in AhS 91A is mineralogically similar to CI chondrites, both the bulk density and the grain density of two 91A fragments (Table 14) are higher than those of CI (Macke et al.

Table 13. Model production rates P_x (Leya and Masarik 2009) for ^3He and ^{21}Ne assuming chemistry to be (1) ureilitic (Welten et al. 2010) and (2) CI chondritic (Lodders and Fegley 1998) and calculated as an average over the expected shielding depths in 2008 TC₃. Two production rate and CRE age (T_x) sets are given.

	Ureilitic		CI chondritic		
	P_3	P_{21}	P_3	P_{21}	
	1.62	0.394	1.52	0.220	
	T_3	T_{21}	T_3	T_{21}	$T_{21,av}$
12	4.6	6.6	4.9	12.0	9.3
14	3.3	3.5	3.5	6.5	5.0
15	3.3	4.8	3.5	8.7	6.8

Production rates P_x in $10^{-8} \text{ cm}^3/(\text{g} \times \text{Ma})$. Exposure ages T_x in Ma.

2011a). Two factors could account for this. First, the AhS 91A samples measured could contain ureilitic and OC type mineral clasts (no CT scans were obtained on these fragments), which would increase density relative to the phyllosilicate-dominated matrix. Second, the C1 material in AhS 91A and 671 shows indications of partial dehydration, which would also increase density. The porosity of AhS 91A (36%) is very similar to that of CI and similar ungrouped CC such as Tagish Lake (Macke et al. 2011a). The combination of density and porosity in AhS 91A does not match any known CC, which supports the interpretation that these stones are a previously unknown type of material.

AhS 91A and AhS 671 are the first AhS stones to contain both ureilitic and chondritic lithologies. They contain most of the previously known AhS stone types (multiple types of ureilites, EC, and OC), as well as a type of chondritic material not previously reported in AhS (C1). This suggests that AhS 91A and AhS 671 do not just give us another meteorite type to add to the inventory of AhS stones. Rather, these stones may be giving us direct information about the structure and composition of AhS (i.e., asteroid 2008 TC₃) overall.

Implications for the Structure and Composition of Asteroid 2008 TC₃

Two observations suggest that AhS 91A and AhS 671 could represent a substantial fraction of the pre-atmospheric mass of 2008 TC₃. First, the extreme friability of these samples suggests that materials like these could easily have disintegrated into \leq tens of micron-sized fragments when 2008 TC₃ impacted the atmosphere and became unrecoverable as macroscopic meteorites. Thus, they are plausible candidates for the missing $>99\%$ of the mass of the asteroid (Jenniskens et al. 2009; Shaddad et al. 2010). Second, the clasts in AhS 91A and 671 are derived from the

Table 14. Physical properties of AhS 91A_18 and AhS 91A_19.

	AhS 91A_18	AhS 91A_19	AhS 91A_(18+19)
Mass	130 ± 2 mg	65.5 ± 2 mg (calculated)	195.5 ± 2 mg
Bulk volume	0.0558 ± 0.0012 cm ³	0.0274 ± 0.0007 cm ³	0.0832 ± 0.0014 cm ³ (calculated)
Bulk density = mass/bulk volume	2.330 ± 0.060 g cm ⁻³	2.391 ± 0.097 g cm ⁻³	2.350 ± 0.046 g cm ⁻³ (calculated)
Grain volume			0.053 ± 0.0023 cm ³
Grain density = mass/grain volume			3.686 ± 0.161 g cm ⁻³
Porosity = [1-(bulk density/ grain density)] × 100%			(36.2 ± 3.0)%

same meteorite types as most of the AhS stones that have been studied so far and, like the other AhS stones, are predominantly ureilitic. Thus, the mineral clasts in 91A and 671 are broken-down fragments of the same materials represented by the lithic clasts (the other AhS stones) in 2008 TC₃. Based on these considerations, a plausible model for the structure and composition of 2008 TC₃ is that it was a breccia with a fine-grained, friable matrix like the C1 material in AhS 91A and AhS 671, which enclosed a small fraction of more coherent, few cm-sized, lithic clasts of ureilitic, OC, and EC materials, as well as smaller fragments (mineral fragments, chondrules, metal-sulfide particles) derived from comminution of similar materials. In the following subsections, we consider whether such a model is consistent with the VNIR reflectance spectrum and the density and porosity of 2008 TC₃.

Spectral Modeling

The reflectance spectrum of 2008 TC₃ was measured in the 0.55–1.00 μm range (Figs. 21c and 21d), and most closely matches F-type asteroids in the Tholen taxonomy (Jenniskens et al. 2009, 2010). F-type asteroids belong to the C complex of dark asteroids that are commonly identified with carbonaceous chondrites (Tholen and Barucci 1989; DeMeo et al. 2009, 2015). The albedo of the asteroid was not directly measured, but the average F-type albedo of 0.046 (Mainzer et al. 2011) is consistent with independent estimates of the asteroid's size (Jenniskens et al. 2009). Albedo estimates ranging from 0.046 to 0.12 (at 0.55 μm) have been proposed from laboratory spectra of some of the ureilitic AhS stones (Jenniskens et al. 2009; Hiroi et al. 2010).

Hiroi et al. (2010) obtained reflectance spectra of chips and powders of 10 AhS ureilites and one ordinary chondrite (Fig. 21b) and used least-squares modeling of linear combinations of these spectra to fit the spectrum of 2008 TC₃ in order to constrain the structure and composition of the asteroid. He found that mixtures dominated by chips and coarse powders of the ureilites, with only a small component (~4–10%) of OC, reproduced the main features of the asteroid spectrum (Figs. 21c and 21d), suggesting that ureilitic material dominated the surface of 2008 TC₃.

We extended this modeling to include the data obtained here for AhS 91A (Fig. 21a) and the enstatite chondrite (EC) stones AhS 1002 and AhS 2012 (Fig. 21b). Critical features of the asteroid spectrum are the lack of a strong spectral downturn shortward of ~0.7–0.8 μm and a shallow absorption at ~0.9 μm attributable to pyroxene. We parameterized these features as the 700/550, 900/550, and 1000/900 nm ratios, and used these as criteria for constructing linear mixtures of small numbers of components (4–5) that plausibly matched the spectrum of the asteroid. The asteroid spectrum used was the same 55 pt averaged spectrum that was used in Hiroi et al. (2010). Albedo was not a fixed constraint. We first focused on testing how large a component of AhS 91A would be consistent with the asteroid spectrum. Two of the best-fit mixtures from this modeling (mix 2 and mix 5) are shown in Figs. 21c and 21d (Table 15).

These two spectra show that mixtures of AhS ureilites + 0–3% AhS OC + 70–79% AhS 91A provide fits to the asteroid spectrum that are comparable in quality to those of the ureilite + OC mixtures of Hiroi et al. (2010) within the uncertainty of the asteroid spectrum, and therefore are consistent with there being a significant component of AhS 91A-like material in the asteroid. Furthermore, adding large fractions of AhS 91A to ureilites results in lower albedo values (Fig. 21d) that are within the range of those of F-type asteroids (<0.09, average 0.046; Mainzer et al. 2011), whereas the ureilite + OC mixtures of Hiroi et al. (2010) are not. This is a strong argument for there being a large component of AhS 91A-like material in the asteroid, because none of the other AhS stones studied so far (by VNIR reflectance spectroscopy) have lower albedos than the ureilites.

We then tested how large a component of EC would be consistent with the asteroid spectrum by adding up to 30% EC chips or powders to one of the ureilite + OC + AhS 91A mixtures (Fig. 21c). Results show that addition of 30% EC chips or powders (the percentage of EC among currently studied non-UOK AhS stones) results in a spectrum that is outside the uncertainty of the 55 pt averaged spectrum for 2008

Table 15. Properties of model spectral mixtures shown in Figs. 21c and 21d.

	% 91A	% OC	% ureilites	RELAB files	AhS stone	Type	State	Incidence angle
Mix 2	70.2	7	19.3	C1MT320	#91A	CC breccia	Chip	19
				C1MT94	#25	OC	Chip	30
				C1MT113	#27	Ureilite	Chip	30
				C1MT95	#7	Ureilite	Chip	30
Mix 5	41.9 37.1	21	3.5	C1MT319B, BKR1MT319B	#91A	CC breccia	125–500 μm powder	19
				C1MT319A, BKR1MT319A	#91A	CC breccia	<125 μm powder	30
				C1MT113B, BKR1MT319B	#27	Ureilite	125–500 μm powder	30

TC₃ over much of its spectral range. Addition of even 10% EC chips or powders results in a spectrum that deviates significantly from the averaged asteroid spectrum (though consistent with it within uncertainty) and therefore appears implausible.

Thus, based on currently available spectra for AhS stones, it is likely that asteroid 2008 TC₃ consisted dominantly of ureilitic and AhS 91A-like materials, with as much as 40–79% of the latter, and only small amounts (<10%) of OC, EC, and other meteorite types.

Density and Porosity

The bulk density determined for AhS 91A ($2.35 \pm 0.05 \text{ g cm}^{-3}$) is lower than the average bulk density ($\sim 2.8 \text{ g cm}^{-3}$) of 42 AhS ureilites (Welten et al. 2010), and significantly lower than densities of other AhS stone types such as EC (e.g., 3.5 g cm^{-3} ; Shaddad et al. 2010). It is also much closer than the ureilites to the bulk density estimates of $\sim 1.7\text{--}2.2 \text{ g cm}^{-3}$ for asteroid 2008 TC₃ (Welten et al. 2010). The porosity of AhS 91A (36%) is higher than the porosities of 36 of the 42 AhS ureilites measured, and within the range of estimates of porosity (33–50%) of the asteroid (Welten et al. 2010). These physical properties of AhS 91A are consistent with the results of the spectral modeling suggesting that material like AhS 91A could have comprised a large fraction of the asteroid. If we accept the argument of Welten et al. (2010) that the lower density (e.g., $\sim 1.7 \text{ g cm}^{-3}$) and higher porosity values (e.g., 50%) determined for the asteroid are the most robust, then AhS 91A is still denser and less porous than the asteroid. This is, in fact, consistent with the observation that the bulk of the asteroid disintegrated in the atmosphere, while AhS 91A survived. The asteroid could have contained some less dense, more porous material that we have not sampled, or it could have consisted mainly of a less dense, more porous version of AhS 91A. However, it is also likely that the asteroid had significant macroporosity (Consolmagno et al. 2008), which could account for the lower bulk density of the asteroid compared to AhS

91A and is consistent with its low strength and fragmentation behavior (Jenniskens et al. 2009).

Implications for the Formation of Asteroid 2008 TC₃

At least 13 different parent asteroids are represented among the AhS stones (Horstmann and Bischoff 2014; Goodrich et al. 2018). Two types of model have been proposed to explain how all these materials became mixed together in asteroid 2008 TC₃ (1) secondary accretion models (Bischoff et al. 2010; Gayon-Markt et al. 2012; Horstmann and Bischoff 2014; Scott et al. 2018) and (2) regolith models (Herrin et al. 2010; Hartmann et al. 2011; Goodrich et al. 2015a). Both models begin with catastrophic impact disruption of the ureilite parent body (UPB), an event which has been proposed based on evidence independent of AhS (Takeda 1987; Warren and Kallemeyn 1992; Goodrich et al. 2004, 2015a; Downes et al. 2008; Herrin et al. 2010; Michel et al. 2015), and which likely occurred at $\sim 5 \text{ Ma}$ after CAI formation (Goodrich et al. 2010, 2015a, 2015b, 2015c). Secondary accretion models for 2008 TC₃ posit that at the time of the catastrophic disruption, abundant fragments of mixed chondritic debris were present around the UPB and re-accreted along with the ureilitic fragments to form mixed second generation asteroids, one of which spawned 2008 TC₃. In contrast, regolith models for 2008 TC₃ posit that in the aftermath of the catastrophic disruption, daughter bodies consisting solely of ureilitic materials formed by gravitational re-accretion of subsets of fragments from the shattered parent (Michel et al. 2001, 2015). Over an extended period of time (tens of millions to billions), these ureilitic daughter bodies then developed regoliths consisting of comminuted fragments of their host ureilitic lithologies, as well as surviving remnants of foreign impactors. Goodrich et al. (2015a) suggested that one daughter body could be the source of all ureilitic material in our collections—main group ureilites from the interior, typical polymict ureilites (from deep, consolidated regolith [“asteroidal megaregolith”]), and AhS from shallower, less coherent regolith.

These two formation models make distinct predictions for the overall structure and composition of the asteroid. The secondary accretion model predicts that 2008 TC₃ consisted of centimeter(s)-sized, loosely agglomerated lithic components (i.e., similar to the studied AhS stones), and broke up mainly into monolithologic fragments along their original boundaries, with some of these fragments becoming the recovered stones (Bischoff et al. 2010). This suggests that the asteroid had relatively uniform clast sizes similar to those of the fallen fragments, and no strong distinction between clasts and matrix. In contrast, the regolith model predicts large variations in clast sizes and a distinct clast–matrix structure.

The structure of the AhS 91A and AhS 671 breccias strongly suggests that they formed in a regolith environment. Regolith (fragmentary debris) is produced through multiple large and small impacts onto an asteroid's surface over an extended period of time, leading to fragmentation, comminution, and redistribution of both indigenous asteroidal material and surviving fragments of impactors (McKay et al. 1989; Bischoff et al. 2006). The products of these combined processes include both regolith breccias (which resided on the outermost few mm of the surface for long enough to acquire solar wind [SW] implanted gases), and fragmental breccias, which formed at various depths below the surface and include materials that were not exposed to space for long enough to acquire solar gases. The observations that the clasts in AhS 91A and AhS 671 are small fragments of their parent meteorite types (i.e., ureilitic mineral fragments rather than complete ureilitic assemblages, enstatite chondrite metal grains rather than a representative piece of an enstatite chondrite, OC chondrules rather than a representative piece of an OC), and that diverse types of clast are intimately mixed over short distances, are consistent with regolith processes, and inconsistent with the predictions of the secondary accretion model. In addition, the physical properties of AhS 91A (i.e., much higher porosity than seen in CC of similar density) suggest that this material has been significantly “shaken and stirred,” as would occur in a regolith environment. Based on the absence (so far) of SW gases in AhS 91A and AhS 671, they are classified as fragmental breccias, which we argue formed dominantly in subsurface layers of a regolith environment.

However, on what type of parent asteroid did this regolith form? If these meteorites had been discovered independent of the other AhS stones, they would probably be considered a new type of carbonaceous chondrite breccia, formed on a carbonaceous chondrite asteroid with the ureilite, ordinary chondrite, and enstatite chondrite materials being foreign. Instead, we know that they are pieces of asteroid 2008 TC₃, which

has been assumed to be a ureilitic asteroid based on the predominance of ureilites among the studied AhS stones (Horstmann and Bischoff 2014; Goodrich et al. 2015a). This apparent paradox can be resolved by recognizing that regolith can be extremely heterogeneous, with some regions being dominated by material from a single impactor. In fact, two other types of asteroids—Vesta (a differentiated asteroid with a basaltic crust) and Psyche (thought to be metallic)—have extensive dark areas on their surfaces that are interpreted as remnants of CC-like impactors (Reddy et al. 2012, 2017; De Sanctis et al. 2012; Turrini et al. 2014; Takir et al. 2017). Thus, we hypothesize that 2008 TC₃ was a fragment of the regolith of a ureilitic asteroid, with AhS 91A and AhS 671 representing a volume of regolith that was dominated by the remnant of a CC-like body that impacted into an already well-gardened (finely comminuted) mixture of ureilitic + impactor-derived (e.g., OC and EC) fragments. Such an interpretation is supported by the dominance of ureilitic material in both AhS 91A/671 and AhS stones overall, and by comparisons between AhS and typical polymict ureilites discussed below.

Noble Gases—The Apparent Absence of SW Implanted Gases

Regolith breccias in meteorite collections are defined by their brecciated nature and the presence of SW derived noble gases that are implanted into the grain surfaces (100s of nm) in the upper meters of the regolith while the grains are still being impact gardened, prior to final compaction and lithification (Bischoff et al. 2006, 2018a). Typically, the gases are abundant and can easily dominate over the other noble gas components, particularly in He and Ne. Thus, the detection of SW in AhS 91A fragments would be unequivocal support for the regolith model suggested above.

The noble gas results obtained here for AhS 91A do not obviously show a Ne-SW component (Fig. 26), but they do not exclude the possibility that one is present. For example, the trapped endmember in all three samples could be a mixture of HL and SW in constant proportions (as indicated by the nearly constant trapped ²⁰Ne/²²Ne ratio of all samples, Fig. 26). However, it is also possible that the primordially trapped Ne component has a ²⁰Ne/²²Ne ratio above the typically dominating one in CI chondrites of HL (8.5) but well below SW-Ne (12.5–13.7, Fig. 26). This component would have a ²⁰Ne/²²Ne ratio of ~10.45, similar to what is found for carbonaceous carriers in carbonaceous chondrites (Q-gases) and the carbon-rich veins of ureilites (Göbel et al. 1978). The nearly constant trapped ²⁰Ne/²²Ne ratio of all three AhS fragments, including AhS 91A_14 with the largest trapped ²⁰Ne concentration (2× more than in the other two, Table 9), supports this interpretation, as a significant presence of

SW-Ne in AhS 91A_14 would increase the trapped $^{20}\text{Ne}/^{22}\text{Ne}$ ratio considerably. Furthermore, AhS 91A_14 also contains an Ar-, Kr-, and Ne-rich component (“subsolar”) that plots at the upper right end of the trend observed by Göbel et al. (1978) in their fig. 8 for several ureilites with strongly elevated $^{36}\text{Ar}/^{132}\text{Xe}$ and $^{84}\text{Kr}/^{132}\text{Xe}$ ratios. All noble gas patterns taken together may suggest that AhS 91A_14 simply contained more of the ureilitic, gas-rich material that is suggested to be carried in C-rich veins (Göbel et al. 1978), diamond, or amorphous C (see, e.g., Wieler et al. [2006] and references therein) whereas AhS 91A_12 and AhS 91A_15 contain more of the C1 material with typical Q-like elemental compositions.

It is possible that the SW component is present in AhS 91A but was not detected in our analyses. It has been shown that a SW-Ne component in grain surfaces can be hidden in analyses of bulk samples (i.e., swamped by the SW-poor grain interiors), particularly for CC samples that contain high concentrations of trapped gases (e.g., CI Ivuna: Riebe et al. 2017b). In such cases, minor contributions of SW can only be detected during stepwise gas extraction with a large number of steps, such as applied with the closed-system step etching technique (Riebe et al. 2017b). Thus, the presence or absence of SW gases in AhS 91A cannot be determined without further analyses.

The absence of SW gases in previously studied AhS stones (Murty et al. 2010; Ott et al. 2010; Welten et al. 2010; Meier et al. 2012; Nagao et al. 2014; Riebe et al. 2017a) has been cited as an argument against a regolith origin for 2008 TC₃ (Horstmann and Bischoff 2014). However, all previously analyzed AhS samples were from the interiors of well-consolidated stones, which we interpret as having been the larger clasts in 2008 TC₃ (a volumetrically minor component). SW gases would not necessarily be expected in such samples, even if they were derived from a regolith environment (see discussion in Riebe et al. 2017a). Furthermore, even the complete absence of SW gases in AhS 91A does not preclude a regolith origin. Solar gases are only implanted in the top millimeter of an asteroidal surface (Wieler et al. 1986), and even extensive gardening may not redistribute affected grains homogeneously in subsurface regolith layers. Solar gases in the typical polymict ureilites EET 83309 and 87720 are known to be heterogeneously distributed (Ott et al. 1990; Rai et al. 2003), showing that some bulk samples of even strictly defined (Bischoff et al. 2006) regolith breccias can be devoid of SW gases. All typical polymict ureilites are sufficiently similar petrographically that they are likely to have had a common origin (Goodrich et al. 2004; Downes et al. 2008); thus, the fact that some of them are regolith breccias (SW gas bearing) implies that

all of them (including the fragmental breccias) formed in a regolith environment. By analogy, the absence of SW in AhS 91A does not rule out 2008 TC₃ having formed as regolith.

AhS 91A has a low CRE (~5–9 Ma) compared with the previously analyzed AhS chondrites and ureilites (~11–22 Ma: Welten et al. 2010; Meier et al. 2012; Riebe et al. 2017a). Riebe et al. (2017a) suggested that the large spread in CRE ages in the AhS samples could be due to irradiation in a regolith environment. In such an environment, different clasts will spend different lengths of time in the upper ~2 m layer where they are exposed to cosmic rays producing cosmogenic noble gases, resulting in a spread in CRE ages. The low CRE ages of AhS 91A increase the CRE age spread of the AhS samples, consistent with a regolith origin of AhS.

Comparisons with Typical Polymict Ureilites

Similarities between typical polymict ureilites and AhS have been argued to support the regolith model for formation of 2008 TC₃ (Goodrich et al. 2015a). As mentioned above, typical polymict ureilites are fragmental and regolith breccias that are dominated by ureilitic materials but also contain multiple types of chondritic and non-ureilitic achondritic clasts (Prinz et al. 1986, 1987; Goodrich et al. 2004, 2015c, 2016, 2017b, 2017c; Bischoff et al. 2006; Downes et al. 2008; Ross et al. 2010). They are unique among meteoritic breccias for the large diversity of their foreign clasts (Bischoff et al. 2006). What makes AhS anomalous, then, is not that it contains many different meteorite types, but that it disaggregated in the atmosphere and its clasts landed on Earth as individual stones.

Goodrich et al. (2015a) argued that the differences between AhS and typical polymict ureilites were principally differences in structure (i.e., grain size, grain and/or clast size distribution, degree of lithification). The range of types and relative abundances of non-ureilitic materials in AhS do appear to differ from those in typical polymict ureilites, at least based on the AhS stones that have been studied to date. Enstatite chondrites and unique enstatite achondrites dominate among non-ureilitic AhS stones (Table 16), whereas enstatite meteorite clasts are rare in typical polymict ureilites (Goodrich et al. 2015b). However, Boleaga and Goodrich (2019) found that half of observed xenolithic metal-sulfide grains in several polymict ureilites were derived from enstatite chondrites, indicating that enstatite chondrites did contribute significant material. Furthermore, our spectral modeling (Fig. 21c) showed that enstatite chondrites could not have been as abundant in 2008 TC₃ as they are among currently

studied AhS stones, but perhaps were concentrated relative to other stone types during the fall or recovery.

Another apparent difference is that hydrous CC-like clasts are the most abundant foreign clast type (both in numbers and volume) in typical polymict ureilites (Goodrich et al. 2015b) whereas prior to the discovery of AhS 91A and AhS 671, no hydrous CCs had been found among AhS stones (Bischoff et al. 2010; Horstmann and Bischoff 2014). The C1 material in AhS 91A and AhS 671 is therefore a critical addition to the inventory of AhS meteorite types, particularly considering its mineralogic and oxygen isotope similarities to the CC-like clasts in typical polymict ureilites (Clayton and Mayeda 1988; Brearley and Prinz 1992; Patzek et al. 2018b; Goodrich et al. 2019a, 2019b). The presence of this component in AhS greatly strengthens the analogy between AhS and typical polymict ureilites, and thus supports the interpretation that 2008 TC₃ (like typical polymict ureilites) is a piece of ureilitic regolith.

Implications for Reflectance Spectroscopy of Asteroids

Regardless of the overall fraction of CC-dominated materials in 2008 TC₃, AhS 91A and AhS 671 provide direct evidence that such regions exist in ureilitic regolith. This has important implications for asteroid spectroscopy, because such regions would have an ~2.7 μm absorption band due to the water of hydration in their phyllosilicates (Figs. 21c and 21d). Depending on the areal extent of these regions, the ~2.7 μm band could be detectable in disk-resolved asteroid spectra. The presence of a 2.7–3.0 μm band is usually considered diagnostic of a carbonaceous chondrite asteroid (Rivkin 2012; Rivkin et al. 2015). However, recent investigations have found that the surfaces of Vesta (a basaltic asteroid) and Psyche (thought to be a metal-rich asteroid) have dark regions that show 2.7–3 μm absorption bands that are attributed to contamination by CC impactors (Reddy et al. 2012, 2017; DeSanctis et al. 2012; Turrini et al. 2014; Takir et al. 2017). The discovery of AhS 91A and AhS 671 shows that ureilitic asteroids can also have such regions. Furthermore, small asteroidal fragments consisting wholly of ureilitic regolith (e.g., 2008 TC₃) could have CC-dominated regions that constitute a significant fraction of their mass, in which case even disk-averaged spectra might show a 2.7–3.0 μm band leading to an incorrect interpretation of asteroid type.

SUMMARY

Almahata Sitta stones 91A and 671 are the first AhS stones to contain both ureilitic and chondritic

Table 16. Classification of Almahata Sitta nonureilites (#s of stones).

	all UoK (16 stones) ^{a,b}	non UoK (48 stones) ^{c,d}
E-meteorites	8	40
EH	4	9
EL	3	29
Unique E-achondrites	1	2
Ordinary chondrites	5	6
H	3	4
L	1	1
LL	1	1
Carbonaceous chondrites	3	1
C1-C2 hydrous	3	0
Metal-rich	0	1
Rumuruti-type chondrites	0	1

^aGoodrich et al. (2018).

^bZolensky et al. (2010).

^cHorstmann and Bischoff (2014).

^dBischoff et al. (2015a, 2016, 2018b, 2019).

lithologies. They are friable breccias, consisting of a hydrous CC-like lithology that encloses clasts of olivine, pyroxenes, plagioclase, graphite, and metal-sulfide, as well as chondrules and chondrule fragments. The CC lithology consists mainly of fine-grained serpentine and saponite, magnetite, carbonates (breunnerite and dolomite), fayalitic olivine, an unidentified Ca-rich silicate phase, and Fe,Ni sulfides. It has mineralogic similarities to known CI chondrites, but also shows heterogeneous thermal metamorphism (dehydration). Its bulk oxygen isotope composition ($\delta^{18}\text{O} = 13.53\text{‰}$, $\delta^{17}\text{O} = 8.93\text{‰}$) is unlike that of known CC, but is essentially identical to that of a several CC-like clasts in typical polymict ureilites. Its Cr isotope composition shows higher $\varepsilon^{54}\text{Cr}$ than any known meteorite. The clasts and chondrules do not belong to the CC lithology. The olivine, pyroxene, plagioclase, graphite, and some of the metal-sulfide clasts are ureilitic and represent at least six main group ureilite lithologies. The chondrules are most likely derived from OC and/or type 3 CC. Some of the metal-sulfide clasts are derived from EC.

AhS 91A and AhS 671 provide direct information about the structure and composition of asteroid 2008 TC₃ overall and could represent a substantial fraction of its pre-atmospheric mass. Their friability makes them plausible candidates for the bulk of the asteroid that was lost in the atmosphere. Spectral modeling using laboratory spectra of AhS stones suggests that 2008 TC₃ consisted dominantly of ureilitic and AhS 91A-like materials, with as much as 70% of the latter, and <10% of OC, EC, and other meteorite types. Physical properties of AhS 91A are also consistent with materials

like this comprising a large fraction of the asteroid. Its bulk density (2.35 g cm^{-3}) is lower than densities of most AhS ureilites and other stone types, and closer to estimates for the asteroid ($1.7\text{--}2.2 \text{ g cm}^{-3}$). Its porosity (36%) is within the range estimated for the asteroid (33–50%). Nevertheless, the fragmentation behavior of the asteroid suggests that it had significant macroporosity.

The texture of AhS 91A and AhS 671 supports the hypothesis that 2008 TC₃ represents regolith developed on a ureilitic asteroid. The observations that the clasts in these fragmental breccias are small, unrepresentative fragments of their parent meteorite types, and that diverse types of clast are intimately mixed, are consistent with regolith processes. The absence of a SW Ne component implies formation dominantly in subsurface layers that were not directly exposed to space for long enough to acquire solar gases. The observed spread in CRE ages among AhS stones (increased by AhS 91A) also argues for irradiation in a regolith environment where different clasts spend different amounts of time in the uppermost layers.

AhS 91A and AhS 671 provide direct evidence that CC-dominated regions exist in ureilitic regolith. Such regions would have an $\sim 2.7 \mu\text{m}$ absorption band due to the water of hydration in their phyllosilicates, which could be detectable in disk-resolved asteroid spectra. The presence of $2.7\text{--}3.0 \mu\text{m}$ band is usually considered diagnostic of a primitive, CC-like asteroid. AhS 91A and AhS 671 show that this interpretation may not always be correct.

Acknowledgments—We are grateful to Dave Draper and Lindsay Keller of ARES, JSC for making the JSC electron-beam facilities available for this work. We thank Allan Treiman and Tom Burbine for helpful discussions and encouragement. We thank Jessie Maisano and Matthew Colbert at the University of Texas (Austin), and Michele Secco at the University of Padova, for conducting XRCT scans. We thank Maciej Śliwiński for assisting with SIMS analyses of carbonate and running multiple standards. We appreciate the helpful reviews from Ed Cloutis, Alan Rubin, Addi Bischoff, and the Associate Editor Adrian Brearley. This work was supported by NASA grants 80NSSC17K0165, NNX17AH09GS03, and 80NSSC19K0507. WiscSIMS is partly supported by NSF (EAR03-19230, EAR-1658823). M.R. and H.B. thank the Swiss National Science Foundation for support through the framework of the NCCR “PlanetS” and grant P2EZP2_165234. This is LPI contribution #2212. LPI is operated by USRA under a cooperative agreement with the Science Mission

Directorate of the National Aeronautics and Space Administration.

Editorial Handling—Dr. Adrian Brearley

REFERENCES

- Afiatalab F. and Wasson J. T. 1980. Composition of the metal phases in ordinary chondrites: Implications regarding classification and metamorphism. *Geochimica et Cosmochimica Acta* 44:431–446.
- Akai J. 1980. Tubular form of interstratified mineral consisting of a serpentine-like layer plus two brucite-like sheets newly found in the Murchison (C2) meteorite. *Memoirs of the National Institute for Polar Research Special Issue* 17:299–310.
- Akai J. and Kanno J. 1986. Mineralogical study of matrix- and groundmass-phyllosilicates, and isolated olivines in Yamato-791198 and -793321: With special reference to new find of 14A chlorite in groundmass. *Memoirs of the National Institute for Polar Research Special Issue* 41:259–275.
- Alexander C. M. O’D., Cody G. D., De Gregorio B. T., Nittler L. R., and Stroud R. M. 2017. The nature, origin, and modification of insoluble organic matter in chondrites, the major source of Earth’s C and N. *Chemie der Erde-Geochemistry* 77:227–256.
- Bandfield J. L., Edgett K. S., and Christensen P. R. 2002. Spectroscopic study of the Moses Lake dune field, Washington: Determination of compositional distributions and source lithologies. *Journal of Geophysical Research* 107:5092. <https://doi.org/5010.1029/2000JE001469>.
- Barber D. J. 1981. Matrix phyllosilicates and associated minerals in C2M carbonaceous chondrites. *Geochimica et Cosmochimica Acta* 45:945–970.
- Barber D. J. 1985. Phyllosilicates and other layer-structured materials in stony meteorites. *Clay Minerals* 20:415–454.
- Benedix G. K., McCoy T. J., Keil K., Bogard D. D., and Garrison D. H. 1998. A petrologic and isotopic study of winonaite: Evidence for early partial melting, brecciation, and metamorphism. *Geochimica et Cosmochimica Acta* 62:2535–2553.
- Bischoff A. 2000. Mineralogical characterization of primitive, type-3 lithologies in Rumuruti chondrites. *Meteoritics & Planetary Science* 35:699–706.
- Bischoff A., Scott E. R. D., Metzler K., and Goodrich C. A. 2006. Nature and origin of meteoritic breccias. In *Meteorites and the early solar system II*, edited by Lauretta D. S. and McSween H. Y. Jr. Tucson, Arizona: The University of Arizona Press. pp. 679–714.
- Bischoff A., Horstmann M., Pack A., Laubenstein M., and Haberer S. 2010. Asteroid 2008 TC₃—Almahata Sitta: A spectacular breccia containing many different ureilitic and chondritic lithologies. *Meteoritics & Planetary Science* 45:1638–1656.
- Bischoff A., Vogel N., and Roszjar J. 2011. The Rumuruti chondrite group. *Chemie der Erde* 71:101–133.
- Bischoff A., Ebert S., Patzek M., Horstmann M., Pack A., Barrat J.-A., and Decker S. 2015a. New individuals from the Almahata Sitta strewn field: Old friends and brand-new fellows (abstract #5092). 78th Annual Meeting of the Meteoritical Society.

- Bischoff A., Horstmann M., Barrat J.-A., Chaussidon M., Pack A., Herwatz D., Ward D., Vollmer C., and Decker S. 2015b. Trachyandesitic volcanism in the early solar system. *Proceedings of the National Academy of Sciences* 111:12,689–12,692.
- Bischoff A., Ebert S., Patzek M., Horstmann M., Pack A., and Decker S. 2016. Almahata Sitta news: Well-known varieties and new species in the zoo (abstract #6319). 79th Annual Meeting of the Meteoritical Society.
- Bischoff A., Schleiting M., Wieler R., and Patzek M. 2018a. Brecciation among 2280 ordinary chondrites—Constraints on the evolution of their parent bodies. *Geochimica et Cosmochimica Acta* 238:516–541.
- Bischoff A., Kraemer A.-K., Klemm K. I., and Decker S. 2018b. News from the Almahata Sitta strewn field—Seven new samples: Three ureilites, three enstatite chondrites, and one ordinary chondrite (abstract #2067). 81st Annual Meeting of the Meteoritical Society.
- Bischoff A., Lentfort S., Möhlmann K., Klemm K., and Haberer S. 2019. Mineralogical characteristics of 20 new samples from the Almahata Sitta strewnfield (abstract #6030). 82nd Annual Meeting of the Meteoritical Society.
- Bishop J. L., Murad E., and Dyar M. D. 2002. The influence of octahedral and tetrahedral cation substitution on the structure of smectites and serpentines as observed through infrared spectroscopy. *Clay Minerals* 37:617–628.
- Bland P. A., Cressey G., Alard O., Rogers N. W., Forder S. D., and Gounelle M. 2002. Modal mineralogy of carbonaceous chondrites, and chemical variation in chondrite matrix (abstract #1754). 33rd Lunar and Planetary Science Conference. CD-ROM.
- Bland P. A., Cressey G., and Menzies N. 2004. Modal mineralogy of carbonaceous chondrites by X-ray diffraction and Mossbauer spectroscopy. *Meteoritics & Planetary Science* 39:3–16.
- Boleaga Y. and Goodrich C. A. 2019. Xenolithic Fe,Ni metal in polymict ureilite meteorites (abstract #1622). 50th Lunar and Planetary Science Conference. CD-ROM.
- Borovička J. and Charvát Z. 2009. Meteosat observation of the atmospheric entry of 2008 TC₃ over Sudan and the associated dust cloud. *Astronomy and Astrophysics* 507:1015–1022.
- Böstrom K. and Fredriksson K. 1966. Surface conditions of the Orgueil meteorite parent body as indicated by mineral associations. *Smithsonian Miscellaneous Collections* 151:1–39.
- Botta O. and Bada J. L. 2002. Extraterrestrial organic compounds in meteorites. *Surveys in Geophysics* 23:411–467.
- Brearley A. J. 1995. Aqueous alteration and brecciation in Bells, an unusual, saponite-bearing CM carbonaceous chondrite. *Geochimica et Cosmochimica Acta* 59:2291–2317.
- Brearley A. J. and Jones R. H. 1998. Chondritic meteorites. In *Planetary materials*, edited by Papike J. J. Washington, D.C.: Mineralogical Society of America. pp. 3.1-3-398.
- Brearley A. J. and Prinz M. 1992. CI chondrite-like clasts in the Nilpena polymict ureilite. Implications for aqueous alteration processes in CI chondrites. *Geochimica et Cosmochimica Acta* 56:1373–1386.
- Briani G., Gounelle M., Bourot-Denise M., and Zolensky M. E. 2012. Xenoliths and microxenoliths in H chondrites: Sampling the zodiacal cloud in the asteroid Main Belt. *Meteoritics & Planetary Science* 47:880–902.
- Browning L. B., McSween H. Y. Jr., and Zolensky M. E. 1996. Correlated alteration effects in CM carbonaceous chondrites. *Geochimica et Cosmochimica Acta* 60:2621–2633.
- Buroni A. and Folco L. 2008. Frontier Mountain meteorite specimens of the acapulcoite-lodranite clan: Petrography, pairing, and parent-rock lithology of an unusual intrusive rock. *Meteoritics & Planetary Science* 43:731–744.
- Busemann H., Baur H., and Wieler R. 2000. Primordial noble gases in “phase Q” in carbonaceous and ordinary chondrites studied by closed-system stepped etching. *Meteoritics & Planetary Science* 35:949–973.
- Che C., Glotch T. D., Bish D. L., Michalski J. R., and Xu W. 2011. Spectroscopic study of the dehydration and/or dehydroxylation of phyllosilicate and zeolite minerals. *Journal of Geophysical Research* 116:E05007.
- Chesley S., Chodas P., and Yeomans S. 2008. NASA/JPL Near-Earth Object Program Office statement. <http://neo.jpl.nasa.gov/news/2008tc3.html>.
- Clayton R. N. and Mayeda T. K. 1988. Formation of ureilites by nebular processes. *Geochimica et Cosmochimica Acta* 52:1313–1318.
- Clayton R. N. and Mayeda T. K. 1996. Oxygen isotope studies of achondrites. *Geochimica et Cosmochimica Acta* 60:1999–2017.
- Cohen B. A., Goodrich C. A., and Keil K. 2004. Feldspathic clast populations in polymict ureilites: Stalking the missing basalts from the ureilite parent body. *Geochimica et Cosmochimica Acta* 68:4249–4266.
- Consolmagno G. J., Britt D. T., and Macke R. J. 2008. The significance of meteorite density and porosity. *Chemie der Erde-Geochemistry* 68:1–29.
- Day J. M. D., Corder C. A., Rumble D. III, Assayag N., Cartigny P., and Taylor L. A. 2015. Differentiation processes in FeO-rich asteroids revealed by achondrite Lewis Cliff 88763. *Meteoritics & Planetary Science* 50:1750–1766.
- De Leuw S., Rubin A. E., and Wasson J. T. 2010. Carbonates in CM chondrites: Complex formational histories and comparison to carbonates in CI chondrites. *Meteoritics & Planetary Science* 45:513–530.
- De Sanctis M. C., Combe J.-P., Ammannito E., Palomba E., Longobardo A., McCord T. B., Marchi S., Capaccioni F., Capria M. T., Mittlefehldt D. W., Pieters C. M., Sunshine J., Tosi F., Zambon F., Carraro F., Fonte S., Frigeri A., Magni G., Raymond C. A., Russell C. T., and Turrini D. 2012. Detection of widespread hydrated materials on Vesta by the VIR imaging spectrometer on board the Dawn mission. *Astrophysics Journal* 758(1–5):L36.
- Deer W. A., Howie R. A., and Zussman J. 1962. *Rock forming minerals. Volume 3. Sheet silicates*. London: Longman Group Limited, 269 pp.
- Delaney J. S., Zanda B., Clayton R. N., and Mayeda T. 2000. Zag(b): A ferroan achondrite intermediate between brachinites and lodranites (abstract #1745). 31st Lunar and Planetary Science Conference. CD-ROM.
- DeMeo F. E., Binzel R. P., Slivan S. M., and Bus S. J. 2009. An extension of the Bus asteroid taxonomy into the near-infrared. *Icarus* 202:160–180.
- DeMeo F. E., Alexander C. M. O'D., Walsh K. J., Chapman C. R., and Binzel R. P. 2015. The compositional structure of the asteroid belt. In *Asteroids IV*, edited by Michel P., DeMeo F. E., and Bottke W. F. Tucson, Arizona: The University of Arizona Press. pp. 13–42.
- Downes H., Mittlefehldt D. W., Kita N. T., and Valley J. W. 2008. Evidence from polymict ureilites for a disrupted and re-accreted single ureilite parent asteroid gardened by

- several distinct impactors. *Geochimica et Cosmochimica Acta* 72:4825–4844.
- Dunn T. L., Gross J., Ivanova M. A., Runyon S. E., and Bruck A. M. 2016. Magnetite in the unequilibrated CK chondrites: Implications for metamorphism and new insights into the relationship between the CV and CK chondrites. *Meteoritics & Planetary Science* 51:1701–1720.
- Ehlers K. and El Goresy A. 1988. Normal and reverse zoning in niningerite: a novel key parameter to the thermal histories of EH-chondrites. *Geochimica et Cosmochimica Acta* 52:877–887.
- El Goresy A., Yabuki H., Ehlers K., Woolum D., and Pernicka E. 1988. Qingzhen and Yamato-691: A tentative alphabet for the EH chondrites. *Proceedings of the National Institute for Polar Research Symposium on Antarctic Meteorites* 1:65–101.
- Endress M. and Bischoff A. 1996. Carbonates in CI chondrites: Clues to parent body evolution. *Geochimica et Cosmochimica Acta* 60:489–507.
- Farmer V. C. 1974. *The infrared spectra of minerals*. London: Mineralogical Society.
- Fioretti A. M., Goodrich C. A., Shaddad M., Jenniskens P., Zolensky M., Kohl I., Young E., Rumble D., Kita N., Hiroi T., Turrin B., and Herzog G. 2017. A report on 63 newly sampled stones of the Almahata Sitta fall (asteroid 2008 TC₃) from the University of Khartoum collection, including a C2 carbonaceous chondrite (abstract #1846). 48th Lunar and Planetary Science Conference. CD-ROM.
- Fleet M. 2003. *Rock forming minerals. Volume 3A. Sheet silicates: Micas*, 2nd ed. London: The Geological Society, 758 pp.
- Folinsbee K., Douglas J. A. V., and Maxwell J. A. 1967. Revelstoke, a new Type I carbonaceous chondrite. *Geochimica et Cosmochimica Acta* 31:1625–1635.
- Frank D. R., Zolensky M. E., and Le L. 2014. Olivine in terminal particles of Stardust aerogel tracks and analogous grains in chondrite matrix. *Geochimica et Cosmochimica Acta* 142:240–259.
- Fredriksson K. and Kerridge J. F. 1988. Carbonates and sulfates in CI chondrites: Formation by aqueous activity on the parent body. *Meteoritics* 23:35–44.
- Gardner-Vandy K. G., Lauretta D. S., Greenwood R. C., McCoy T. J., and Killgore M. 2012. The Tafassasset primitive achondrite: Insights into initial stages of planetary differentiation. *Geochimica et Cosmochimica Acta* 85:142–159.
- Gardner-Vandy K. G., Lauretta D. S., and McCoy T. J. 2013. A petrologic, thermodynamic and experimental study of brachinites: Partial melt residues of an R chondrite-like precursor. *Geochimica et Cosmochimica Acta* 122:36–57.
- Gayon-Markt J., Delbo M., Morbidelli A., and Marchi S. 2012. On the origin of the Almahata Sitta meteorite and 2008 TC₃ asteroid. *Monthly Notices of the Royal Astronomical Society* 424:508–518.
- Göbel R., Ott U., and Begemann F. 1978. On trapped noble gases in ureilites. *Journal of Geophysical Research* 83:855–867.
- Goldstein J. I., Huss G. R., and Scott E. R. D. 2017. Ion microprobe analyses of carbon in Fe-Ni metal in iron meteorites and mesosiderites. *Geochimica et Cosmochimica Acta* 200:367–407.
- Gooding J. L. and Keil K. 1981. Relative abundances of chondrule primary textural types in ordinary chondrites and their bearing on conditions of chondrule formation. *Meteoritics* 16:17–43.
- Goodrich C. A. and Righter K. 2000. Petrology of unique achondrite Queen Alexandra Range 93148: A piece of the pallasite (howardite-eucrite-diogenite?) parent body? *Meteoritics & Planetary Science* 35:521–535.
- Goodrich C. A. and Wilson L. 2014. Feldspathic clast populations in polymict ureilites: determining the compositions of melts and the mode of melt extraction on the ureilite parent body (abstract #1342). 45th Lunar and Planetary Science Conference. CD-ROM.
- Goodrich C. A., Jones J. H., and Berkley J. L. 1987. Origin and evolution of the ureilite parent magmas: Multi-stage igneous activity on a large parent body. *Geochimica et Cosmochimica Acta* 51:2255–2274.
- Goodrich C. A., Fioretti A. M., Tribaudino M., and Molin G. 2001. Primary trapped melt inclusions in olivine in the olivine-augite-orthopyroxene ureilite Hughes 009. *Geochimica et Cosmochimica Acta* 65:621–652.
- Goodrich C. A., Scott E. R. D., and Fioretti A. M. 2004. Ureilitic breccias: Clues to the petrologic structure and impact disruption of the ureilite parent body. *Chemie der Erde - Geochemistry* 64:283–327.
- Goodrich C. A., Wlotzka F., Ross D. K., and Bartoschewicz R. 2006. NWA 1500: Plagioclase-bearing monomict ureilite or ungrouped achondrite? *Meteoritics & Planetary Science* 41:925–952.
- Goodrich C. A., Fioretti A. M., and Van Orman J. A. 2009. Petrogenesis of augite-bearing ureilites Hughes 009 and FRO 90054/93008 inferred from melt inclusions. *Geochimica et Cosmochimica Acta* 73:3055–3076.
- Goodrich C. A., Hutcheon I. D., Kita N. T., Huss G. R., Cohen B. A., and Keil K. 2010. ⁵³Mn-⁵³Cr and ²⁶Al-²⁶Mg ages of a feldspathic lithology in polymict ureilites. *Earth and Planetary Science Letters* 295:531–540.
- Goodrich C. A., Kita N. T., Spicuzza M. K., Valley J. W., Zipfel J., Mikouchi T., and Miyamoto M. 2011. The Northwest Africa 1500 meteorite: Not a ureilite, maybe a brachinite. *Meteoritics & Planetary Science* 45:1906–1928.
- Goodrich C. A., Sutton S. R., Wirick S., and Jercinovic M. J. 2013a. Chromium valences in ureilite olivine and implications for ureilite petrogenesis. *Geochimica et Cosmochimica Acta* 122:280–305.
- Goodrich C. A., Ash R. D., Van Orman J. A., Domanik K., and McDonough W. F. 2013b. Metallic phases and siderophile elements in main group ureilites: Implications for ureilite petrogenesis. *Geochimica et Cosmochimica Acta* 112:340–373.
- Goodrich C. A., Harlow G., Van Orman J. A., Sutton S. R., Jercinovic M. J., and Mikouchi T. 2014. Petrology of chromite in ureilites: Deconvolution of primary oxidation states and secondary reduction processes. *Geochimica et Cosmochimica Acta* 135:126–169.
- Goodrich C. A., Hartmann W. K., O'Brien D. P., Weidenschilling S., Wilson L., Michel P., and Jutzi M. 2015a. Origin and history of ureilitic material in the solar system: The view from asteroid 2008 TC₃ and the Almahata Sitta meteorite. *Meteoritics & Planetary Science* 50:782–809.
- Goodrich C. A., Fioretti A. M., O'Brien D. P., Zolensky M., Jenniskens P., and Shaddad M. H. 2015b. Comparing the foreign clast populations of Almahata Sitta and typical polymict ureilites, with implications (abstract #5018). 78th Annual Meeting of the Meteoritical Society.
- Goodrich C. A., Mikouchi T., and Treiman A. H. 2015c. A volcanic (quenched) angrite clast in polymict ureilite DaG

- 319 (abstract #5048). 78th Annual Meeting of the Meteoritical Society.
- Goodrich C. A., Treiman A. H., Kita N. T., and Defouilloy C. 2016. Increasing diversity of ordinary chondrite and Rumuruti-type chondrites clasts in polymict ureilites (abstract #1617). 47th Lunar and Planetary Science Conference. CD-ROM.
- Goodrich C. A., Treiman A. H., and Boyle S. 2017a. Melt formation and evolution on the ureilite parent body, as shown by feldspathic clasts in polymict ureilites (abstract #1196). 48th Lunar and Planetary Science Conference. CD-ROM.
- Goodrich C. A., Kita N. T., Yin Q.-Z., Sanborn M. E., Williams C. D., Nakashima D., Lane M. D., and Boyle S. 2017b. Petrogenesis and provenance of ungrouped achondrite Northwest Africa 7325 from petrology, trace elements, oxygen, chromium and titanium isotopes, and mid-IR spectroscopy. *Geochimica et Cosmochimica Acta* 203:381–403.
- Goodrich C. A., Ross D. K., and Treiman A. H. 2017c. A new type of foreign clast in a polymict ureilite: A CAI or Al-rich chondrule (abstract #1101). 48th Lunar and Planetary Science Conference. CD-ROM.
- Goodrich C. A., Kita N. T., Sutton S. R., Wirick S., and Gross J. 2017e. The Miller Range 090340 and 090206 meteorites: New brachinite-like achondrites with implications for the diversity and petrogenesis of the brachinite clan. *Meteoritics & Planetary Science* 52:949–978.
- Goodrich C. A., Fioretti A. M., Zolensky M., Shaddad M., Ross D. K., Kohl I., Young E., Kita N., Hiroi T., Śliwiński M. G., and Jenniskens P. 2018. The Almahata Sitta polymict ureilite from the University of Khartoum collection: Classification, distribution of clast types in the strewn field, new meteorite types, and implications for the structure of asteroid 2008 TC₃ (abstract #1321). 49th Lunar and Planetary Science Conference. CD-ROM.
- Goodrich C.A., Zolensky M., Kohl I., Young E. D., Yin Q. – Z., Sanborn M. E., and Shaddad M. H. 2019a. Carbonaceous chondrite-like xenoliths in polymict ureilites: A large variety of unique outer solar system materials (abstract #1312). 50th Lunar and Planetary Science Conference. CD-ROM.
- Goodrich C.A., Kita N. T., Zolensky M., and Shaddad M. H. 2019b. Oxygen isotope compositions of magnetite in CC-like clasts from Almahata Sitta and other polymict ureilites (abstract #1551). 50th Lunar and Planetary Science Conference. CD-ROM.
- Gounelle M., Zolensky M. E., Liou J.-C., Bland P. A., and Alard O. 2003. Mineralogy of carbonaceous chondritic microclasts in howardites: Identification of C2 fossil micrometeorites. *Geochimica et Cosmochimica Acta* 67:507–527.
- Grasa G., Martínez I., Diego M., and Abanades J. 2014. Determination of CaO carbonation kinetics under recarbonation conditions. *Energy & Fuels* 28:4033–4042.
- Green H. W., Radcliffe S. V., and Heuer A. H. 1971. Allende meteorite: A high voltage electron petrographic study. *Science* 172:936–939.
- Greenwood R. C., Franchi I. A., Kearsley A. T., and Alard O. 2010. The relationship between CK and CV chondrites. *Geochimica et Cosmochimica Acta* 74:1684–1705.
- Greshake A. 2014. A strongly hydrated microclast in the Rumuruti chondrite NWA 6828: Implications for the distribution of hydrous material in the solar system. *Meteoritics & Planetary Science* 49:824–841.
- Hamilton V. E. 2018. Spectral classification of ungrouped carbonaceous chondrites I: Data collection and processing (abstract #1759). 49th Lunar and Planetary Science Conference. CD-ROM.
- Hamilton V. E. and Ruff S. W. 2012. Distribution and characteristics of Adirondack-class basalt as observed by Mini-TES in Gusev crater, Mars and its possible volcanic source. *Icarus* 218:917–949.
- Hamilton V. E. and Connolly H. C. Jr. 2012. In situ microspectroscopy of a Type B CAI in Allende: Mineral identification in petrographic context (abstract #2495). 43rd Lunar and Planetary Science Conference. CD-ROM.
- Hamilton V. E., Abreu N. M., Bland P. A., Connolly H. C. Jr., Hanna R. D., Lauretta D. S., and Schrader D. L. 2018. Spectral classification of ungrouped carbonaceous chondrites II: Parameters and comparison to independent measures (abstract #1753). 49th Lunar and Planetary Science Conference. CD-ROM.
- Harju E. R., Rubin A. E., Ahn I., Choi B.-G., Ziegler K., and Wasson J. T. 2014. Progressive aqueous alteration of CR carbonaceous chondrites. *Geochimica et Cosmochimica Acta* 139:267–292.
- Hartmann W. K., Goodrich C. A., O'Brien D. P., Michel P., Weidenschilling S. J., and Sykes M. V. 2011. Breakup and reassembly of the ureilite parent body, formation of 2008 TC₃/Almahata Sitta, and delivery of ureilites to Earth (abstract #1360). 42nd Lunar and Planetary Science Conference. CD-ROM.
- Hayes J. M. 1967. Organic constituents of meteorites—A review. *Geochimica et Cosmochimica Acta* 31:1395–1440.
- Heber V. S., Wieler R., Baur H., Olinger C., Friedmann T. A., and Burnett D. S. 2009. Noble gas composition of the solar wind as collected by the Genesis mission. *Geochimica et Cosmochimica Acta* 73:7414–7432.
- Herrin J. S., Zolensky M. E., Ito M., Le L., Mittlefehldt D. W., Jenniskens P., Ross A. J., and Shaddad M. H. 2010. Thermal and fragmentation history of ureilitic asteroids: Insights from the Almahata Sitta fall. *Meteoritics & Planetary Science* 45:1789–1803.
- Herrin J. S., Zolensky M. E., Cartwright J. A., Mittlefehldt D. W., and Ross D. K. 2011. Carbonaceous chondrite-rich howardites: The potential for hydrous lithologies on the HED parent (abstract #2806). 42nd Lunar and Planetary Science Conference. CD-ROM.
- Hildebrand A. R., McCausland P. J. A., Brown P. G., Longstaffe F. J., Russell S. D. J., Tagliaferri E., Wacker J. F., and Mazur M. J. 2006. The fall and recovery of the Tagish Lake meteorite. *Meteoritics & Planetary Science* 41:407–431.
- Hiroi T., Jenniskens P., Bishop J. L., Shatir T. S. M., Kudoda A. M., and Shaddad M. H. 2010. Bi-directional visible-NIR and biconical FT-IR reflectance spectra of Almahata Sitta meteorite samples. *Meteoritics & Planetary Science* 45:1836–1845.
- Hiroi T., Milliken R. E., Pieters C. M., Kaiden H., Imae N., Yamaguchi A., Kojima H., Sasaki S., Matsuoka M., Sato Y., and Nakamura T. 2017. Visible and near-infrared spectral survey of carbonaceous chondrites and its application to HAYABUSA 2 (abstract #1086). 48th Lunar and Planetary Science Conference. CD-ROM.
- Horstmann M. and Bischoff A. 2014. The Almahata Sitta polymict breccia and the late accretion of asteroid 2008 TC₃. *Chemie der Erde - Geochemistry* 74:149–183.

- Horstmann M., Humayun M., and Bischoff A. 2014. Clues to the origin of metal in Almahata Sitta EL and EH chondrites and implications for primitive E chondrite thermal histories. *Geochimica et Cosmochimica Acta* 140:720–744.
- Howard K. T., Alexander C. M. O. D., Schrader D. L., and Dyl K. A. 2015. Classification of hydrous meteorites (CR, CM and C2 ungrouped) by phyllosilicate fraction: PSD-XRD modal mineralogy and planetesimal environments. *Geochimica et Cosmochimica Acta* 149:206–222.
- Huss G. R. and Lewis R. S. 1994. Noble gases in presolar diamonds I: Three distinct components and their implications for diamond origins. *Meteoritics* 29:791–810.
- Huss G. R. and Lewis R. S. 1995. Presolar diamond, SiC, and graphite in primitive chondrites: Abundances as a function of meteorite class and petrologic type. *Geochimica et Cosmochimica Acta* 59:115–160.
- Ikeda Y. 1983. Alteration of chondrules and matrices in the four Antarctic carbonaceous chondrites ALH-77307(C3), Y-790123(C2), Y-75293(C2), and Y-74662(C2). *Proceedings of the National Institute of Polar Research Special Issue* 30:93–108.
- Ikeda Y., Prinz M., and Nehru C. E. 2000. Lithic and mineral clasts in the Dar al Gani (DaG) 319 polymict ureilite. *Antarctic Meteorite Research* 13:177–221.
- Ikeda Y., Kita N. T., Morishita Y., and Weisberg M. K. 2003. Primitive clasts in the Dar al Gani 319 polymict ureilite: precursors of the ureilites. *Antarctic Meteorite Research* 16:105–127.
- Inoue M., Mikouchi T., and Goodrich C. A. 2016. Petrography and mineralogy of Northwest Africa 3222: Magmatically zoned augite-bearing ureilite with only little carbon (abstract #6417). 79th Annual Meeting of the Meteoritical Society.
- Jaques A. L. and Fitzgerald M. J. 1982. The Nilpena ureilite, an unusual polymict breccia: Implications for origin. *Geochimica et Cosmochimica Acta* 46:893–900.
- Jenniskens P., Shaddad M. H., Numan D., Elsir S., Kudoda A. M., Zolensky M. E., Le L., Robinson G. A., Friedrich J. M., Rumble D., Steele A., Chesley S. R., Fitzsimmons A., Duddy S., Hsieh H. H., Ramsay G., Brown P. G., Edwards W. N., Tagliaferri E., Boslough M. B., Spalding R. E., Dantowitz R., Kozubal M., Pravec P., Borovička J., Charvát Z., Vaubaillon J., Kuiper J., Albers J., Bishop J., Mancinelli R. L., Sandford S. A., Milam S. N., Nuevo M., and Worden S. P. 2009. The impact and recovery of asteroid 2008 TC₃. *Nature* 458:485–488.
- Jenniskens P., Vaubaillon J., Binzel R. P., Demeo F. E., Desvorné D., Bottke W. F., Fitzsimmons A., Hiroi T., Marchis F., Bishop J. L., Vernazza P., Zolensky M. E., Herrin J. S., Welten K. C., Meier M. M. M., and Shaddad M. H. 2010. Almahata Sitta (=asteroid 2008 TC₃) and the search for the ureilite parent body. *Meteoritics & Planetary Science* 45:1590–1617.
- Johnson C. A. and Prinz M. 1993. Carbonate compositions in CM and CI chondrites and implications for aqueous alteration. *Geochimica et Cosmochimica Acta* 57:2843–2852.
- Jones R. H. 2012. Petrographic constraints on the diversity of chondrule reservoirs in the protoplanetary disk. *Meteoritics & Planetary Science* 47:1176–1190.
- Kallemeyn G. W., Rubin A. E., Wang D., and Wasson J. T. 1989. Ordinary chondrites: Bulk compositions, classification, lithophile-element fractionations, and composition-petrographic type relationships. *Geochimica et Cosmochimica Acta* 53:2747–2767.
- Keller L. P., Thomas K. L., Clayton R. N., Mayeda T. K., DeHart J. M., and McKay D. S. 1994. Aqueous alteration of the Bali CV3 chondrite: Evidence from mineralogy, mineral chemistry, and oxygen isotopic compositions. *Geochimica et Cosmochimica Acta* 58:5589–5598.
- Kerridge J. F. 1985. Carbon, hydrogen and nitrogen in carbonaceous chondrites: Abundances and isotopic compositions in bulk samples. *Geochimica et Cosmochimica Acta* 49:1701–1714.
- Kimura M., Tsuchiyama A., Fukuoka T., and Imura Y. 1992. Antarctic primitive achondrites Yamato-74025, -75300, and 75305: Their mineralogy, thermal history, and the relevance to winonaite. *Proceedings, National Institute of Polar Research Symposium on Antarctic Meteorites* 5:165–190.
- Kita N. T., Ikeda Y., Togashi S., Liu Y., Morishita Y., and Weisberg M. K. 2004. Origin of ureilites inferred from a SIMS oxygen isotopic and trace element study of clasts in the Dar al Gani 319 polymict ureilite. *Geochimica et Cosmochimica Acta* 68:4213–4235.
- Kita N. T., Goodrich C. A., Fu B., Spicuzza M. J., and Valley J. W. 2006. Oxygen isotopes in mafic and feldspathic clasts from polymict ureilites (abstract #5161). 69th Annual Meeting of the Meteoritical Society. *Meteoritics & Planetary Science* 41 (Suppl.):A96.
- Kita N. T., Nagahara H., Tachibana S., Tomomura S., Spicuzza M. J., Fournelle J. H., and Valley J. W. 2010. High precision SIMS oxygen three isotope study of chondrules in LL3 chondrites: Role of ambient gas during chondrule formation. *Geochimica et Cosmochimica Acta* 74:6610–6635.
- Kita N. T., Defouilloy C., Goodrich C. A., and Zolensky M. E. 2017. Oxygen isotope ratios of magnetite in CI-like clasts from a polymict ureilite (abstract #6153). 80th Annual Meeting of the Meteoritical Society.
- Klimentidis R. and MacKinnon I. D. R. 1986. High resolution imaging of ordered mixed-layer clays. *Clays and Clay Minerals* 34:155–164.
- Kojima H., Ikeda Y., and Yanai K. 1984. The alteration of chondrules and matrices in new Antarctic carbonaceous chondrites. *Proceedings 9th Symposium on Antarctic Meteorites NIPR Special Issue* 35:184–199.
- Kornacki A. S. and Wood J. A. 1984. The mineral chemistry and origin of inclusion matrix and meteorite matrix in the Allende CV3 chondrite. *Geochimica et Cosmochimica Acta* 48:1663–1676.
- Kowalski R. A. 2008. MPEC 2008-T50:2008TC3. <https://minorplanetcenter.net/iau/mpec/K08/K08T50.html>.
- Kozubal M. J., Gasdia F. W., Dantowitz R. F., Scheirich P., and Harris A. W. 2011. Photometric observations of Earth-impacting asteroid 2008 TC₃. *Meteoritics & Planetary Science* 46:534–542.
- Krot A. N., Scott E. R. D., and Zolensky M. E. 1995. Mineralogical and chemical modification of components in CV3 chondrites: Nebular or asteroidal processing? *Meteoritics* 30:748–775.
- Kunihiro T., Rubin A. E., McKeegan K. D., and Wasson J. T. 2004. Oxygen-isotopic compositions of relict and host grains in chondrules in the Yamato 81020 CO3.0 chondrite. *Geochimica et Cosmochimica Acta* 68:3599–3606.
- Lane M. D. and Christensen P. R. 1997. Thermal infrared emission spectroscopy of anhydrous carbonates. *Journal of Geophysical Research* 102:25,581–25,592.

- Lane M. D., Glotch T. D., Dyar M. D., Pieters C. M., Klima R., Hiroi T., Bishop J. L., and Sunshine J. 2011. Mid-infrared spectroscopy of synthetic olivines: Thermal emission, specular and diffuse reflectance, and attenuated total reflectance studies of forsterite to fayalite. *Journal of Geophysical Research* 116. <https://doi.org/10.1029/2010JE003588>
- Le Guillou C., Changela H. G., and Brearley A. J. 2015. Widespread oxidized and hydrated amorphous silicates in CR chondrites matrices: Implications for alteration conditions and H₂ degassing of asteroids. *Earth and Planetary Science Letters* 420:162–173.
- Leshin L. A., Rubin A. E., and McKeegan K. D. 1997. The oxygen isotopic composition of olivine and pyroxene from CI chondrites. *Geochimica et Cosmochimica Acta* 61:835–845.
- Leya I. and Masarik J. 2009. Cosmogenic nuclides in stony irons revisited. *Meteoritics & Planetary Science* 44:1061–1086.
- Lodders K. and Fegley B. 1998. *The planetary scientist's companion*. New York: The Oxford University Press. 370 pp.
- Löhn B., and El Goresy A. 1992. Morphologies and chemical composition of individual magnetite grains in CI and CM chondrites: A potential genetic link to their origin? *Meteoritics* 27:252.
- Macke R. J., Consolmagno G. J., and Britt D. T. 2011a. Density, porosity, and magnetic susceptibility of carbonaceous chondrites. *Meteoritics & Planetary Science* 46:1842–1862.
- Macke R. J., Britt D. T., and Consolmagno G. J. 2011b. Density, porosity, and magnetic susceptibility of achondritic meteorites. *Meteoritics & Planetary Science* 46:311–326.
- MacKinnon I. D. R. 1980. Structures and textures of the Murchison and Mighei carbonaceous chondrite matrices. Proceedings of the 11th Lunar and Planetary Science Conference. pp. 839–852.
- MacKinnon I. D. R. 1982. Ordered mixed-layer structures in the Mighei carbonaceous chondrite matrix. *Geochimica et Cosmochimica Acta* 46:479–489.
- Mainzer A., Grav T., Masiero J., Hand E., Bauer J., Tholen D., McMillan R. S., Spahr T., Cutri R. M., Wright E., Watkins J., Mo W., and Maleszewski C. 2011. Neowise studies of spectrophotometrically classified asteroids: Preliminary results. *Astrophysical Journal* 741:90 (25 pp).
- McKay D. S., Swindle T. D., and Greenberg R. 1989. Asteroidal regoliths: What we do not know. In *Asteroids II*, edited by Binzel R. P. Tucson, Arizona: University of Arizona Press. pp. 617–642.
- McSween H. Y. Jr. 1979. Alteration in CM carbonaceous chondrites inferred from modal and chemical variations in matrix. *Geochimica et Cosmochimica Acta* 43:1761–1770.
- Meier M. M., Welten K. C., Caffee M. W., Friedrich J. M., Jenniskens P., Nishiizumi K., Shaddad M. H., and Wieler R. 2012. A noble gas and cosmogenic radionuclide analysis of two ordinary chondrites from Almahata Sitta. *Meteoritics & Planetary Science* 47:1075–1086.
- Michalski J. R., Kraft M. D., Sharp T. G., Williams L. B., and Christensen P. R. 2006. Emission spectroscopy of clay minerals and evidence for poorly crystalline aluminosilicates on Mars from thermal emission spectrometer data. *Journal of Geophysical Research* 111. <https://doi.org/10.1029/2005JE002438>.
- Michel P., Benz W., Tanga P., and Richardson D. C. 2001. Collisions and gravitational reaccumulation: Forming asteroid families and satellites. *Science* 294:1696–1700.
- Michel P., Jutzi M., Richardson D. C., Goodrich C. A., Hartmann W. K., and O'Brien D. P. 2015. Selective sampling during catastrophic disruption: mapping the location of reaccumulated fragments in the original parent body. Proceedings of the 8th Catastrophic Disruption Workshop. *Planetary and Space Science* 107:24–28.
- Mittlefehldt D. W., Lindstrom M. M., Bogard D. D., Garrison D. H., and Field S. W. 1996. Acapulco- and Lodran-like achondrites: Petrology, geochemistry, chronology, and origin. *Geochimica et Cosmochimica Acta* 60:867–882.
- Mittlefehldt D. W., McCoy T. J., Goodrich C. A., and Kracher A. 1998. Non-chondritic meteorites from asteroidal bodies. In *Planetary materials*, edited by Papike J. J. Washington, D.C.: Mineralogical Society of America. pp. 4–1–4–195.
- Mittlefehldt D. W., Bogard D. D., Berkley J. L., and Garrison D. H. 2003. Brachinites: Igneous rocks from a differentiated asteroid. *Meteoritics & Planetary Science* 38:1601–1625.
- Müller W. F., Kurat G., and Kracher A. 1977. Crystal structure and composition of cronstedtite from the Cochabamba carbonaceous chondrite. *Meteoritics* 12:322 (abstract).
- Murty S. V. S., Mahajan R. R., Jenniskens P., Shaddad M. H., and Eldien B. 2010. Noble gases and nitrogen in the Almahata Sitta ureilite. *Meteoritics & Planetary Science* 45:1751–1764.
- Nagahara H. 1992. Yamato-8002: Partial melting residue on the “unique” chondrite parent body. *Proceedings of the NIPR Symposium on Antarctic Meteorites* 5:191–223.
- Nagao K., Haba M. K., Zolensky M., Jenniskens P., and Shaddad M. H. 2014. Noble gases in two fragments of different lithologies from the Almahata Sitta meteorite (abstract #5204). 77th Annual Meeting of the Meteoritical Society.
- Nakamura T. 2005. Post-hydration thermal metamorphism of carbonaceous chondrites. *Journal of Mineralogical and Petrological Sciences* 100:260–272.
- Nehru C. E., Prinz M., and Delaney J. S. 1983. Brachina: A new type of meteorite, not a chassignite. Proceedings, 14th Lunar and Planetary Science Conference, Part 1. *Journal of Geophysical Research* 88:B237–B244.
- Ott U. 2014. Planetary and pre-solar noble gases in meteorites. *Chemie der Erde* 74:519–544.
- Ott U., Löhr H. P., and Begemann F. 1985. Trapped neon in ureilites – A new component. In *Isotopic ratios in the solar system*. Toulouse, France: Cepa Dues-Editions. pp. 129–136.
- Ott U., Löhr H. P., and Begemann F. 1990. EET 83309: A ureilite with solar noble gases. *Meteoritics* 25:396.
- Ott U., Hermann S., Jenniskens P. M., and Shaddad M. 2010. A noble gas study of two stones from the Almahata Sitta meteorite (abstract #1195). 41st Lunar and Planetary Science Conference. CD-ROM.
- Papike J. J., Spilde M. N., Fowler G. W., Layne G. D., and Shearer C. K. 1995. The Lodran primitive achondrite: Petrogenetic insights from electron and ion microprobe analysis of olivine and orthopyroxene. *Geochimica et Cosmochimica Acta* 59:3051–3070.
- Patzek M., Hoppe P., Bischoff A., Visser R., and John T. 2017. Water-bearing, volatile-rich clasts in howardites and

- polymict ureilites – Carriers of deuterium-enriched waters not sampled by individual meteorites (abstract #6183). 80th Annual Meeting of the Meteoritical Society.
- Patzek M., Bischoff A., Visser R., and John T. 2018a. Mineralogy of volatile-rich clasts in brecciated meteorites. *Meteoritics & Planetary Science* 53:2519–2540.
- Patzek M., Pack A., Bischoff A., Visser R., and John T. 2018b. O-isotope composition of CI- and CM-like clasts in ureilites, HEDs, and CR chondrites (abstract #6254). 81st Annual Meeting of the Meteoritical Society. Meteoritical Society.
- Pearson V. K., Sephton M. A., Franchi I. A., Gibson J. M., and Gilmour I. 2006. Carbon and nitrogen in carbonaceous chondrites: Elemental abundances and stable isotopic compositions. *Meteoritics & Planetary Science* 41:1899–1918.
- Peck J. A. 1984. Origin of the variation in properties of CV3 meteorite matrix and matrix clasts. Proceedings, 15th Lunar and Planetary Science Conference. pp. 635–636.
- Petaev M. I., Barsukova L. D., Lipschutz M. E., Wang M.-S., Ariskin A. A., Clayton R. N., and Mayeda T. K. 1994. The Divnoe meteorite: Petrology, chemistry, oxygen isotopes and origin. *Meteoritics* 29:182–199.
- Popova O., Borovička J., Hartmann W. K., Spurný P., Gnos E., Nemtchinov I., and Trigo-Rodríguez J. M. 2011. Very low strengths of interplanetary meteoroids and small asteroids. *Meteoritics & Planetary Science* 46:1525–1550.
- Prinz M., Weisberg M. K., Nehru C. E., and Delaney J. S. 1986. North Haig and Nilpena: Paired polymict ureilites with Angra dos Reis-related and other clasts (abstract). 18th Lunar and Planetary Science. pp. 681–682.
- Prinz M., Weisberg M. K., Nehru C. E., and Delaney J. S. 1987. Black inclusions of carbonaceous chondrite matrix material in polymict ureilites. *Meteoritics* 22:482–483.
- Prinz M., Weisberg M. K., and Nehru C. E. 1988. Feldspathic components in polymict ureilites (abstract). 19th Lunar and Planetary Science, pp. 947–948.
- Rai V. K., Murty V. S., and Ott U. 2003. Noble gases in ureilites: Cosmogenic, radiogenic, and trapped components. *Geochimica et Cosmochimica Acta* 67:4435–4456.
- Reddy V., Le Corre L., O'Brien D. P., Nathues A., Cloutis E. A., Durda D. D., Bottke W. F., Bhatt M. U., Nesvorný D., Buczkowski D., Scully J. E. C., Palmer E. M., Sierk H., Mann P. J., Becker K. J., Beck A. W., Mittlefehldt D., Li J.-Y., Gaskell R., Russell C. T., Gaffey M. J., McSween H. Y., McCord T. B., and Blewett D. 2012. Delivery of dark material to Vesta via carbonaceous chondritic impacts. *Icarus* 221:544–559.
- Reddy V., Shephard M. K., Takir D., Sanchez J. A., Richardson J., Emery J. P., and Taylor P. A. 2017. Psyche: state of knowledge from ground-based observations (abstract #6335). 80th Annual Meeting of the Meteoritical Society.
- Reisener R. J. and Goldstein J. I. 2003. Ordinary chondrite metallography: Part 2. Formation of zoned and unzoned metal particles in relatively unshocked H, L, and LL chondrites. *Meteoritics & Planetary Science* 38:1679–1696.
- Riebe M. E. I., Welten K. C., Meier M. M. M., Wieler R., Barth M. U. F., Ward D., Laubenstein M., Bischoff A., Caffee M. W., Nishiizumi K., and Busemann H. 2017a. Cosmic-ray exposure ages of six chondritic Almahata Sitta fragments. *Meteoritics & Planetary Science* 52:2353–2374.
- Riebe M. E. I., Busemann H., Wieler R., and Maden C. 2017b. Closed system step etching of CI chondrite Ivuna reveals primordial noble gases in the HF-solubles. *Geochimica et Cosmochimica Acta* 205:65–83.
- Rivkin A. S. 2012. The fraction of hydrated C-complex asteroids in the asteroid belt from SDSS data. *Icarus* 221:327–333.
- Rivkin A. S., Campins H., Emery J. P., Howell E. S., Licandro J., Takir D., and Vilas F. 2015. Astronomical observations of volatiles on asteroids. In *Asteroids IV*, edited by Michel P., DeMeo R. E., and Bottke W. F. Tucson, Arizona: The University of Arizona Press. pp. 65–88.
- Rodriguez-Navarro C., Ruiz-Agudo E., Luque A., Rodriguez-Navarro A., and Ortega-Huertas M. 2009. Thermal decomposition of calcite: Mechanisms of formation and textural evolution of CaO nanocrystals. *American Mineralogist* 94:578–593.
- Ross A. J., Downes H., Smith C. L., and Jones A. P. 2010. DaG 1047: A polymict ureilite containing exotic clasts including a chondrite (abstract #2361). 41st Lunar and Planetary Science Conference. CD-ROM.
- Ross A. J., Steele A., Fries M. D., Kather L., Downes H., Jones A. P., Smith C. L., Jenniskens P. M., Zolensky M. E., and Shaddad M. H. 2011. MicroRaman spectroscopy of diamond and graphite in Almahata Sitta and comparison with other ureilites. *Meteoritics & Planetary Science* 46:364–378.
- Rout S. S., Heck P. R., Isheim D., Stephan T., Zaluzec N. J., Miller D. J., Davis A. M., and Seidman D. N. 2017. Atom-probe tomography and transmission electron microscopy of the kamacite-taenite interface in the fast-cooled Bristol IVA iron meteorite. *Meteoritics & Planetary Science* 52:2707–2729.
- Rubin A. E. 1990. Kamacite and olivine in ordinary chondrites: Intergroup and intragroup relationships. *Geochimica et Cosmochimica Acta* 54:1217–1232.
- Sanborn M. E., Yin Q.-Z., Goodrich C. A., Zolensky M., and Fioretti A. M. 2017. A case for nebula scale mixing between non-carbonaceous and carbonaceous chondrite reservoirs: Testing the Grand Tack model with chromium isotopic composition of Almahata Sitta stone 91A (abstract #6277). 80th Annual Meeting of the Meteoritical Society.
- Scheirich P., Durech J., Pravec P., Kozubal M., Dantowitz R., Kaasalainen M., Betzler A. S., Meltrame P., Muler G., Birtwhistle P., and Kugel F. 2010. The shape and rotation of asteroid 2008 TC₃. *Meteoritics & Planetary Science* 45:1804–1811.
- Scott E. R. D. and Krot A. N. 2004. Chondrites and their components. In *Meteorites, comets, and planets*, edited by Davis A. M. Treatise on Geochemistry, vol. 1 edited by Holland H. D. and Turekian K. K. Oxford: Elsevier-Perigamon. pp. 143–200.
- Scott E. R. D., Krot A. N., and Sanders I. S. 2018. Isotopic dichotomy among meteorites and its bearing on the protoplanetary disk. *The Astrophysical Journal* 854:164 (12 pp).
- Shaddad M. H., Jenniskens P., Numan D., Kudoda A. M., Elsir S., Riyah I. F., Ali A. E., Alameen M., Alameen N. M., Eid O., Osman A. T., AbuBaker M. I., Yousif M., Chesley S. R., Chodas P. W., Albers J., Edwards W. N., Brown P. G., Kuiper J., and Friedrich J. M. 2010. The recovery of asteroid 2008 TC₃. *Meteoritics & Planetary Science* 45:1618–1637.
- Singletary S. J. and Grove T. L. 2003. Early petrologic processes on the ureilite parent body. *Meteoritics & Planetary Science* 38:95–108.

- Smith P. P. K. and Buseck P. R. 1981. Graphitic carbon in the Allende meteorite, a microstructural study. *Science* 212:323–342.
- Steele I. M. 1990. Minor elements in forsterites of Orgueil (C1), Alais (C1) and two interplanetary dust particles compared to C2-C3-UOC forsterites. *Meteoritics & Planetary Science* 25:301–307.
- Takeda H. 1987. Mineralogy of Antarctic ureilites and a working hypothesis for their origin and evolution. *Earth and Planetary Science Letters* 81:358–370.
- Takeda H. 1989. Mineralogy of coexisting pyroxenes in magnesian ureilites and their formation conditions. *Earth and Planetary Science Letters* 93:181–194.
- Takeda H., Mori H., and Ogata H. 1989. Mineralogy of augite-bearing ureilites and the origin of their chemical trends. *Meteoritics* 24:73–81.
- Takeda H., Mori H., Hiroi T., and Saito J. 1994. Mineralogy of new Antarctic achondrites with affinity to Lodran and a model of their evolution in an asteroid. *Meteoritics* 29:830–842.
- Takir D., Reddy V., Sanchez J. A., Shepard M. K., and Emery J. P. 2017. Detection of water and/or hydroxyl on asteroid (16) Psyche. *The Astronomical Journal* 153:31 (6 pp).
- Tenner T. J., Nakashima D., Ushikubo T., Kita N. T., and Weisberg M. K. 2015. Oxygen isotope ratios of FeO-poor chondrules in CR3 chondrites: influence of dust enrichment and H₂O during chondrule formation. *Geochimica et Cosmochimica Acta* 148:228–250.
- Tholen D. J. 1984. *Asteroid taxonomy from cluster analysis of photometry*. University of Arizona. PhD Thesis.
- Tholen D. J. and Barucci M. 1989. Asteroid taxonomy. In *Asteroids II*, edited by Binzel R., Gehrels T., and Matthews M. Tucson, Arizona: University of Arizona Press. pp. 298–315.
- Tomeoka K. and Buseck P. R. 1988. Matrix mineralogy of the Orgueil CI carbonaceous chondrite. *Geochimica et Cosmochimica Acta* 52:1627–1640.
- Tonui E., Zolensky M., Hiroi T., Nakamura T., Lipschutz M., Wang M.-S., and Okudaira K. 2014. Petrographic, chemical and spectroscopic evidence for thermal metamorphism in carbonaceous chondrites I: CI and CM chondrites. *Geochimica et Cosmochimica Acta* 126:284–306.
- Treiman A. H. and Berkley J. L. 1994. Igneous petrology of the new ureilites Nova 001 and Nullarbor 010. *Meteoritics* 29:843–848.
- Turrini D., Combe J.-P., McCord T. B., Oklay N., Vincent J.-B., Prettyman T. H., McSween H. Y., Consolmagno G. J., De Sanctis M. C., Le Corre L., Longobardo A., Palomba E., and Russell C. T. 2014. The contamination of the surface of Vesta by impacts and the delivery of the dark material. *Icarus* 240:86–102.
- Ushikubo T., Kimura M., Kita N. T., and Valley J. W. 2012. Primordial oxygen isotope reservoirs of the solar nebula recorded in chondrules in Acfer 094 carbonaceous chondrite. *Geochimica et Cosmochimica Acta* 90:242–264.
- Visser R., John T., Patzek M., Bischoff A., and Whitehouse M. 2018. Sulfur isotope compositions of sulfides in carbonaceous chondrites and volatile-rich, CI- and CM-like clasts from various chondrites and achondrites (abstract #6190). 81st Annual Meeting of the Meteoritical Society.
- Warren P. H. and Kallemeyn G. W. 1989. The second brachinite, far more differentiated than Brachina, and an ultramafic achondritic clast from L chondrite Yamato 75097. Proceedings of the 19th Lunar and Planetary Science Conference. pp. 475–486.
- Warren P. H. and Kallemeyn G. W. 1992. Explosive volcanism and the graphite-oxygen fugacity buffer on the parent asteroid(s) of the ureilite meteorites. *Icarus* 100:110–126.
- Warren P. H. and Rubin A. E. 2011. Pyroxene-selective impact smelting in ureilites. *Geochimica et Cosmochimica Acta* 74:5109–5133.
- Weber I., Bischoff A., and Weber D. 2003. TEM investigations on the monomict ureilites Jalanash and Hammadah al Hamra 064. *Meteoritics & Planetary Science* 38:145–156.
- Weisberg M. K. and Kimura M. 2012. The unequilibrated enstatite chondrites. *Chemie der Erde* 72:101–115.
- Welten K. C., Meier M. M. M., Caffee M. W., Nishiizumi K., Wieler R., Jenniskens P., and Shaddad M. H. 2010. Cosmogenic nuclides in Almahata Sitta ureilites: Cosmic-ray exposure age, preatmospheric mass, and bulk density of asteroid 2008 TC₃. *Meteoritics & Planetary Science* 45:1728–1742.
- Wieler R. 2002. Cosmic-ray-produced noble gases in meteorites. *Reviews in Mineralogy and Geochemistry* 47:125–170.
- Wieler R., Baur H., and Signer P. 1986. Noble gases from solar energetic particles revealed by closed system stepwise etching of lunar soil minerals. *Geochimica et Cosmochimica Acta* 50:1997–2017.
- Wieler R., Busemann H., and Franchi I. A. 2006. Trapping and modification processes of noble gases and nitrogen in meteorites and their parent bodies. In *Meteorites and the early solar system II*, edited by Lauretta D. S. and McSween H. Y. Jr. Tucson, Arizona: The University of Arizona Press. pp. 499–521.
- Wlotzka F. 1972. Haverö ureilite: Evidence for recrystallization and partial reduction. *Meteoritics* 7:591–600.
- Yeomans D. 2008. NASA/JPL Near-earth Object Program Office statement. <http://neo.jpl.nasa.gov/news/news159.html>.
- Yin Q.-Z., Sanborn M. E., Goodrich C. A., Zolensky M., Fioretti A. M., Shaddad M., Kohl I. E., and Young E. D. 2018. Nebula scale mixing between non-carbonaceous and carbonaceous chondrite reservoirs: Testing the Grand Tack model with Almahata Sitta stones (abstract #1810). 49th Lunar and Planetary Science Conference. CD-ROM.
- Zanda B., Bourot-Denise M., Perron C., and Hewins R. H. 1994. Origin and metamorphic redistribution of silicon, chromium, and phosphorus in the metal of chondrites. *Science* 265:1846–1849.
- Zolensky M. and McSween H. Y. Jr. 1988. Aqueous alteration. In *Meteorites and the early solar system*, edited by Kerridge J. F. and Matthews M. S. Tucson, Arizona: The University of Arizona Press. pp. 114–143.
- Zolensky M. E., Barrett T., and Browning L. 1993. Mineralogy and composition of matrix and chondrule rims in carbonaceous chondrites. *Geochimica et Cosmochimica Acta* 57:3123–3148.
- Zolensky M. E., Weisberg M. K., Buchanan P. C., and Mittlefehldt D. W. 1996. Mineralogy of carbonaceous chondrite clasts in HED achondrites and the Moon. *Meteoritics & Planetary Science* 31:518–537.
- Zolensky M., Herrin J., Mikouchi T., Ohsumi K., Friedrich J., Steele A., Rumble D., Fries M., Sandford S., Milam S., Hagiya K., Takeda H., Satake W., Kurihara T., Colbert

- M., Hanna R., Maisano J., Ketcham R., Goodrich C. A., Le L., Robinson G.-A., Martinez J., Ross K., Jenniskens P., and Shaddad M. 2010. Mineralogy and petrography of the Almahata Sitta ureilite. *Meteoritics & Planetary Science* 45:1618–1637.
- Zolensky M., Fries M., Chan Q. H.-S., Yebukawa Y., Steel A., Bodnar R. J., Ito M., Nakashima D., Nakamura T., Greenwood R., Rahman Z., Le L., Ross D. J., Ziegler K., Bottke W., and Martinez J. 2018. Outer solar system material in inner solar system regolith breccias (abstract #6103). 81st Annual Meeting of the Meteoritical Society.
- Zolotov M. Y., Mironenko M. V., and Shock E. L. 2006. Thermodynamic constraints on fayalite formation on parent bodies of chondrites. *Meteoritics & Planetary Science* 41:1775–1796.

SUPPORTING INFORMATION

Additional supporting information may be found in the online version of this article.

Fig. S1. Location of SIMS analyses.

Table S1. Instrumental bias and mineral standards and formula for bias correction in SIMS analyses.

Table S2. Mean values and reproducibility of

running standard analyses in SIMS analyses.

Table S3. SIMS isotope analyses of silicates and carbonates in AhS 91-01.

Supplement 1. Fragments of Almahata Sitta samples 91/91A and 671 studied in this work.

Supplement 2. Analytical methods.

Supplement 3. Raman spectroscopy.
